Title

Numerical Studies of Electron-Phonon Interactions and Non-equilibrium Phenomena in Strongly Correlated Systems

Author

Zhang, Yuxi

Publication Date

2022

Peer reviewed|Thesis/dissertation

Numerical Studies of Electron-Phonon Interactions and Non-equilibrium Phenomena in Strongly Correlated Systems

By

Yuxi Zhang

DISSERTATION

Submitted in partial satisfaction of the requirements for the degree of

DOCTOR OF PHILOSOPHY

in

PHYSICS

in the

OFFICE OF GRADUATE STUDIES

of the

UNIVERSITY OF CALIFORNIA

DAVIS

Approved:

Richard T. Scalettar, Chair

Warren Pickett

Gergely Zimanyi

Committee in Charge

2022

To

my family

and everyone who have ever helped and supported me

Contents

List of Figures

Abstract

Strongly correlated systems account for many fascinating physics phenomena, from superconductivity (SC) to charge density wave (CDW) order. Finding a complete explanation for these phenomena, however, is very challenging: solving the problem on a mean-field level is useful but approximate, and treating interactions non-perturbatively is extremely hard because of the many-body nature of these systems. Therefore, numerical algorithms such as quantum Monte Carlo (QMC) and exact diagonalization (ED) that are able to solve strongly correlated systems exactly start to play a hugely important role. In this thesis, we first introduce in chapters 2 and 3 the model Hamiltonians and numerical methods employed to explore pairing and charge orders, then we present several numerical studies with a variety of focuses. Chapters 4 and 5 look at the effect of electron-phonon interactions on Dirac Fermions and charge order and related phase transitions. In chapter 6 we study the possibility of orbital-selective behavior of charge order, when there is inter-orbital hybridization and two distinct electron-phonon couplings. Chapter 7 displays an out-of-equilibrium study of pairing, charge and magnetic orders upon photoirradiation, where an enhancement of d-wave superconductivity is observed. Finally in the last chapter, we provide a summary and outlook of our work.

Acknowledgments

I always count myself as a very fortunate person: every step in my life I've met many very nice people who have helped me tremendously. This is especially true here in UC Davis where I'm pursuing my PhD.

Everyone says pursuing PhD in physics is very hard, not least doing so in a foreign country 9,000 km from home. But "hard" is not the primary word I'd use to describe my grad school, I'd describe it as challenging but enjoyable, and this is predominantly thanks to my advisor, Professor Richard Scalettar. Professor Scalettar really thinks of his students and helps students as much as he can, he provides a comfortable and respectful working environment for everyone, from a student point of view this eliminates so much of the anxiety surrounding grad school, and I cannot stress enough how much I appreciate this. He is an incredible teacher who is able to convey complicated materials in simple terms, and he has the perfect balance of providing enough guidance whenever I need them, while always letting me go find the answers by myself. What really impresses me is not only his remarkable knowledge in this field but also his passion for physics and his work ethic, and I've learnt so much from Professor Scalettar, from how to conduct a research to how to be a respectful and professional physicist.

I'm fortunate that I have the privilege to work with my collaborators: Professor George Batrouni, Professor Rubem Mondaini, Professor Huaiming Guo and Professor Natanael C Costa. They are all excellent physicists from whom I have learnt a lot research-wise, but also they are all extremely nice people who would not hesitate whenever I ask any questions, physics related or not. I'm especially grateful to Professor Inna Vishik here at UC Davis, who kindly allows me to join her group meetings for the past two years so that I have the opportunity to learn about condensed matter experiments first-hand.

I also want to say a big, big thank you to many of my fellow PhD students. I'm really grateful to have shared the group (and the office!) with Ben Cohen-Stead, with whom I have spent countless time debating and discussing with, and these discussions have hugely helped me in research and pushed me forward. As well as all the time climbing together at Rocknasium, all the time at hotpot or sushi restaurants, all the time I've asked you to correct my English —thank you for making my life so much easier in so many areas. Also a special thanks to Ronaldo Ortez, thank you for all

those late and long conversations, and thank you for sharing your thoughts and stories with me. Of course also other group mates, class mates and room mates: Chunhan Feng, Bo Xiao, Wei-Ting Chiu, Owen Bradley, Yao Yao, Xiaoxiao Yang, Xiaohong Yang and everyone else, thank you for always being there and thank you for making my life so much more enjoyable.

My parents. I always consider myself fortunate that I'm able to figure out what I want to do from a relatively early age, but I'm even more fortunate because you have always supported me and trusted me and letting me make my own decisions, even if my decisions don't necessarily align with what you would have wanted. Thank you for being open-minded and supportive, especially through the tough times. Thank you.

Pursing a career in academia, especially in physics, might be really hard, but I'm incredibly happy and grateful for all the people I've met along this journey. Without you I will not be able to be where I am today and be the person I am today. You made everything worth it.

CHAPTER 1

Introduction

1.1. The physics of strongly correlated materials

In his famous paper "More is different" published in 1972, Phil Anderson stated "The behavior of large and complex aggregates of elementary particles, it turns out, is not to be understood in terms of a simple extrapolation of the properties of a few particles." [4]. The philosophy that collective behavior of a large quantity of particles is fundamentally different from that of a few particles opens a new door in research in physics, and is a key insight in understanding the condensed matter physics known today.

What makes collective behavior really interesting are the *interactions* between particles. Theoretical calculations on non-interacting systems has been well-established over the years, and for many systems, treating the Coulomb interactions such as the electron-electron interactions as a perturbation works well. This is, however, not applicable to all systems. Physical phenomena occurring in "strongly correlated systems", including superconductivity, topological phases, quantum spin liquids and strange metals, require interactions to be treated non-perturbatively, which greatly complicates the problem, and satisfactory understanding of these phenomena is still not reached after decades of intense work.

A perfect example to showcase this is high T_c superconductivity (SC). The phenomenon of superconductivity, where the resistance of a material drops to zero upon cooling below a certain temperature, was discovered in 1911. Since then, people have been trying to formulate a microscopic theory to explain this phenomenon; the most successful of them being the Bardeen–Cooper–Schrieffer (BCS) theory [5, 6], which proposes that superconductivity is a result of condensation of "Cooper pairs", which occurs due to an effective interaction mediated by phonons. BCS theory works well for the superconductors known at the time, but is challenged by the so-called "high T_c superconductivity" found in cuprates [7].

The first high T_c superconductor found, in 1986, was lanthanum barium copper oxide, or LBCO; many others are identified later, such as $La_{2-x}Sr_xCuO_4$ (LSCO), yttrium barium copper oxide (YBCO) or bismuth strontium calcium copper oxide (BSCCO). Over the last 35 years, their properties have been measured and analyzed. Their detailed characterization has been made possible because of the development of experimental techniques, such as angle-resolved photoemission spectroscopy (ARPES) which can directly measure electronic band structure, scanning tunneling microscope (STM) which can image surfaces at the atomic level, nuclear magnetic resonance (NMR), and phonon scattering etc.

Theoretical works and numerical techniques have also been developed aiming at providing a complete explanation of the experimental data observed in cuprate materials. It should be emphasized that for correlated many-body systems exactly solving analytically is mostly impossible, so analytical work or theories mostly involve some forms of approximation; computational techniques therefore can become the "go to" tools in the theoretical world. Among these tools are quantum Monte Carlo (QMC) methods, which have been playing an essential role in the computational physics world, and will be introduced in detail in chapter 2. Other methods include the density-matrix renormalization group (DMRG) method, dynamical mean-field theory (DMFT), dynamical cluster approximation (DCA), exact diagonalization (ED) methods, and more recently, machine learning (ML) techniques. There was an early skepticism of computational results in the community, but the amount of information a modern (super)computer can store, or the amount of calculation it can handle, is way beyond what a human-being can possibly perform. Therefore computational studies should not be considered as an replacement of human's brainpower; rather it should be seen as an extension that can perform calculations that human cannot.

Other than superconductivity, other interesting physical phenomena are also observed and studied; one of them being charge density wave (CDW) order. A charge density wave describes pattern (checkerboard or stripe) in the positions of electrons in real space in a crystal. The conventional explanation of CDW formation is the "Peierls instability", which says a one-dimensional equally spaced chain with one electron per ion is unstable; for two-dimensional systems, it generalizes to "Fermi Surface Nesting", which describes when Fermi surface contours

coincide when shifted along the observed CDW wave vector. But unconventional CDW order has since been observed as well, mostly in transition metal dichalcogenides materials, which cannot be explained by Fermi Surface Nesting, and complete understanding of its mechanism is still lacking. As studies furthered, people also discovered that CDW order is sometimes related to superconductivity, such that it helps or suppresses the formation of superconductivity.

In addition to the fascinating physics phenomena like superconductivity or charge density wave order, phase transitions to these orders are interesting by themselves. Phase transitions are relatable to everyone's daily life, yet many aspects are still not fully explained, especially for interaction-driven phase transitions (as opposed to temperature driven phase transitions), quantum phase transitions, and behavior near the critical point.

All in all, there are many fascinating yet unanswered questions still awaiting for us. In this thesis, we will present work that aims to continue and further our understanding on many of the topics mentioned above. More specifically, we will present several QMC studies of charge density wave order and the phase transitions related to them; as well as a study of pairing in an out-of-equilibrium quantum system.

The fundamental equations that governs quantum systems is of course the Schrödinger equation

$$i\hbar\frac{d}{dt}|\Phi(t)\rangle = \hat{H}|\Phi(t)\rangle\,. \tag{1.1}$$

As far as a condensed matter physicist is concerned, the Hamiltonian for a many-body system in a d-dimensional space can be generally written as

$$\begin{aligned} H = &\int d^dR\,\Psi^\dagger(\vec{R})\left[-\frac{\hbar^2}{2M_{\text{ion}}}\nabla^2\right]\Psi(\vec{R}) + \\ &\frac{1}{2}\int d^dR d^dR'\,\Psi^\dagger(\vec{R'})\Psi^\dagger_\sigma(\vec{R})\,U_{\text{ion}-\text{ion}}(\vec{R}-\vec{R'})\,\Psi_{\sigma'}(\vec{R'})\Psi_\sigma(\vec{R}) + \\ &\sum_\sigma\sum_n\int d^dr_n\,\psi^\dagger_\sigma(\vec{r}_n)\left[-\frac{\hbar^2}{2m_e}\nabla^2 + U_{\text{ion}-\text{el}}(\vec{r}_n)\right]\psi_\sigma(\vec{r}_n) + \\ &\frac{1}{2}\sum_{\sigma,\sigma'}\sum_{n,n'}\int d^dr_n d^dr'_{n'}\,\psi^\dagger_{\sigma'}(\vec{r'}_{n'})\psi^\dagger_\sigma(\vec{r}_n)\,U_{\text{el}-\text{el}}(\vec{r}_n-\vec{r'}_{n'})\,\psi_{\sigma'}(\vec{r'}_{n'})\psi_\sigma(\vec{r}_n)\,. \end{aligned} \tag{1.2}$$

The first two lines describes nuclei and the last two lines describes electrons in the system. $\Psi_\sigma(\vec{R})$ is nuclei field operator at location $\vec{R}$; the first line corresponds to the kinetic energy of nuclei, and

the second line is the Coulomb interactions among the nuclei

$$U_{\text{ion}-\text{ion}}(\vec{R}-\vec{R}') = \frac{Z_A Z_B e^2}{|\vec{R}-\vec{R}'|}\,. \tag{1.3}$$

Likewise $\psi_\sigma(\vec{r}_n)$ is electron field operator at location $\vec{r}$ where $\sigma = \uparrow, \downarrow$ is the spin index and $n, n' = 1, 2, \cdots N$ are electrons at location $\vec{r}$. The first term in line three $-\frac{\hbar^2}{2m_e}\nabla^2$ describes the kinetic energy of electrons, whereas the second term $U_{\text{ion}-\text{el}}(\vec{r})$ presents the Coulomb interactions between nuclei and an electron at location $\vec{r}$

$$U_{\text{ion}-\text{el}}(\vec{r}) = \int d^d R \frac{Ze^2}{|\vec{r}-\vec{R}|}\,. \tag{1.4}$$

Finally the last line describes the electron-electron Coulomb interactions

$$U_{\text{el}-\text{el}}(\vec{r}-\vec{r'}) = \frac{e^2}{|\vec{r}-\vec{r'}|}\,. \tag{1.5}$$

Before we move on, it's worth pointing out the complexity of this Hamiltonian. Although the fact that it contains only kinetic energy and Coulomb interactions may make it look simple, it instantly becomes unsolvable when the system scale gets to the order of 10^{23}, with the number of states grow exponentially with the number of particles. This scale is way beyond what a modern super computer can handle. Thus the problem going from macroscopic to microscopic is not only technical; it becomes one of *principle* [8].

Fortunately, the mass for nuclei is much larger than that of electrons $M_{\text{ion}} \gg m_e$ and therefore the motion of nuclei is much slower than that of electrons (or, the kinetic energy of nuclei is much smaller than that of the electrons $\mathcal{K}_{\text{ion}} \ll \mathcal{K}_{\text{el}}$). Because of this, we can separate the nuclei and the electrons part of the Hamiltonian, the so-called **Born–Oppenheimer (BO) approximation**, and only focus on the electron parts (which account for most of the interesting physics). But even so, the system is still incredibly complex with local and long-range electron-electron interactions, local and long-range electron-ion interactions, spin interactions, inhomogeneity of real systems and defects, and many other effects; people therefore proposed many simplified models that account for only one or few of these "effects" and focused on solving them, hoping that it will capture the most essential physics happening in the real world. This approach has gained great success, and there's no better example to illustrate this than *the Hubbard model* [9].

1.2. The Hubbard model

The Hubbard model [9] is one of the simplest model in describing the electron-electron interactions in a many-body system. Using **second quantization**, that is, using the creation and annihilation operators to express the Hamiltonian, the one-band Hubbard model can be written as

$$\hat{\mathcal{H}} = -t \sum_{\langle \mathbf{i},\mathbf{j}\rangle,\sigma} \left(\hat{c}^{\dagger}_{\mathbf{i}\sigma}\hat{c}_{\mathbf{j}\sigma} + \text{H.c.}\right) + U\sum_{\mathbf{i}} \hat{n}_{\mathbf{i}\uparrow}\hat{n}_{\mathbf{i}\downarrow} - \mu\sum_{\mathbf{i}}(\hat{n}_{\mathbf{i}\uparrow} + \hat{n}_{\mathbf{i}\downarrow}) \,, \tag{1.6}$$

where the sums on $\mathbf{i}$ and σ run over all lattice sites and spins $\sigma =\uparrow,\downarrow$. $\langle \mathbf{i},\mathbf{j}\rangle$ denotes nearest neighbors. $\hat{c}^{\dagger}_{\mathbf{i}\sigma}$ and $\hat{c}_{\mathbf{i}\sigma}$ are creation and annihilation operators of electrons with spin σ on a given site $\mathbf{i}$; $\hat{n}_{\mathbf{i},\sigma} = \hat{c}^{\dagger}_{\mathbf{i}\sigma}\hat{c}_{\mathbf{i}\sigma}$ is the number operator. The Fermionic creation and annihilation operators obey

$$\{\hat{c}_{\mathbf{i}\sigma},\, \hat{c}^{\dagger}_{\mathbf{j}\sigma'}\} = \delta_{\mathbf{i},\mathbf{j}}\delta_{\sigma,\sigma'} \,, \qquad \{\hat{c}^{\dagger}_{\mathbf{i}\sigma},\, \hat{c}^{\dagger}_{\mathbf{j}\sigma'}\} = 0 \,, \qquad \{\hat{c}_{\mathbf{i}\sigma},\, \hat{c}_{\mathbf{j}\sigma'}\} = 0 \tag{1.7}$$

where $\{\hat{A},\hat{B}\} = \hat{A}\hat{B} \ + \hat{B}\hat{A}$ is the anticommutator relations.

The first term of Eq. (1.6) corresponds to the hopping of electrons between nearest-neighboring sites $\langle \mathbf{i},\mathbf{j}\rangle$, where the hopping amplitude is represented by the parameter t. This term describes the kinetic energy of the electrons in the system $\mathcal{K}_{\text{el}}$. On a lattice with translational symmetry, after Fourier transforming into the k-space

$$\begin{aligned} \hat{c}^{\dagger}_{\mathbf{k}\sigma} &= \frac{1}{\sqrt{N}}\sum_{\mathbf{j}} e^{i\mathbf{k}\cdot\mathbf{j}}\, \hat{c}^{\dagger}_{\mathbf{j}\sigma} \\ \hat{c}_{\mathbf{k}\sigma} &= \frac{1}{\sqrt{N}}\sum_{\mathbf{j}} e^{-i\mathbf{k}\cdot\mathbf{j}}\, \hat{c}_{\mathbf{j}\sigma} \end{aligned} \tag{1.8}$$

where N is the size of the system, we can obtain the electronic structure of the geometry. For a system with more than one atom per unit cell, a "band" index l is needed to indicate multiple bands. Fig. 1.1 demonstrates the band structure for the square lattice (left) and the honeycomb lattice (right).

The second term of Eq. (1.6) is the on-site electron-electron interaction term. Because of Pauli principle, every site can have maximum two electrons with opposite spins. Only when the site is

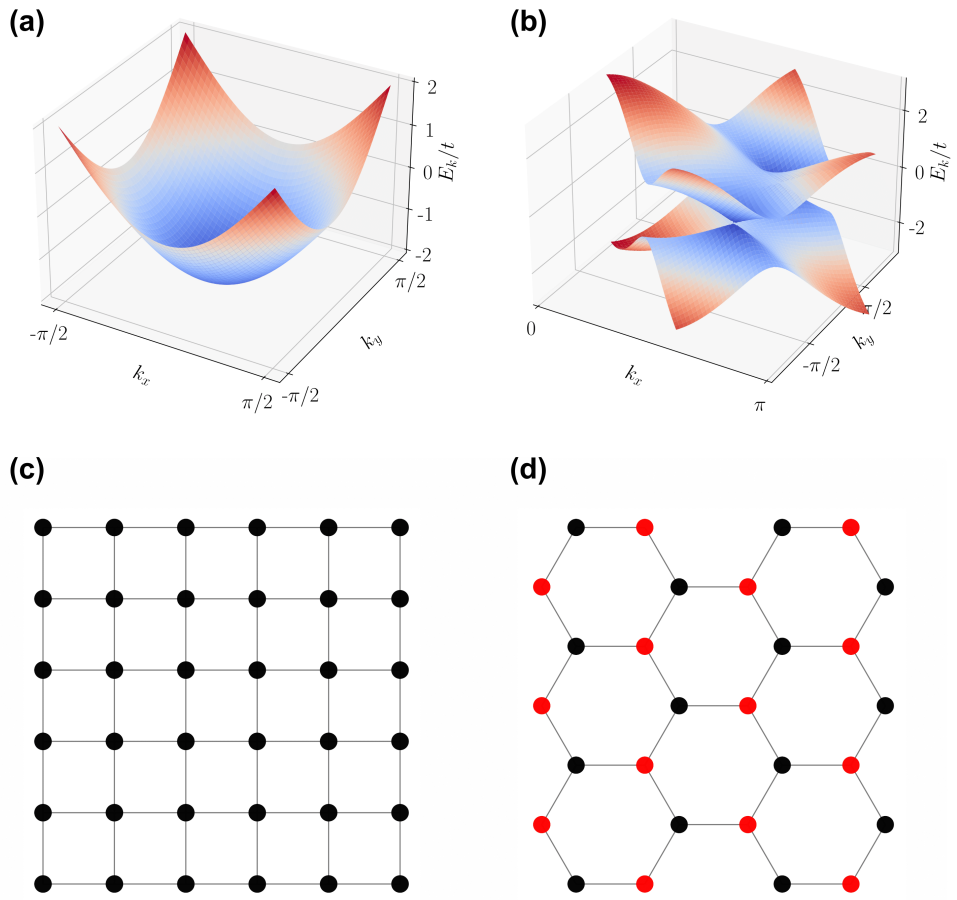

FIGURE 1.1. Square lattice, honeycomb lattice and their corresponding band structure.

doubly occupied will the term return a non-zero value. The energy scale of this el-el interaction is set by U (or rather U/t); roughly speaking the $U/t \lesssim 2$ regime is considered weak coupling, the $2 \lesssim U/t \lesssim 6$ regime is considered intermediate coupling, and $U/t \gtrsim 6$ is considered strong coupling [10]. The reason is that $U/t = 6 \sim 8$ is a rough measure of the bandwidth of many (2D) lattice models. It worth mentioning that the $U/t < 0$ case is also of interest; this model is often referred to as the negative-U Hubbard model or the attractive Hubbard model.

The third term of Eq. (1.6) is the chemical potential term. One can tune μ to change the filling of the system in the grand canonical ensemble. One particular case of interest is half-filling $\langle \hat{n}_{\mathbf{i},\sigma} \rangle = \frac{1}{2}$, which can be achieved by setting $\mu = \frac{U}{2}$ on a bipartite lattice. For this reason, it is

convenient to write the Hubbard model in "Particle-Hole Symmetry" (PHS) form

$$\hat{\mathcal{H}} = -t \sum_{\langle \mathbf{i},\mathbf{j}\rangle,\sigma} \left(\hat{c}^{\dagger}_{\mathbf{i}\sigma}\hat{c}_{\mathbf{j}\sigma} + \text{H.c.}\right) + U\sum_{\mathbf{i}}(\hat{n}_{\mathbf{i}\uparrow} - \frac{1}{2})(\hat{n}_{\mathbf{i}\downarrow} - \frac{1}{2}) - \mu\sum_{\mathbf{i}}(\hat{n}_{\mathbf{i}\uparrow} + \hat{n}_{\mathbf{i}\downarrow}) \tag{1.9}$$

so that $\mu = 0$ corresponds to half-filling.

We mentioned "Particle-Hole Symmetry" (PHS) in the above paragraph. Consider a Particle-hole transformation

$$\hat{d}^{\dagger}_{\mathbf{i}\sigma} = (-1)^{\mathbf{i}}\hat{c}_{\mathbf{i}\sigma}\,, \tag{1.10}$$

if the kinetic energy remains unchanged, then it is said that the system has Particle-hole symmetry (because the potential energy when written as Eq. (1.9) automatically remains unchanged).

The Hubbard model is a very simplified model: only nearest-neighbor hopping is considered, with no variations in hopping amplitude; the electron-electron interaction is strictly local (on-site); only one band is considered with two electrons per site. Because of this, there are many variations of Hubbard models. One can change a subset of bonds to study the effect of geometry inhomogenity, or study multi-bands or multi-orbitals systems to simulate real materials more closely; the extended Hubbard model includes nearest-neighbor interactions $V\sum_{\mathbf{i},\mathbf{j}}\hat{n}_{\mathbf{i}}\hat{n}_{\mathbf{j}}$; the SU(N) Hubbard model provides insights on SU(N) symmetries, etc.

It's important to address the units of parameters in the Hubbard model, so that it's better connected with real materials. With reduced Planck constant and electron mass both normalized $\hbar = 1$ and $m_e = 1$, t, U and μ all have units of energy. Hopping t is usually set to one $t = 1$ to set the energy scale of the system; so when not stated explicitly, values of U and μ are in unit of t. Bandwidth W also has unit of t, for example square lattice and honeycomb lattice have bandwidth of $W = 8t$ and $W = 6t$ respectively. Another physical quantity, the Fermi velocity, also has unit of energy; temperature T is in unit of t as well, and inverse temperature β has unit of $1/t$. In most cuprates (the material Hubbard model is mostly matched to), bandwidth is $W \sim 2$ eV, which gives hopping $t \sim 0.2 - 0.4$ eV.

1.2.1. Why the Hubbard model? For how remarkably simple it is, the Hubbard model provides remarkably rich physics, although much of this still in debate today, after decades of

effort. A Google Scholar search returned more than 250 results with "Hubbard model" in the title, published in 2021 alone.

The two dimensional Hubbard model on a square lattice at half-filling doesn't suffer from the infamous "sign problem" [11] (which will be introduced in section 2.5) thanks to particle-hole symmetry, so it can be sufficiently studied by quantum Monte Carlo methods [12, 13, 14, 15]. In the ground state, the system has insulating antiferromagnetic (AF) order; the gap observed in spectral function is of the Mott type in the strong coupling regime [16], but in the weak coupling regime it's of a different origin (a "slater" gap) [17], indicating a crossover between the two regimes. At finite temperature, an AF pseudogap is observed upon cooling [18]. Away from half-filling, QMC approaches become much trickier with the sign problem, but nonetheless evidence for d-wave superconductivity has been found [19, 20] using other methods. With the presence of next-nearest hopping t', other instabilities like spin-density wave and ferromagnetism have also been discovered [20]; but the most intriguing question has been whether there is d-wave superconductivity at $U/t \sim 8$ and 1/8 doping, and recent studies have shown that the ground state is stripe spin and charge order without superconductivity [21, 22, 23].

The attractive Hubbard model can be mapped to the repulsive Hubbard model through a particle-hole transition with the chemical potential μ mapping into a Zeeman field B. Being a sign-problem-free model at $B = 0$, it is possible to conduct accurate QMC simulations, and phenomena such as Kosterlitz–Thouless (KT) phase transition at finite temperature or the BCS-BEC (Bose-Einstein condensation) crossover has been studied [20, 24, 25, 26].

The Hubbard model on other geometries has attracted massive interest as well. The Hubbard model on honeycomb lattice is one of the easiest models to study the interplay of Dirac Fermions and electron-electron interactions. At half-filling, it is found that only above a critical point U_c would AF order occur [27, 28], which makes it the perfect playground for studying interaction-driven metal-insulator transition (MIT), an example of a quantum phase transition; a spin liquid phase was first found between the semi-metal phase and the AF phase [29], but later it was confirmed to be absent [30, 31]. The Hubbard model on a triangular lattice is one of the simplest model to study a frustrated system; the ground state is still under debate [32, 33] regarding whether there is an intermediate spin liquid phase between the metallic phase and the 120-deg magnetic order at

strong interaction. Kagome lattice is also commonly studied, which features a flat band at Dirac zone. These examples emphasize the incredible range of phenomena one can explore through the Hubbard model.

The physics displayed in the Hubbard model, including d-wave superconductivity, Mott insulator, antiferromagnetic (AF) order, stripe order, pseudogaps, Fermi liquid and strange metal behavior, is already fansinating by itself; what's even more appealing is that it's remarkably similar to that discovered in cuprates. Because of this, a major motivation of studying the Hubbard model also comes from the world of condensed matter experiments, especially that of cuprates. Measurements from Hubbard model calculations such as spectral function, current-current correlation function, simulated Raman results and local magnetic susceptibility can directly corresponding to experimental measurements from ARPES, Optical Conductivities, Raman Spectroscopy or NMR measurements (see Ref. [10] and references therein).

Out-of-equilibrium dynamics is another area where the Hubbard model proves to be really useful. Time-dependent calculations on the Hubbard model have shown an increase in d-wave pairing and charge or spin order strength [34, 35, 36] as well as the η-pairing mechanism [37], which gives insights into the experimental discovery of photo-induced superconductivity [38].

We shall stress again that the vast majority of these results were obtained via computational techniques such as QMC, DMRG, DMFT, Quantum cluster methods, DCA, and many more. Numerical methods have played and is still playing a crucial role on solving the Hubbard model, which contributes the broader range of condensed matter community.

1.3. Electron-phonon interaction

Despite this wide range of applications, the Hubbard model only involves the electron-electron interaction; if we compare with Eq. (1.2), we'd find that we have been ignoring the $U_{\text{ion}-\text{el}}$ term completely so far. The interaction with ions, or in a periodic system with translational symmetry, the lattice degrees of freedom, is introduced via "phonon", which is the collective mode of lattice vibrations. Thus the ion-electron interaction $U_{\text{ion}-\text{el}}$ gives rise to "electron-phonon" interactions in solid state materials.

1.3.1. The Holstein model. The simplest model for electron-phonon problem is *the Holstein model* [39]. The Hamiltonian reads

$$\hat{\mathcal{H}} = -t \sum_{\langle \mathbf{i},\mathbf{j}\rangle,\sigma} \left(\hat{c}^{\dagger}_{\mathbf{i}\sigma}\hat{c}_{\mathbf{j}\sigma} + \text{H.c.}\right) - \mu \sum_{\mathbf{i},\sigma} \hat{n}_{\mathbf{i},\sigma} + \frac{1}{2}\sum_{\mathbf{i}} \hat{P}^2_{\mathbf{i}} + \frac{\omega_0^2}{2}\sum_{\mathbf{i}} \hat{X}^2_{\mathbf{i}} + \lambda \sum_{\mathbf{i},\sigma} \hat{n}_{\mathbf{i},\sigma}\hat{X}_{\mathbf{i}} \ . \tag{1.11}$$

Similar to the Hubbard model, the sums on $\mathbf{i}$ and σ run over all lattice sites and spins $\sigma = \uparrow, \downarrow$, and $\langle \mathbf{i}, \mathbf{j}\rangle$ denotes nearest neighbors. $\hat{c}^{\dagger}_{\mathbf{i}\sigma}$ and $\hat{c}_{\mathbf{i}\sigma}$ are creation and annihilation operators of electrons with spin σ on a given site $\mathbf{i}$; $\hat{n}_{\mathbf{i},\sigma} = \hat{c}^{\dagger}_{\mathbf{i}\sigma}\hat{c}_{\mathbf{i}\sigma}$ is the number operator.

The first term of Eq. (1.11) corresponds to the hopping of electrons $\mathcal{K}_{\text{el}}$, as in Eq. (1.6), with chemical potential μ term next.

The next two terms, $\mathcal{H}_{\text{ph}}$ of the Hamiltonian, describes optical phonons, with $\frac{1}{2}\sum_{\mathbf{i}} \hat{P}^2_{\mathbf{i}}$ being the phonon kinetic energy $\mathcal{K}_{\text{ph}}$ and $\frac{\omega_0^2}{2}\sum_{\mathbf{i}} \hat{X}^2_{\mathbf{i}}$ being the phonon potential energy $\mathcal{V}_{\text{ph}}$. Phonon position and momentum operators are denoted by $\hat{X}_{\mathbf{i}}$ and $\hat{P}_{\mathbf{i}}$ respectively. The phonons are local quantum harmonic oscillators of frequency ω_0 on each site, and dispersionless since there are no terms connecting $\hat{X}_{\mathbf{i}}$ on different sites of the lattice. The phonon mass M is eliminated because is set to unity.

An equivalent way to express the phonon terms is through the phonon creation and annihilation operators $\hat{a}_{\mathbf{i}}$ and $\hat{a}^{\dagger}_{\mathbf{i}}$

$$\begin{aligned} \hat{a}_{\mathbf{i}} &= \sqrt{\frac{\omega_0}{2}}\left(\hat{X}_{\mathbf{i}} + \frac{i}{\omega_0}\hat{P}_{\mathbf{i}}\right) \\ \hat{a}^{\dagger}_{\mathbf{i}} &= \sqrt{\frac{\omega_0}{2}}\left(\hat{X}_{\mathbf{i}} - \frac{i}{\omega_0}\hat{P}_{\mathbf{i}}\right) \ , \end{aligned} \tag{1.12}$$

and the phonon energy can be expressed by

$$\hat{\mathcal{H}}_{\text{ph}} = \omega_0 \left(\hat{N}_{\mathbf{i}} + \frac{1}{2}\right), \tag{1.13}$$

where $\hat{N}_{\mathbf{i}} = \hat{a}^{\dagger}_{\mathbf{i}}\hat{a}_{\mathbf{i}}$ is the phonon number operator. $\hbar$ is set to 1 for simplicity.

The final term of Eq. (1.11) is the key term of the Holstein Hamiltonian. It describes on-site electron-phonon interactions with electrons coupled to the local phonon displacement with coupling strength λ.

Again it's important to explain the units in the Holstein model. We have established previously that t and μ have unit of energy; it's obvious that phonon energy ω_0 is the same. Using t as the energy scale, phonon displacement and momentum operators $\hat{X}_{\mathbf{i}}$ and $\hat{P}_{\mathbf{i}}$ then have units of $[1/\sqrt{t}]$ and $\sqrt{t}$ respectively. That leaves electron-phonon coupling λ to be unit of $t^{3/2}$. To simplify discussions, we introduce a "dimensionless coupling" $\lambda_D = \frac{\lambda^2}{\omega_0^2 W}$, which is unitless.

We can also express the Holstein model, or electron-phonon models in general, in the momentum space,

$$\hat{\mathcal{H}} = \sum_{\mathbf{k},\sigma} \epsilon(\mathbf{k})\, \hat{c}^\dagger_{\mathbf{k}\sigma} \hat{c}_{\mathbf{k}\sigma} + \sum_{\mathbf{q}} \omega(\mathbf{q})\, \hat{a}^\dagger_{\mathbf{q}} \hat{a}_{\mathbf{q}} + \frac{1}{\sqrt{N}} \sum_{\mathbf{k},\mathbf{q},\sigma} g(\mathbf{q})\, \hat{c}^\dagger_{\mathbf{k}+\mathbf{q}} \hat{c}_{\mathbf{k}\sigma} (\hat{a}^\dagger_{-\mathbf{q}} + \hat{a}_{\mathbf{q}}) \ . \tag{1.14}$$

The first two terms describe electronic band structure and phonon dispersion relation respectively. For Holstein model, coupling $g(\mathbf{q})$ is a constant that's independent of $\mathbf{q}$; another form of electron-phonon coupling, the so-called Fröhlich model, has $g(\mathbf{q}) \propto 1/|\mathbf{q}|$ [40].

We can gain first insights of the Holstein model from the one site limit. The electron hopping term t is set to zero, so the Hamiltonian reduces to a collection of independent terms

$$\hat{\mathcal{H}} = \frac{1}{2}\hat{P}^2 + \frac{\omega_0^2}{2}\hat{X}^2 + \lambda \hat{X}(\hat{n}_\uparrow + \hat{n}_\downarrow) - \mu(\hat{n}_\uparrow + \hat{n}_\downarrow) \ . \tag{1.15}$$

We can complete the square on phonon displacement $\hat{X}$,

$$\hat{\mathcal{H}} = \frac{1}{2}\hat{P}^2 + \frac{\omega_0^2}{2}\left[\hat{X} + \frac{\lambda}{\omega_0^2}(\hat{n}_\uparrow + \hat{n}_\downarrow)\right]^2 - \frac{1}{2}\frac{\lambda^2}{\omega_0^2}(\hat{n}_\uparrow + \hat{n}_\downarrow)^2 - \mu(\hat{n}_\uparrow + \hat{n}_\downarrow) \,, \tag{1.16}$$

so that the first two terms form a shifted harmonic oscillator with equilibrium position $X_0 = \frac{\lambda}{\omega_0^2}(n_\uparrow + n_\downarrow)$, and there is now an attractive electron-electron interaction with effective coupling strength

$$U_{\text{eff}} = -\frac{\lambda^2}{\omega_0^2} \,. \tag{1.17}$$

For one site, there are only four states for the electrons $|n_\uparrow, n_\downarrow\rangle = |0,0\rangle$, $|0,1\rangle$, $|1,0\rangle$ and $|1,1\rangle$, so the model can be solved analytically. The potential energy of this one site limit forms a double-well structure, with the two minimum corresponding to $n = 0$ and $n = 2$, as shown in Fig. 1.2. This presents a basic physics picture of the Holstein model: an effective attractive electron-electron

interaction is introduced through the electron-phonon interaction, and the lowest energy occurs at either doubly occupied sites or empty sites.

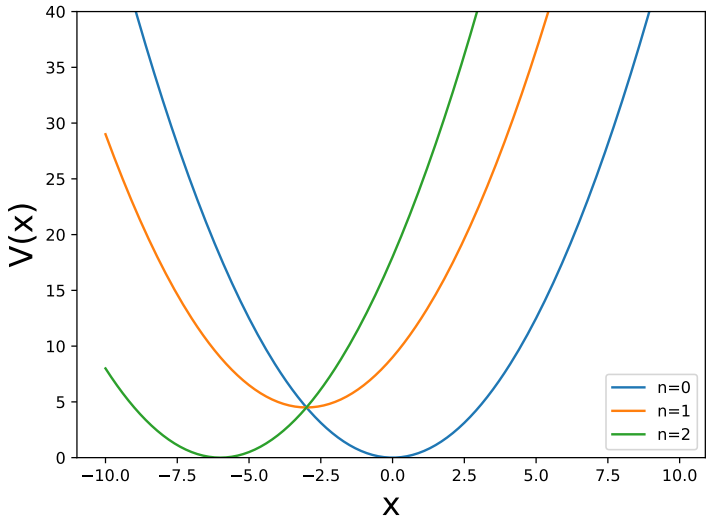

FIGURE 1.2. Potential energy of the Holstein model at one site limit.

Because of this degenerate low energy state at doubly occupied sites or empty sites, the Holstein model at half-filling is a perfect playground for studying charge order. Early Quantum Monte Carlo studies [41, 42, 43, 44, 45, 46] and DMFT studies [47, 48] in the 1990s have focused on charge density wave and the competition with superconductivity. Recent studies on a 1D chain or 2D square lattice [49, 50, 51, 52] have analyzed more closely the CDW phase transition, including locating the transition temperature at different coupling strength λ, as well as looking at the effect of dispersion of phonons [53] or the effect of strain [54]. Studies on a triangular lattice [55] have found an enhancement of superconductivity due to frustration of charge order whereas studies of Dirac fermions [3, 56, 57, 58] have discovered a critical point from semi-metal to CDW insulator. Superconductivity order analyzed more carefully away from half-filling [59], but simulations are more costly because of the lower transition temperature for the SC order. In a real material, both electron-electron and electron-phonon interactions exist, and in some cases the energy scale is comparable; so studies on the Hubbard-Holstein model have also been a hot area [46, 49, 60].

Another trend of study of the Holstein model has focused on the "Holstein polaron" [61, 62, 63, 64, 65, 66, 67]; in fact, the Holstein model was initially proposed to address the polaron problem. A

polaron is a quasiparticle describing a conduction electron (or hole) together with its self-induced lattice polarization in an ionic crystal. Characterized by the polaron radius, Holstein polaron is usually called the small polaron, indicating the real-space deformation is short-ranged under strong coupling; the Fröhlich polaron describes large polaron with weak coupling. Bi-polaron state is also studied in the context of the pseudogap state [46, 68, 69].

1.3.2. The Su-Schrieffer-Heeger model. The complexity of phonon modes in real materials means that accounting for local Holstein phonons isn't enough to describe more complex situations. In this final section of introduction, we will introduce another well-studied model of electron-phonon interaction: the Su-Schrieffer-Heeger (SSH) model [70]. Instead of optical Holstein phonons that couple to the electron density of each site, SSH phonons account for the effect of lattice vibrations on the hopping of electrons. The optical SSH model Hamiltonian is therefore defined as

$$\mathcal{H} = -t \sum_{\langle \mathbf{i},\mathbf{j}\rangle,\sigma} \left(1 - \lambda \hat{X}_{\mathbf{ij}}\right)\left(\hat{c}^{\dagger}_{\mathbf{i}\sigma}\hat{c}_{\mathbf{j}\sigma} + \text{H.c.}\right) - \mu \sum_{\mathbf{i},\sigma} \hat{n}_{\mathbf{i},\sigma} + \sum_{\langle \mathbf{i},\mathbf{j}\rangle} \left[\frac{1}{2M}\hat{P}^2_{\mathbf{ij}} + \frac{K}{2}\hat{X}^2_{\mathbf{ij}}\right] . \tag{1.18}$$

Recent numerical studies on 1D or 2D system have established bond-order wave (BOW) as the ground state at half-filling, but unlike 1D systems where BOW exists for any non-zero coupling, in 2D systems BOW occurs only above a coupling strength [71, 72, 73, 74, 75, 76]. AF induced by electron-phonon interaction was also discovered via SSH model or SSH+U model very recently [77, 78, 79] The SSH was originally motivated by polyacetylene physics, but it also plays an essential role in recent years in studies of topological insulators.

1.4. Summary

We have introduced physics phenomena such as superconductivity and charge density wave, and the model Hamiltonians proposed in order to study them, such as the Hubbard model, the Holstein model and the SSH model. In the next two chapters, we will introduce *how* to study them —the tools used in computational condensed matter physics, more specifically the quantum Monte Carlo methods (in chapter 2) and exact diagonalization (in chapter 3). From chapter 4 to chapter 7, we will present four studies on these topics: two of them focus on the effect of electron-phonon interactions on Dirac Fermions (on the honeycomb lattice in chapter 4 and the π-flux lattice in chapter 5); chapter 6 presents a study of multi-orbital (layer) Holstein model and orbital-selective

behavior; a time-dependent study on a plaquette Hubbard model is given in chapter 7. Finally in chapter 8, we will present a summary and conclusion, as well as an outlook for future works.

CHAPTER 2

Methodologies I: The Quantum Monte Carlo (QMC) Method

The quantum Monte Carlo (QMC) method has played a huge role in the history of strongly correlated systems in the condensed matter community, as mentioned in the previous chapter. Here we will introduce quantum Monte Carlo starting from the basics of classical Monte Carlo, and the idea of quantum Monte Carlo and path integrals. Then we will describe in detail two of its variants, namely the determinant quantum Monte Carlo (DQMC) and the Langevin quantum Monte Carlo.

2.1. Introduction to the Monte Carlo method

The Monte Carlo Method includes a broad range of computational methods that's becoming increasingly important in not only physics, but also natural sciences, mathematics, engineering and even social sciences [80]. It has roots in statistics and approaches problems with the simple idea of *important sampling*.

A classic example of the random sampling is "children on the beaches of Monaco" to calculate the area of a circle: they first draw a large circle and a square directly containing it; then they randomly threw pebbles into the square, and count how many of them land inside the circle, comparing to the total number of pebbles. As we know, the radio of area of within the circle over the area of the square is $\pi/4 \approx 0.7854$. Fig. 2.1 shows such a simulation, with sample size $N = 5000$, π is calculated to be 3.1168. With sample size larger and larger, the estimation will get closer and closer to the correct results. This is the idea of Monte Carlo sampling: when the analytical calculation is hard to achieve, we can randomly sample the distribution, and when the sample size is large enough, the estimate results will converge to the correct results.

A slightly more sophisticated version of the Monte Carlo method is *Markov Chain* sampling. When the "square on the beach" gets too large so that the children cannot cover the whole area by throwing pebbles from outside, a modified method is used: one would throw a pebble first inside the square, then walk to where it lands, and throw again from this location; but if it lands outside

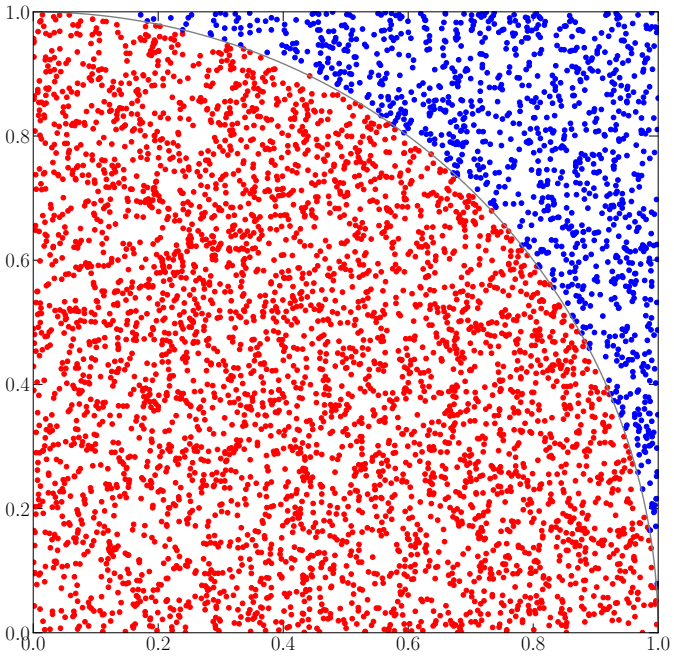

FIGURE 2.1. The game of "children on the beaches of Monaco". 1/4 of a square is drawn, with sample size $N = 5000$, π is calculated to be $\pi \approx 3.1168$.

of the square, they would not move and simply re-throw the pebble, until when it lands inside the square. Now the distance that can be covered is much larger than only throwing from the outside, and when enough steps have been made, everywhere inside the square on the beach can be reached.

We now introduce Monte Carlo in a more formal way. We know from statistical mechanics that, in a system with many states $|n\rangle$, each associated with energy E_n, the probability of finding the system in state n is given by Boltzmann distribution

$$\pi(n) = \frac{1}{Z} e^{-\beta E_n} , \tag{2.1}$$

where $\beta = 1/k_B T$ is the inverse temperature and

$$Z = \sum_n e^{-\beta E_n} \tag{2.2}$$

is the partition function. Any observable A can be calculated as

$$\langle A \rangle = \sum_n \pi(n) A_n = \frac{1}{Z} A_n e^{-\beta E_n} , \tag{2.3}$$

where A_n is the value of A in the state n.

The Monte Carlo method generates states or configurations randomly, according to probability $\pi(n)$. In the case of Markov Chain sampling, probability of each step only depends on the step before $p(n_j|n_j \cdots n_1) = p(n_j|n_{j-1})$. There are two ingredients that are essential for the Monte Carlo method to work. One of them is **ergodicity**, i.e. all possible configurations should be reachable within a finite number of Monte Carlo steps; the other is **detailed balance**

$$\pi(m)P(m \to n) = \pi(n)P(n \to m) \tag{2.4}$$

where $\pi(m)$ is the probability of finding the system in state m and $P(m \to n)$ is the probability to move from state m to n.

One widely used Monte Carlo algorithm is called the *Metropolis Algorithm*, which accepts a move from m to n with a probability

$$p(m \to n) = \min\big[1, \frac{\pi(n)}{\pi(m)}\big]\,, \tag{2.5}$$

i.e. if the probability $\pi(n) > \pi(m)$ then accept the move; if not, get an uniformly distributed random number $0 < R < 1$ and accept the move if $R < \pi(n)/\pi(m)$, otherwise reject the move. It can easily be shown that the Metropolis algorithm satisfies detailed balance.

In a statistics physics context,

$$\pi(n)/\pi(m) = e^{-\beta E_n}/e^{-\beta E_m} = e^{-\beta \Delta E} \tag{2.6}$$

where $\Delta E = E_n - E_m$. In another words, instead of analytically *calculating* the Boltzmann distribution and partition function and other variables, the Monte Carlo method only requires the knowledge of the difference in energy ΔE, then it *samples* the Boltzmann distribution, and according to the Law of large numbers, Monte Carlo results will converge to the correct Boltzmann distribution with enough steps.

2.2. Quantum Monte Carlo and path integrals

Now we move on to quantum systems. We start this section by writing down the partition function of a system

$$Z = \int dx e^{-\beta H(x)} = \int dx\, \rho(x, x, \beta) \tag{2.7}$$

where $\beta = 1/T$ is the inverse temperature (k_B is set to 1 for simplicity), x represents the degree of freedom in the system, for example the position; ρ is called the density matrix, which gives the probability of finding the system at position x. The density matrix can be used as the Boltzmann weight for Monte Carlo sampling. For some simple quantum systems such as free particle in a box or quantum harmonic oscillator (QHO), $\rho(x, x, \beta)$ can be evaluated explicitly, but for the vast majority of complicated quantum systems, $\rho(x, x, \beta)$ cannot be calculated analytically.

However, there are tools to help approach the problem. If a system's Hamiltonian can be written as

$$H = H^{\text{free}} + V\,, \tag{2.8}$$

where H^{free} describes the free particle Hamiltonian and V describes the interactions, the density matrix can then be expressed by the Trotter Formula

$$\rho(x, x', \beta) \xrightarrow{\beta \to 0} e^{-\frac{1}{2}\beta V(x)}\, \rho^{\text{free}}(x, x', \beta)\, e^{-\frac{1}{2}\beta V(x')}\,, \tag{2.9}$$

notice here we use both x and x' to include possible off-diagonal elements of the density matrix; also notice H^{free} and V may not commute, that is $H^{\text{free}}V \neq VH^{\text{free}}$, this introduces an error of the order $O\{\beta^2\}$.

The Trotter Formula is exact only as $\beta \to 0$, which is the high temperature limit. But the density matrix processes an useful property

$$\int dx'\, \rho(x, x', \beta_1)\, \rho(x', x'', \beta_2) = \rho(x, x'', \beta_1 + \beta_2)\,, \tag{2.10}$$

meaning by introducing a new variable x' and an integral over x', we can decompose β into β_1 and β_2. If the variable x is discrete, and if $\beta_1 = \beta_2$, we can use the discrete form

$$\sum_l \rho_{kl}\, \rho_{lm} = (\rho^2)_{km}\,, \tag{2.11}$$

which is the usual expression relatives matrix elements of ρ to those of its square, or "matrix squaring". Matrix squaring gives us a way to approach low temperature (large β) by breaking down β into small steps.

Combining matrix squaring with the Trotter formula, we arrive at

$$\begin{aligned}
Z &= \int dx_0\, \rho(x_0, x_0, \beta) \\
&= \int \cdots \int dx_0 \cdots dx_{N-1}\, \rho(x_0, x_1, \frac{\beta}{N}) \cdots \rho(x_{N-1}, x_0, \frac{\beta}{N}) \\
&= \int \cdots \int dx_0 \cdots dx_{N-1}\, e^{-\frac{1}{2}\beta V(x_0)}\, \rho^{\text{free}}(x_0, x_1, \beta)\, e^{-\frac{1}{2}\beta V(x_1)} \cdots \\
&\qquad\qquad e^{-\frac{1}{2}\beta V(x_{N-1})}\, \rho^{\text{free}}(x_{N-1}, x_0, \beta)\, e^{-\frac{1}{2}\beta V(x_0)} \\
&= \int \cdots \int dx_0 \cdots dx_{N-1}\, \rho^{\text{free}}(x_0, x_1, \beta) \cdots \rho^{\text{free}}(x_{N-1}, x_0, \beta)\, e^{-\beta V(x_0)} \cdots e^{-\beta V(x_{N-1})}\,.
\end{aligned} \tag{2.12}$$

The last step introduces an error of order $O\{(\beta/N)^2\}$. We have introduced a set of variables $\{x_0, x_1, \cdots, x_{N-1}\}$, which is called a "path", and broken down the integral over x_0 into N integrals over $\{x_0, x_1, \cdots, x_{N-1}\}$. This is called a "path integral". By doing this, we also break down the inverse temperature β into N steps $\Delta\tau = \beta/N$, so that the Trotter error is negligible as long as $\Delta\tau$ is chosen to be small enough. Because of the similarity of $e^{-\beta H}$ and $e^{-\mathrm{i}tH}$, the inverse temperature $\beta = \mathrm{i}t$ is often referred to as "imaginary time".

Over the years, many quantum Monte Carlo methods have been developed and proven very useful in solving quantum many-body models, including the determinant quantum Monte Carlo (DQMC) method [81], the Langevin quantum Monte Carlo method [2], stochastic series expansion (SSE) [82, 83], continuous-time quantum Monte Carlo (CT-QMC) [84, 85] and diagrammatic quantum Monte Carlo (DiagMC) [61], Green's function Monte Carlo (GF-MC) [86, 87] and diffusion Monte Carlo (DMC) [88], auxiliary-field quantum Monte Carlo (AFQMC) [89], and many others. The best method depends on the model being studied, for

example the SSE approach is especially powerful for quantum spin systems, while CT-QMC is effective in the weak interaction regime. In the following sections I will introduce in detail two of the variations, namely the determinant method and the Langevin method.

2.3. Determinant quantum Monte Carlo (DQMC)

The determinant quantum Monte Carlo (DQMC) method, sometimes also referred to as the BSS (Blankenbecler-Scalapino-Sugar) method, was developed in the early 1980s for Boson-Fermion problems [81, 90], coupled electron problems [91, 92], as well as quantum impurity models [93], and has been instrumental in numerical studies of quantum many-body problems and the broader condensed matter communities for decades. Being a non-perturbative method with no approximations made, it is intrinsically exact and unbiased with only statistical errors, which makes it applicable for a wide range of models, as well as giving comparison with other theoretical or computational methods or experimental results. As with many Monte Carlo methods, a limitation is the size of the system which can be studied. In this section, we will present both the high-level idea and details of the DQMC formalism.

2.3.1. Multidimensional Gaussian integral: Before we start the description of the DQMC method, we first review a classical theorem that provides a useful analogy in the derivation, the multidimensional Gaussian Integral. The one dimensional Gaussian Integral

$$\int_{-\infty}^{+\infty} dx\, e^{-ax^2} = \frac{\sqrt{\pi}}{a} \tag{2.13}$$

can be generalized to multi-dimensions

$$Z = \int_{-\infty}^{+\infty} dx_1 \int_{-\infty}^{+\infty} dx_2 \cdots \int_{-\infty}^{+\infty} dx_N\, e^{-\vec{x}\mathbf{A}\vec{x}^T} = \frac{\pi^{N/2}}{\sqrt{\det \mathbf{A}}}\,, \tag{2.14}$$

where $\vec{x} = \{x_1, x_2, \cdots x_N\}$ is an N dimensional vector of real numbers, and $\mathbf{A}$ is a real, symmetric, N dimensional matrix. In other words, if the "action" is in quadratic form $S = \vec{x}\mathbf{A}\vec{x}^T$, it could be evaluated by the determinant of the matrix $\mathbf{A}$. Similarly we can calculate integrals when the integrand includes factors of x_i

$$Z^{-1} \int_{-\infty}^{+\infty} dx_1 \int_{-\infty}^{+\infty} dx_2 \cdots \int_{-\infty}^{+\infty} dx_N\, x_i x_j e^{-\vec{x}\mathbf{A}\vec{x}^T} = \frac{1}{2}\left[\mathbf{A}^{-1}\right]_{ij} \tag{2.15}$$

as well as

$$Z^{-1}\int_{-\infty}^{+\infty}dx_1\int_{-\infty}^{+\infty}dx_2\cdots\int_{-\infty}^{+\infty}dx_N\, x_ix_jx_kx_le^{-\vec{x}\mathbf{A}\vec{x}^T}$$
$$=\frac{1}{4}\left([\mathbf{A}^{-1}]_{ij}[\mathbf{A}^{-1}]_{kl}+[\mathbf{A}^{-1}]_{ik}[\mathbf{A}^{-1}]_{jl}+[\mathbf{A}^{-1}]_{il}[\mathbf{A}^{-1}]_{jk}\right). \tag{2.16}$$

Eq. (2.16) can also be written as

$$\langle x_ix_jx_kx_l\rangle=\langle x_ix_j\rangle\langle x_kx_l\rangle+\langle x_ix_k\rangle\langle x_jx_l\rangle+\langle x_ix_l\rangle\langle x_jx_k\rangle \tag{2.17}$$

meaning a quartic term can be expressed as a sum of product of quadratic terms, in all possible permutations. This identity is analogous to what is known as the "Wick's Theorem" in quantum field theory.

2.3.2. DQMC formalism: Now that we have reviewed the classical multidimensional Gaussian Integral, we will use the (quantum) single band Hubbard model

$$\hat{H}=\underbrace{-t\sum_{\langle\mathbf{i},\mathbf{j}\rangle,\sigma}(\hat{c}^\dagger_{\mathbf{i}\sigma}\hat{c}_{\mathbf{j}\sigma}+\text{H.c.})-\mu\sum_{\mathbf{i}}(\hat{n}_{\mathbf{i}\uparrow}+\hat{n}_{\mathbf{i}\downarrow})}_{\hat{K}}+\underbrace{U\sum_{\mathbf{i}}(\hat{n}_{\mathbf{i}\uparrow}-\frac{1}{2})(\hat{n}_{\mathbf{i}\downarrow}-\frac{1}{2})}_{\hat{V}} \tag{2.18}$$

to help describe the formalism of DQMC.

We start with the partition function, where we can employ the identity

$$\text{Tr}\, e^{-\beta\hat{H}}=\det\left[\mathbf{I}+e^{-\beta\mathbf{H}}\right] \tag{2.19}$$

when $\hat{H}$ is quadratic in Fermionic operators $\hat{H}=\hat{c}^\dagger\mathbf{H}\hat{c}$. The trace is over the 2^N dimensional Hilbert space of Fermionic operators. The one-body part K of Eq. (2.18) is in quadratic form, but the interaction part V is in quartic form, so we cannot use Eq. (2.19). To solve this problem, we introduce the (discrete) Hubbard-Stratonovich (HS) transformation,

$$e^{-U\Delta\tau(n_{\mathbf{i}\uparrow}-\frac{1}{2})(n_{\mathbf{i}\downarrow}-\frac{1}{2})}=\frac{1}{2}e^{-\frac{U\Delta\tau}{4}}\sum_{S_{\mathbf{i}}}e^{\lambda S_{\mathbf{i}}(n_{\mathbf{i}\uparrow}-n_{\mathbf{i}\downarrow})} \tag{2.20}$$

where $\cosh\lambda=e^{\frac{U\Delta\tau}{2}}$, and $S_{\mathbf{i}}=\pm1$ is an Ising-like variable. The HS transformation enables us to express the V term also as a quadratic form by introducing an additional field $S_{\mathbf{i}}$ on each site.

Now that both terms in the Hubbard Hamiltonian can be written in quadratic form, we can follow up on eq. (2.19) and use the idea introduced in previous section, and write the partition function in path integral form

$$
\begin{aligned}
Z &= \int \mathcal{D}S_{\mathbf{i},\tau}\ \mathrm{Tr}\ e^{-\beta\hat{H}} = \int \mathcal{D}S_{\mathbf{i},\tau} \mathrm{Tr}\, e^{-\Delta\tau\hat{H}} \cdots e^{-\Delta\tau\hat{H}} \\
Z &= \int \mathcal{D}S_{\mathbf{i},\tau}\ \mathrm{Tr}\ e^{-\Delta\tau\hat{K}} e^{-\Delta\tau\hat{V}} \cdots e^{-\Delta\tau\hat{K}} e^{-\Delta\tau\hat{V}} \\
&= \int \mathcal{D}S_{\mathbf{i},\tau} \det\left[\mathbf{I} + e^{-\Delta\tau\mathbf{K}} e^{-\Delta\tau\mathbf{V}(S_{\mathbf{i},1})} \cdots e^{-\Delta\tau\mathbf{K}} e^{-\Delta\tau\mathbf{V}(S_{\mathbf{i},L_\tau})}\right],
\end{aligned}
\tag{2.21}
$$

where L_τ is the number of imaginary time steps and the integral is over all possible states (or configurations). Notice each $\mathbf{V}$ matrix is a function of a set of HS field variable $\{S_{\mathbf{i},\tau}\}$, which has two indices, spatial site $\mathbf{i}$ and imaginary-time index τ, because the HS transformation must be applied for each term in Eq. (2.12). While $\mathbf{K}$ and $\mathbf{V}$ are N-dimensional matrices where N is the total number of sites, HS field $\{S_{\mathbf{i},\tau}\}$ is $N \times L_\tau$ dimensional, where L_τ is the number of imaginary time steps. The integral over all possible states can be expressed as an integral over all possible configurations of HS field as well. We also notice that, the two spin species can be separated so that the determinant can be calculated independently; the $\mathbf{K}$ matrix is the same for both up and down spin, but the $\mathbf{V}$ matrix will differ by a sign. So in the end we can write the partition function as

$$
Z = \int \mathcal{D}S_{\mathbf{i},\tau} \det \mathbf{M}_\uparrow \det \mathbf{M}_\downarrow \tag{2.22}
$$

where

$$
\mathbf{M}_\sigma = \mathbf{I} + e^{-\Delta\tau\mathbf{K}_\sigma} e^{-\mathbf{V}_\sigma(S_{\mathbf{i},1})} \cdots e^{-\Delta\tau\mathbf{K}_\sigma} e^{-\mathbf{V}_\sigma(S_{\mathbf{i},L_\tau})}. \tag{2.23}
$$

As an simple example, for a system of 1D chain with 4 sites with periodic boundary condition (PBC), the $\mathbf{K}$ and $\mathbf{V}$ matrix can be written as

$$\mathbf{K} = \begin{pmatrix} -\mu & -t & 0 & -t \\ -t & -\mu & -t & 0 \\ 0 & -t & -\mu & -t \\ -t & 0 & -t & -\mu \end{pmatrix}, \quad \mathbf{V}_\sigma(S_{\mathbf{i},\tau}) = \frac{U\lambda}{4} \begin{pmatrix} S_{1,\tau} & 0 & 0 & 0 \\ 0 & S_{2,\tau} & 0 & 0 \\ 0 & 0 & S_{3,\tau} & 0 \\ 0 & 0 & 0 & S_{4,\tau} \end{pmatrix}. \tag{2.24}$$

The last important part of the DQMC formalism is the measurement. The Fermionic Green's function can be measured by

$$G_\sigma(i,j) = \langle \hat{c}_{\mathbf{i}\sigma} \hat{c}^\dagger_{\mathbf{j}\sigma} \rangle = [\mathbf{I} + e^{-\Delta\tau \mathbf{K}_\sigma} e^{-\mathbf{V}_\sigma} \cdots e^{-\Delta\tau \mathbf{K}_\sigma} e^{-\mathbf{V}_\sigma}]^{-1}_{ij} = [\mathbf{M}_\sigma]^{-1}_{ij}, \tag{2.25}$$

and other quantities can be calculated from Green's function via Wick's theorem (2.17).

2.3.3. DQMC algorithm procedure: Here we present the key steps for a primitive DQMC algorithm:

- Initialize HS field $\{S_{\mathbf{i},\tau}\}$ randomly;
- Initialize and evaluate the exponential of matrices $e^{-\Delta\tau\mathbf{K}}$ and $e^{-\mathbf{V}_\sigma(S_{\mathbf{i},\tau})}$;
- Calculate $\det \mathbf{M} = \det\big[\mathbf{I} + e^{-\Delta\tau\mathbf{K}} e^{-\mathbf{V}_\sigma(S_{\mathbf{i},1})} \cdots e^{-\Delta\tau\mathbf{K}} e^{-\mathbf{V}_\sigma(S_{\mathbf{i},L_\tau})}\big]$ as well as the Green's function $\mathbf{G} = \mathbf{M}^{-1}$ using linear algebra library;
- Sweep through the HS field and suggest a move to each site: $S_{\mathbf{i},\tau} \to S'_{\mathbf{i},\tau} = -S_{\mathbf{i},\tau}$;
- Calculate the probability ratio $\frac{\pi(S'_{\mathbf{i},\tau})}{\pi(S_{\mathbf{i},\tau})} = \frac{\det \mathbf{M}'_\uparrow \det \mathbf{M}'_\downarrow}{\det \mathbf{M}_\uparrow \det \mathbf{M}_\downarrow}$;
- Get a random number $0 < R < 1$;
- Use the Metropolis algorithm: accept the move if $R < \frac{\pi(S'_{\mathbf{i},\tau})}{\pi(S_{\mathbf{i},\tau})}$, otherwise reject the move;
- Measure Green's functions $G_\sigma(i,j)$ and other quantities.

2.3.4. Important details: So far we have covered the basics of DQMC algorithm; there are, however, some "tricks" that are essential for a practical DQMC code, and we will introduce them in this subsection.

- Evaluating $\det \mathbf{M}$ is a very time consuming operation (scales as $O\{N^3\}$). To reduce computational cost, instead of directly calculating $\det \mathbf{M}'$ after each update, we use

$$\frac{\det \mathbf{M}'}{\det \mathbf{M}} = \det\big(\mathbf{M}^{-1}\mathbf{M}'\big) = \det\big(\mathbf{M}^{-1}(\mathbf{M} + d\mathbf{M})\big) = \det(I + \mathbf{G}d\mathbf{M}) \tag{2.26}$$

to calculate the ratio, where only $d\mathbf{M}$ is needed. When one HS field is updated, the $\mathbf{K}$ matrix stays the same and only one element in $\mathbf{V}$ changes. The CPU time for calculating the determinant ratio is therefore independent of N and L_τ.

However, we still need to calculate the Green's function matrix $\mathbf{G} = \mathbf{M}^{-1}$, and if the move is accepted, we need to update $\mathbf{G}$. Fortunately calculating $\mathbf{G}' = (\mathbf{M} + d\mathbf{M})^{-1}$ from $\mathbf{G} = \mathbf{M}^{-1}$ can also be simplified to an $O\{N^2\}$ operation, thanks to the fact that only one element in $\mathbf{V}$ is changed.

- Wrapping the Green's function. When the spatial sites on the same imaginary time slice τ are being updated, the calculation of Green's function requires matrix $\mathbf{M}$ to be written as

$$\mathbf{M} = \mathbf{I} + \mathbf{B}_{\tau+1} \cdots \mathbf{B}_L \mathbf{B}_1 \cdots \mathbf{B}_\tau \tag{2.27}$$

where $\mathbf{B}_\tau = e^{-\Delta\tau \mathbf{K}} e^{-\mathbf{V}_\sigma(S_{\mathbf{i},\tau})}$, i.e. the slice being updated needs to be at the end of the product. After all spatial sites on the same imaginary time slice τ is updated, we need to 'wrap' the Green's function to bring $\mathbf{B}_{\tau-1}$ to the end. This can be done via

$$\mathbf{I} + \mathbf{B}_\tau \cdots \mathbf{B}_L \mathbf{B}_1 \cdots \mathbf{B}_{\tau-1} = \mathbf{B}_\tau^{-1} \left[\mathbf{I} + \mathbf{B}_{\tau+1} \cdots \mathbf{B}_L \mathbf{B}_1 \cdots \mathbf{B}_\tau\right] \mathbf{B}_\tau \ . \tag{2.28}$$

- Time-dependent measurements. It's possible to calculate the full time-dependent Green's functions, $G_\sigma(i, j; \tau_1, \tau_2) = \langle \hat{c}_{\mathbf{i}\sigma}(\tau_1) \hat{c}^\dagger_{\mathbf{j}\sigma}(\tau_2) \rangle$, where i, j are spatial indices and τ_1, τ_2 are imaginary time slice indices, and to calculate other (physical) quantities from these (imaginary) time-dependent Green's functions, such as the susceptibility and spectral function (via analytic continuation, which is introduced in Appendix C). It's however computationally very costly to measure time-dependent Green's function [94].
- Local update and global update. We have described one type of update above, where we go to each imaginary time index τ and sweep through and update HS field on each spatial site $\mathbf{i}$. This is called the local update. Another type of update is called the global update, where for each step we randomly select a spacial site $\mathbf{i}$ and update all its imaginary-time slices. Usually a combination of local update and global update is implemented in a practical DQMC package, to improve the efficiency and accuracy of the simulation.

- Checkerboard decomposition [1, 95]. Exponentiating the kinetic matrix $\mathbf{K}$ (shown in eq. (2.24)) can be expensive, since it's not a diagonal matrix. To avoid this, we can use a trick called "checkerboard decomposition" which works when the $\mathbf{K}$ matrix is sparse. Again using the system of 1D chain as an example, we can split matrix $\mathbf{K}$ into $\mathbf{K}^{(1)} + \mathbf{K}^{(2)}$, and the exponential can be approximated by

$$e^{-\mathbf{K}} = e^{-\mathbf{K}^{(1)}} e^{-\mathbf{K}^{(2)}} + O\{(t\Delta\tau)^2\}\,, \tag{2.29}$$

where

$$e^{-\mathbf{K}^{(1)}} = \begin{pmatrix} e^{-\mathbf{D}} & & & \\ & e^{-\mathbf{D}} & & \\ & & \ddots & \\ & & & e^{-\mathbf{D}} \end{pmatrix}, e^{-\mathbf{K}^{(2)}} = \begin{pmatrix} \cosh(-t) & & & \sinh(-t) \\ & e^{-\mathbf{D}} & & \\ & & \ddots & \\ \sinh(-t) & & & \cosh(-t) \end{pmatrix}, \tag{2.30}$$

and $\mathbf{D}$ is a 2×2 matrix where

$$e^{-\mathbf{D}} = \begin{pmatrix} \cosh(-t) & \sinh(-t) \\ \sinh(-t) & \cosh(-t) \end{pmatrix}. \tag{2.31}$$

This is mathematically equivalent to a multiplication of N_b matrices $e^{\Delta\tau\mathbf{T}}$, N_b being the number of bonds, where each matrix

$$e^{\Delta\tau\mathbf{T}} = \begin{pmatrix} 1 & & & & & \\ & \ddots & & & & \\ & & \cosh(-\Delta\tau t) & \cdots & \sinh(-\Delta\tau t) & \\ & & \vdots & & \vdots & \\ & & \sinh(-\Delta\tau t) & \cdots & \cosh(-\Delta\tau t) & \\ & & & & & \ddots \\ & & & & & 1 \end{pmatrix} \tag{2.32}$$

has only 4 elements that differ from an identity matrix: $(e^{\Delta\tau\mathbf{T}})_{ii} = (e^{\Delta\tau\mathbf{T}})_{jj} = \cosh(-\Delta\tau t)$ as well as $(e^{\Delta\tau\mathbf{T}})_{ij} = (e^{\Delta\tau\mathbf{T}})_{ji} = \sinh(-\Delta\tau t)$ for the

matrix representing the bond connecting site **i** and site **j**. It needs to be done in the order of "groups" of the bonds which share no sites in common; an example of the grouping is shown in Fig. 2.2.

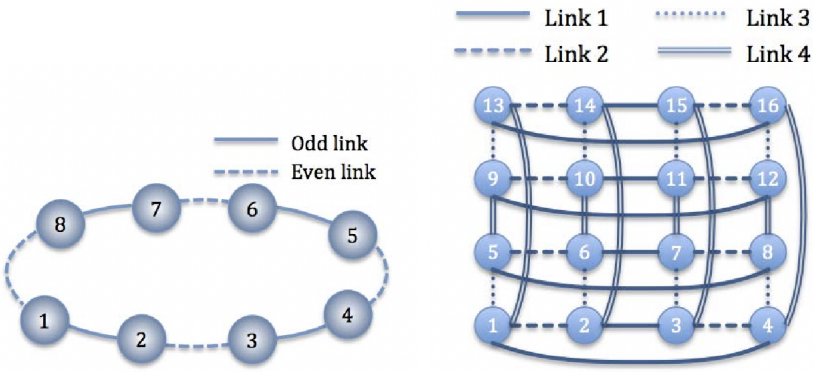

FIGURE 2.2. The mesh of a 1D ring (left) and 2D square lattice (right). Figure taken from Ref. [1].

- Numerical stabilization. Because each matrix elements are stored as a finite-precision number (usually 64 bits), the matrix production in **M** could become unstable in some parameter range, i.e. the matrix **M** is "ill-conditioned", when the ratio of largest to smallest eigenvalues become too high. In some cases, this ratio can get up to 10^{16}, which means a number stored as double-precision will lose its accuracy and become un-representable. Because of this, special "numerial stabilization" methods need to be performed to make the DQMC algorithm practical.

2.3.5. DQMC for Holstein model: So far we have described the DQMC formalism using the Hubbard model, in this subsection we will briefly cover DQMC for the Holstein model

$$\hat{H} = \underbrace{-t \sum_{\langle \mathbf{i},\mathbf{j}\rangle,\sigma} (\hat{c}^{\dagger}_{\mathbf{i}\sigma}\hat{c}_{\mathbf{j}\sigma} + H.c.) - \mu \sum_{\mathbf{i}} (\hat{n}_{\mathbf{i}\uparrow} + \hat{n}_{\mathbf{i}\downarrow})}_{\hat{K}} + \underbrace{\lambda \sum_{\mathbf{i}} \hat{x}_{\mathbf{i}} (\hat{n}_{\mathbf{i}\uparrow} + \hat{n}_{\mathbf{i}\downarrow})}_{\hat{V}} + \underbrace{\frac{\omega^2}{2} \sum_{\mathbf{i}} \hat{x}^2_{\mathbf{i}} + \frac{1}{2} \sum_{\mathbf{i}} \hat{p}^2_{\mathbf{i}}}_{\hat{H}_{ph}} \ . \tag{2.33}$$

The formalism and procedure is very similar to that of the Hubbard model, with two major differences. One is that the interaction term $\hat{V}$ is already a quadratic form (instead of a quartic form), so we don't need to perform a Hubbard-Stratonovich transformation to evaluate it; instead,

if we compare the right hand side of eq. (2.20) with the $\hat{V}$ term in (2.33), we can see the phonon field x in Holstein model acts in exactly the same way as the HS field in Hubbard model. So instead of sampling the HS field $S_{\mathbf{i},\tau}$, in the case of the Holstein model we'd sample the phonon field $x_{\mathbf{i},\tau}$, and the form of the matrices is the same with $S_{\mathbf{i},\tau} \to x_{\mathbf{i},\tau}$.

The second major difference is the addition of phonon part of the Hamiltonian $\hat{H}_{ph}$. Integrating over the phonon degrees of freedom gives the usual path integral for a quantum harmonic oscillator

$$\begin{aligned} Z_{ph} &= \int dx_{\mathbf{i},\tau} \langle x_{\mathbf{i},1}|e^{-\Delta\tau \hat{H}_{ph}}|x_{\mathbf{i},2}\rangle\langle x_{\mathbf{i},2}|e^{-\Delta\tau \hat{H}_{ph}}|x_{\mathbf{i},3}\rangle \cdots \langle x_{\mathbf{i},L_\tau}|e^{-\Delta\tau \hat{H}_{ph}}|x_{\mathbf{i},1}\rangle \\ &= \prod_{\tau} \exp\left\{ -\Delta\tau \left[\frac{\omega^2}{2} \sum_{\mathbf{i}} x_{\mathbf{i},\tau}^2 + \frac{1}{2} \sum_{\mathbf{i}} \left(\frac{x_{\mathbf{i},\tau} - x_{\mathbf{i},\tau-1}}{\Delta\tau} \right)^2 \right] \right\} \\ &= e^{-S_{ph}(\{x_{\mathbf{i},\tau}\})} \ , \end{aligned} \tag{2.34}$$

where $S_{ph}(\{x_{\mathbf{i},\tau}\})$ is called the *phonon action*. The total partition function can then be written as

$$Z = \int \mathcal{D}x_{\mathbf{i},\tau} \det \mathbf{M}_\uparrow \det \mathbf{M}_\uparrow \, e^{-S_{ph}} \ . \tag{2.35}$$

It worth pointing out that the $\mathbf{M}$ matrix is identical for up spin and down spin, unlike in the Hubbard model case where the $\mathbf{V}$ matrices differ by a sign. In other words

$$Z = \int \mathcal{D}x_{\mathbf{i},\tau} (\det \mathbf{M}_\sigma)^2 \, e^{-S_{ph}} \ . \tag{2.36}$$

From here onwards, the DQMC procedure is the same as in the case of the Hubbard model.

2.4. Langevin quantum Monte Carlo

The Langevin quantum Monte Carlo method, i.e. using Langevin dynamics to evolve the field instead of using Markov Chain Monte Carlo to sample the field, was first developed for lattice field theories [96] as well as electron-electron problem in the condensed matter community [97], and later developed for electron-phonon problems [2]. The method involves the calculation of $\mathbf{M}^{-1}\vec{g}$ using an iterative algorithm, as I will soon describe; for electron-electron interactions the number of iterations required becomes very large so that the method becomes impractical. Because of this, here we specifically discuss the Langevin method for electron-phonon problem where S_{ph} reduces the condition number of $\mathbf{M}$ and makes the calculations converge in a much smaller number of steps.

The formalism of the Langevin method is very similar to that of DQMC. Again using the Holstein model as an example, we start with the partition function, which is derived in the previous section

$$Z = \int \mathcal{D}x_{\mathbf{i},\tau} (\det \mathbf{M}_\sigma)^2 \, e^{-S_{ph}} \tag{2.37}$$

where

$$S_{ph} = -\Delta\tau \left[\frac{\omega^2}{2} \sum_{\mathbf{i}} x_{\mathbf{i},\tau}^2 + \frac{1}{2} \sum_{\mathbf{i}} \left(\frac{x_{\mathbf{i},\tau} - x_{\mathbf{i},\tau-1}}{\Delta\tau} \right)^2 \right] . \tag{2.38}$$

First we write it in the form

$$Z = \int \mathcal{D}x_{\mathbf{i},\tau} e^{-S} \tag{2.39}$$

where the "action" now includes the Fermionic contribution

$$S = S_{ph} - \ln (\det \mathbf{M})^2 \, , \tag{2.40}$$

then we introduce the Langevin equation governing the phonon field dynamics

$$\frac{dx_{\mathbf{i},\tau,t}}{dt} = -\frac{\partial S}{\partial x_{\mathbf{i},\tau,t}} + \sqrt{2}\eta_{\mathbf{i},\tau,t} \, , \tag{2.41}$$

with η being a stochastic variable. Notice that here we introduced a third index, t, of the phonon field x, where t is the Langevin time.

Now we need to discretize the Langevin equation. There are many ways to do it, the simplest being the Euler discretization

$$x_{\mathbf{i},\tau,t+dt} = x_{\mathbf{i},\tau,t} - dt \frac{\partial S}{\partial x_{\mathbf{i},\tau,t}} + \sqrt{2dt}\eta_{\mathbf{i},\tau,t} \, , \tag{2.42}$$

where the stochastic variable η satisfies

$$\langle \eta_{\mathbf{i},\tau,t} \rangle = 0 \, , \quad \langle \eta_{\mathbf{i},\tau,t} \eta_{\mathbf{j},\tau',t'} \rangle = \delta_{\mathbf{i},\mathbf{j}} \delta_{\tau,\tau'} \delta_{t,t'} \, . \tag{2.43}$$

This gives an error of $O\{dt\}$, dt being the Langevin time step. Other methods, such as the Runge-Kutta discretization, can reduce the error to $O\{dt^2\}$.

The key is to deal with the partial derivative of the action term, which can be evaluated by

$$\begin{aligned}\frac{\partial S}{\partial x_{\mathbf{i},\tau,t}} &= \frac{\partial S_{ph}}{\partial x_{\mathbf{i},\tau,t}} - \frac{\partial \ln\left(\det \mathbf{M}\right)^2}{\partial x_{\mathbf{i},\tau,t}} \\ &= \frac{\partial S_{ph}}{\partial x_{\mathbf{i},\tau,t}} - 2\,\mathrm{Tr}\left(\frac{\partial \mathbf{M}}{\partial x_{\mathbf{i},\tau,t}}\mathbf{M}^{-1}\right). \end{aligned} \tag{2.44}$$

Before we move on, it's worth mentioning that, previously we have defined the $\mathbf{M}$ matrix as

$$\mathbf{M} = \mathbf{I} + \mathbf{B}_1 \cdots \mathbf{B}_{L_\tau} \tag{2.45}$$

where $\mathbf{B}_\tau = e^{-\Delta\tau\mathbf{K}}e^{-\mathbf{V}}$ in the DQMC section, which is of dimension N and often referred to as the "small matrix" form. We could equally write the matrix as

$$\mathbf{M} = \begin{pmatrix} \mathbf{I} & -\mathbf{B}_2 & & & \\ & \mathbf{I} & -\mathbf{B}_3 & & \\ & & \ddots & \ddots & \\ & & & \mathbf{I} & -\mathbf{B}_{L_\tau} \\ \mathbf{B}_1 & & & & \mathbf{I} \end{pmatrix}, \tag{2.46}$$

which is a $NL_\tau \times NL_\tau$ dimension matrix, often referred to as the "large matrix" form, and will be used in the derivation of the Langevin method.

Of the two terms on the right hand side of eq. (2.44), the partial derivative of the phonon action is easy to calculate, but the trace term is expensive at $(O\{(NL_\tau)^3\})$. To avoid this, we instead use a Gaussian stochastic estimator to evaluate this term

$$2\,\mathrm{Tr}\left(\frac{\partial \mathbf{M}}{\partial x_{\mathbf{i},\tau,t}}\mathbf{M}^{-1}\right) \Rightarrow 2\vec{g}^T\left(\frac{\partial \mathbf{M}}{\partial x_{\mathbf{i},\tau,t}}\mathbf{M}^{-1}\right)\vec{g}\,. \tag{2.47}$$

Here $\vec{g}$ is a vector of Gaussianly distributed random numbers. Now instead of calculating the inverse of the matrix $\mathbf{M}$, we only need to calculate $\mathbf{M}^{-1}\vec{g}$, which can be done iteratively using the bi-conjugate gradient (CG) algorithm at $O\{NL_\tau\}$ cost.

We have so far introduced the core of Langevin quantum Monte Carlo method. One major remaining issue is the measurements. Of the two degrees of freedoms in the Holstein model, the phonons are easy to measure, since the phonon field is directly involved in the algorithm; the

Fermion quantities, however, are slightly more involved. We again approach this by calculating the Fermionic Green's function, which can be evaluated by

$$G_\sigma(i,j) = \langle \hat{c}_{\mathbf{i}\sigma} \hat{c}^\dagger_{\mathbf{j}\sigma} \rangle = \langle \mathbf{M}^{-1}_{i,j} \rangle = \langle \gamma_i (\mathbf{M}^{-1} \vec{\gamma})_j \rangle \ , \tag{2.48}$$

that is, using a Gaussian random number vector $\vec{\gamma}$ to calculate $\mathbf{M}^{-1}\vec{\gamma}$ via the CG algorithm. Once the Green's function is calculated, we can evaluate other electronic measurements via the Green's function and Wick's theorem (2.17). Although one needs to be careful when using Wick's theorem and calculating a product of two Green's functions: the error associated with the product of two Gaussian random numbers $\gamma_i \gamma_j$ can get really large, so different Gaussian vectors should be used for the two Green's functions.

The last thing we shall mention in this section is called "Fourier acceleration", a method introduced to reduce the long auto-correlation time often seen in simulations of electron-phonon systems. We first re-write the Langevin equation (2.41) as

$$\frac{d\vec{x}}{dt} = -Q \frac{dS}{d\vec{x}} + \sqrt{2Q}\eta \tag{2.49}$$

where Q is an arbitrary but positive definite matrix. The idea is to choose Q that helps reduce auto-correlation time. To achieve this, we notice that after Fourier transforming along the imaginary time axis, in the non-interacting limit,

$$\frac{d\tilde{S}}{d\tilde{x}_{\mathbf{i},k_\tau}} = (\Delta\tau\omega^2 + \frac{2 - 2\cos\frac{2\pi k_\tau}{L_\tau}}{\Delta\tau}) \tilde{x}_{\mathbf{i},k_\tau} \tag{2.50}$$

where $-\frac{L_\tau}{2} + 1 \leqslant k_\tau \leqslant \frac{L_\tau}{2}$. The ratio of slowest to fastest phonon mode is

$$\frac{(\Delta\tau\omega)^2}{4 + (\Delta\tau\omega)^2} \ll 1 \ , \tag{2.51}$$

meaning the critical slow down happens at small $\Delta\tau$. To compensate, we choose Q to be

$$\tilde{Q}(k_\tau) = \frac{\Delta\tau^2\omega^2 + 4}{\Delta\tau^2\omega^2 + 2 - 2\cos\frac{2\pi k_\tau}{L_\tau}} \ . \tag{2.52}$$

Even though this form is motivated by non-interacting results, it works very well for $\lambda \neq 0$ situations.

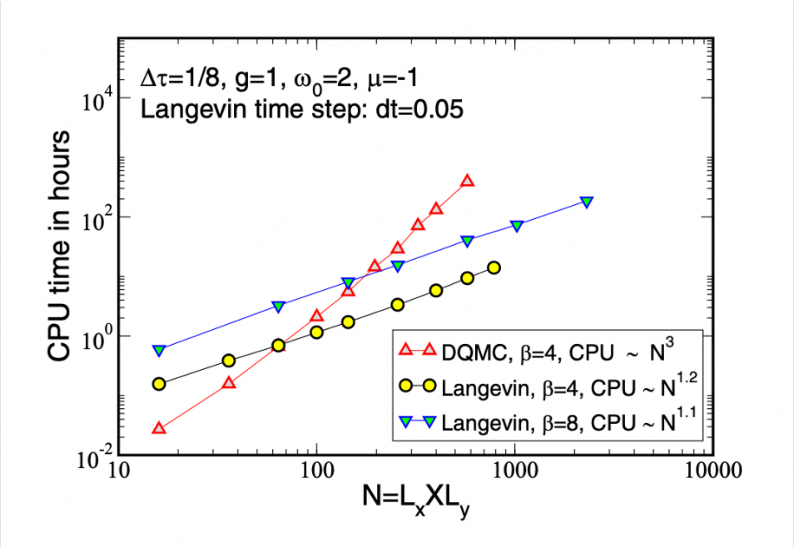

FIGURE 2.3. CPU time as a function of system size for DQMC (red triangles) and Langevin (yellow circles; blue triangles) algorithms. System temperature $\beta = 4$ is used for DQMC and $\beta = 4$, 8 for Langevin. Figure taken from Ref. [2].

Comparing to the DQMC method which scales as $O\{N^3 L_\tau\}$, Langevin method scales as $O\{N L_\tau\}$, i.e. linearly in both spatial size N and imaginary-time dimension L_τ, which makes it much easier to push for larger lattice sizes and greatly reduce finite size effects. Fig. 2.3 shows a comparison of CPU time in DQMC simulation and Langevin simulation of the same system, where the advantage of Langevin method can be clearly seen.

2.5. The "Sign Problem"

The infamous "Sign Problem" [11] has been the main obstacle for quantum Monte Carlo research for decades.

We have established the Boltzmann weight for a given configuration in Hubbard model in eq. (2.22) as

$$\pi(c) = \pi(\{S_{\mathbf{i},\tau}\}) = \det \mathbf{M}_\uparrow \det \mathbf{M}_\downarrow \,, \tag{2.53}$$

where

$$\mathbf{M}_\sigma = \mathbf{I} + e^{-\Delta\tau \mathbf{K}_\sigma} e^{-\mathbf{V}_\sigma(S_{\mathbf{i},1})} \cdots e^{-\Delta\tau \mathbf{K}_\sigma} e^{-\mathbf{V}_\sigma(S_{\mathbf{i},L_\tau})} \,. \tag{2.54}$$

We use the notation $c \equiv \{S_{\mathbf{i},\tau}\}$ to represent a given configuration of the HS field. As we have said before, $\mathbf{M}_\uparrow$ and $\mathbf{M}_\downarrow$ are not equal, because of a sign difference for matrix $\mathbf{V}$. So the Boltzmann weight can be either positive or negative since each individual $\det \mathbf{M}$ can be either positive or negative. This introduces a problem that a negative Boltzmann weight cannot be used in Monte Carlo sampling. One possible way to deal with this is to simply employ the absolute value $|\pi(\{S_{\mathbf{i},\tau}\})|$ as the sampling weight; in which case each observable is measured as

$$\langle \hat{O} \rangle = \frac{\sum_{\{S_{\mathbf{i},\tau}\}} \hat{O}\pi(\{S_{\mathbf{i},\tau}\})}{\sum_{\{S_{\mathbf{i},\tau}\}} \pi(\{S_{\mathbf{i},\tau}\})} = \frac{\sum_c O(c)\mathrm{sign}(c)|\pi(c)|/\sum_c |\pi(c)|}{\sum_c \mathrm{sign}(c)|\pi(c)|/\sum_c |\pi(c)|} = \frac{\langle \hat{O} \rangle_{|w|}}{\langle \mathrm{sign} \rangle_{|w|}} \tag{2.55}$$

where $\pi(c) = \mathrm{sign}(c)|\pi(c)|$. The problem is that the average sign $\langle \mathrm{sign} \rangle_{|w|}$ gets exponentially small with system size and imaginary time $\langle \mathrm{sign} \rangle_{|w|} \sim e^{-NL_\tau}$, so that the statistical errors of measuring $\langle \hat{O} \rangle$ gets exponentially large, to the point it becomes unusable. This is the so-called "Sign Problem". Many studies since have focused on finding QMC approaches to avoid the sign problem [98], for example using more complex Fermion or Majorana Fermion representation [99].

Fortunately, there are some models and/or parameter regimes that don't suffer from the sign problem. One example is the Holstein model, where the matrix $\mathbf{M}$ is identical for up spin and down spin, so that Boltzmann weight

$$\pi(\{x_{\mathbf{i},\tau}\}) = (\det \mathbf{M}_\sigma)^2 \, e^{-S} \tag{2.56}$$

is always positive. Another example is the Hubbard model at half filling, i.e. $\langle \hat{n}_\mathbf{i} \rangle = 1$, which is also sign problem free because of particle-hole symmetry.

CHAPTER 3

Methodologies II: Exact Diagonalization (ED) Method

The Exact Diagonalization (ED) method [100, 101] is another technique that's widely used in solving many-body systems. When the system can be described with a discrete and finite set of basis states, the Hamiltonian is written in a matrix form in this basis and diagonalized using a linear algebra library. It provides access to some quantities that are hard to obtain from other numerical methods, such as directly calculating ground state and low energy excited states and their properties, or real time dynamics; but due to the fact that Hilbert space grows exponentially with system sizes, it's only feasible for systems with a few tens of sites.

Unlike the QMC method described in previous chapter, the bottleneck for ED method isn't CPU time in most cases. For a Hubbard system with N sites, there are 2^N possible states (or 4^N considering both spin species); if we work in the canonical ensemble and fix the number of electrons n_e, then the size of Hilbert space is

$$\frac{N!}{n_e!(N-n_e)!} = \binom{N}{n_e} . \tag{3.1}$$

As an example, consider an electron system with 36 sites and 6 electrons. The size of its Hilbert space is $\binom{36}{6} = 1947792$, or about 2×10^6; if each matrix element is stored as double precision number, it requires 16×1947792^2 bytes, or 55 TeraBytes of RAM. So memory is usually the main issue for ED simulations. Because of this memory limitation, special "tricks" are needed for study of sufficiently large systems. Using symmetries is a common practice to make the matrix block diagonal, such as SU(2) spin symmetry, particle-hole symmetry, translational symmetries and inversion symmetry. This matrix is usually also very sparse, which makes it suitable for approaches like the Lanczos method.

3.1. The Lanczos method

The Lanczos algorithm [102] is an iterative method that's efficient in finding the M smallest eigenvalues and their corresponding eigenvectors of an $N \times N$ Hermitian matrix $\mathbf{H}$, where $M \ll N$. The idea is to start from a random state $|\phi\rangle$, find the direction of steepest-descent, move in this direction so that energy expectation $\langle\phi|H|\phi\rangle$ is lower, and repeat this until it converges to ground state.

We start with a random state $|\tilde{\phi}_1\rangle$, normalize it, and calculate it's energy expectation

$$\begin{aligned} b_1 &= \sqrt{\langle\tilde{\phi}_1|\tilde{\phi}_1\rangle}\,, \\ |\phi_1\rangle &= \frac{|\tilde{\phi}_1\rangle}{b_1}\,, \\ a_1 &= \langle\phi_1|H|\phi_1\rangle\,. \end{aligned} \tag{3.2}$$

Then we obtain the next state by orthogonalizing $H|\phi_1\rangle$ to $|\phi_1\rangle$ and normalizing it,

$$\begin{aligned} |\tilde{\phi}_2\rangle &= H|\phi_1\rangle - a_1|\phi_1\rangle\,, \\ b_2 &= \sqrt{\langle\tilde{\phi}_2|\tilde{\phi}_2\rangle}\,, \\ |\phi_2\rangle &= \frac{|\tilde{\phi}_2\rangle}{b_2}\,, \\ a_2 &= \langle\phi_2|H|\phi_2\rangle\,. \end{aligned} \tag{3.3}$$

Repeat this process, notice only the previous two states are needed for the next state

$$\begin{aligned} |\tilde{\phi}_{n+1}\rangle &= H|\phi_n\rangle - a_n|\phi_n\rangle - b_n|\phi_{n-1}\rangle\,, \\ b_{n+1} &= \sqrt{\langle\tilde{\phi}_{n+1}|\tilde{\phi}_{n+1}\rangle}\,, \\ |\phi_{n+1}\rangle &= \frac{|\tilde{\phi}_{n+1}\rangle}{b_{n+1}}\,, \\ a_{n+1} &= \langle\phi_{n+1}|H|\phi_{n+1}\rangle\,. \end{aligned} \tag{3.4}$$

Repeat this M times. We get

- an $N \times M$ dimension matrix $\mathbf{V} = [\phi_1, \phi_2, \cdots, \phi_M]$;

- a tridiagonal $M \times M$ matrix $\mathbf{T} = \begin{pmatrix} a_1 & b_2 & & & & \\ b_2 & a_2 & b_3 & & & \\ & b_3 & a_3 & b_4 & & \\ & & \ddots & \ddots & \ddots & \\ & & & b_{M-1} & a_{M-1} & b_M \\ & & & & b_M & a_M \end{pmatrix}$.

The final step of the process is to find eigenvalues and eigenvectors of the tridiagonal matrix $\mathbf{T}$, i.e. $\mathbf{T}|\psi\rangle = \lambda|\psi\rangle$, which is much cheaper than finding eigenvalues and eigenvectors of a general matrix. In the cases where $M \ll N$, the reduce in size saves much CPU time as well. The λ associated with $\mathbf{T}$ is also an eigenvalue of the original matrix $\mathbf{H}$, and $|\Phi\rangle = \mathbf{V}|\psi\rangle$ is eigenvector of $\mathbf{H}$ (if $M = N$), since

$$\mathbf{H}|\Phi\rangle = \mathbf{H}\mathbf{V}|\psi\rangle = \mathbf{V}\mathbf{T}\mathbf{V}^*\mathbf{V}|\psi\rangle = \mathbf{V}\mathbf{T}|\psi\rangle = \mathbf{V}\lambda|\psi\rangle = \lambda(\mathbf{V}|\psi\rangle) = \lambda|\Phi\rangle\,. \tag{3.5}$$

The subspace $\mathcal{K}^M(|\phi_1\rangle) = \big[|\phi_1\rangle, \mathbf{H}|\phi_1\rangle, \mathbf{H}^2|\phi_1\rangle, \cdots, \mathbf{H}^M|\phi_1\rangle, \big]$ is called the (M+1)-dimensional *Krylov space*. The Lanczos method is one of the standard technique in solving the eigenvalue problem, and can often be found in modern linear algebra library.

3.2. Time-dependent ED

One advantage of the ED method is the ability to apply it to real time dynamics and out-of-equilibrium systems, which is increasingly becoming one of the focal point in studies of strongly correlated systems. Here we describe the procedure of using Lanczos to calculate real time dynamics [**103**, **104**].

Starting from the time-dependent Schrödinger equation

$$i\frac{\partial\Psi(t)}{\partial t} = H(t)\Psi(t) \tag{3.6}$$

where the time-dependent wavefunction is

$$|\Psi(t)\rangle = e^{-iHt}|\Psi(0)\rangle\,. \tag{3.7}$$

We discretize time and employ the Lanczos eigenvalues and eigenvectors,

$$|\Psi(t+dt)\rangle = e^{-iH(t)dt}|\Psi(t)\rangle \approx \mathbf{V}(t)e^{-i\mathbf{T}(t)dt}\mathbf{V}^T(t)|\Psi(t)\rangle\,, \tag{3.8}$$

where $\mathbf{V}(t)$ and $\mathbf{T}(t)$ are calculated from $\mathbf{H}(t)$. It can be shown that the error associated with the approximation [**103**]

$$\begin{aligned}\epsilon &= \| \, |\Psi(t+dt)\rangle - |\Psi(t+dt)\rangle_{\text{approx}} \| \\ &< 12\left(\frac{eWdt}{4M}\right)^2 e^{-\frac{(Wdt)^2}{16M}}\,,\end{aligned} \tag{3.9}$$

where $\|\cdots\|$ represents the Euclidean norm, W is the bandwidth of the system and M is the number of Lanczos vectors. It is crucial to get a good estimate of M before the simulations, because M being too small can cause inaccuracy of the simulation, but M being too large would be costly both on memory and on CPU time.

The procedure of a time-dependent ED algorithm reads:

- Estimate the number of Lanczos vectors M needed;
- Use the Lanczos procedure to calculate $\mathbf{V}(t)$ and $\mathbf{T}(t)$ from $\mathbf{H}(t)$;
- Calculate the wavefunction at time step $t+dt$ according to eq. (3.8);
- Perform measurements;
- Go to next time step and repeat steps 2-4, until the maximum time $t_{\max}$ is reached.

CHAPTER 4

Charge Order of Electron-Phonon Coupling in the Honeycomb Lattice

4.1. Introduction

The synthesis of graphene, *i.e.* single layers of carbon atoms in a hexagonal lattice, in 2004, has led to a remarkable body of subsequent work [105, 106]. One of the key elements of interest has been the Dirac dispersion relation of free electrons in this geometry, allowing the exploration of aspects of relativistic quantum mechanics in a conventional solid. "Dirac point engineering" has also become a big theme of investigation of fermions confined in hexagonal optical lattices [107].

It has been natural to ask what the effects of electron-electron interactions are on this unusual noninteracting dispersion relation. Early quantum Monte Carlo (QMC) simulations and series expansion investigations of the Hubbard model on a honeycomb lattice found a critical value of the on-site repulsion $U_c \sim 4t$ for the onset of antiferromagnetic (AF) order at half-filling [28]. This stood in contrast to the extensively studied square lattice geometry for which the perfect Fermi surface nesting and the van Hove singularity of the density of states (DOS) imply $U_c = 0$. Subsequent QMC studies refined this value to $U_c \sim 3.87$ and suggested the possibility that a gapped, spin-liquid (resonating valence bond) phase exists between the weak coupling semimetal and strong coupling AF regimes [29], a conclusion further explored in the strong coupling (Heisenberg) limit [108]. Yet more recent work challenged this scenario, and pointed instead to a conventional, continuous quantum phase transition (QPT) between the semimetal and AF insulator [30, 31, 109]. Equally interesting is the possibility of unusual, topological superconducting phases arising from these spin fluctuations [110, 111, 112, 113, 114, 115, 116, 117, 118, 119].

Graphene itself is, in fact, only moderately correlated. First principles calculations of the on-site Hubbard U yield $U_{00} \sim 9.3$ eV [120], with a nearest neighbor hopping $t \sim 2.8$ eV, so that $U/t \sim 3.3$ is rather close (and slightly below) U_c. Longer range U_{01} interactions can lead

to a rich phase diagram including charge ordered phases [112, 121], especially in the semimetal phase where the Coulomb interaction is unscreened. Charge ordering may also arise when electron-phonon coupling (EPC) is taken into account [122, 123]. Indeed, considering such coupling would allow an exploration of the effect of other sorts of interactions on the Dirac fermions of graphene, complementing the extensive existing literature on electron-electron repulsion.

There are a number of fundamental differences between the two types of correlations. Most significantly, the continuous symmetry of the Hubbard interaction, and the AF order parameter, preclude a finite 2D temperature transition. Therefore the focus is instead on quantum phase transitions. On the other hand, in the Holstein case the charge-density-wave (CDW) order has a one-component order parameter, leading to a transition that breaks a *discrete* symmetry and, consequently, a finite critical temperature (in the Ising universality class). Precise QMC values of T_c on a square lattice were only quite recently obtained [49, 53, 124]. These build on earlier QMC studies of CDW physics in the Holstein model [41, 42], and introduce an exact treatment of fluctuations into earlier mean-field calculations [45].

In this chapter we explore the effect of electron-phonon, rather than electron-electron, interactions, on the properties of Dirac fermions, through QMC simulations of the Holstein model [39] *on a honeycomb lattice.* We use the charge structure factor, compressibility, and Binder ratio to evaluate the critical transition temperatures and EPC, leading to a determination of the phase diagram of the model. Taken together, these results provide considerable initial insight into the nature of the CDW transition for Dirac fermions coupled to phonons.

4.2. Model

The Holstein model [39], as introduced in chapter 1, describes conduction electrons locally coupled to phonon degrees of freedom,

$$\begin{aligned}\hat{\mathcal{H}} = &- t \sum_{\langle \mathbf{i},\mathbf{j}\rangle,\sigma} \left(\hat{d}^{\dagger}_{\mathbf{i}\sigma}\hat{d}_{\mathbf{j}\sigma} + \text{h.c.}\right) - \mu \sum_{\mathbf{i},\sigma} \hat{n}_{\mathbf{i},\sigma} \\ &+ \frac{1}{2}\sum_{\mathbf{i}} \hat{P}^2_{\mathbf{i}} + \frac{\omega_0^2}{2}\sum_{\mathbf{i}} \hat{X}^2_{\mathbf{i}} + \lambda \sum_{\mathbf{i},\sigma} \hat{n}_{\mathbf{i},\sigma}\hat{X}_{\mathbf{i}} \ , \end{aligned} \tag{4.1}$$

where the sums on $\mathbf{i}$ run over a two-dimensional honeycomb lattice (see Fig. 4.1 (a)), with $\langle \mathbf{i}, \mathbf{j} \rangle$ denoting nearest neighbors. $d^{\dagger}_{\mathbf{i}\sigma}$ and $d_{\mathbf{i}\sigma}$ are creation and annihilation operators of electrons with spin σ at a given site $\mathbf{i}$. The first term on the right side of Eq. (4.1) corresponds to the hopping of electrons, with chemical potential μ given by the second term. The phonons are local (dispersionless) quantum harmonic oscillators with frequency ω_0, described in the next two terms of Eq. (4.1). The EPC is included in the final term. The hopping integral ($t = 1$) sets the energy scale, with bandwidth $W = 6\,t$ for the honeycomb geometry.

We use determinant quantum Monte Carlo (DQMC) simulations [**81**], which is introduced in section 2.5, to investigate the properties of Eq. (4.1). Since the fermionic operators appear only quadratically in the Hamiltonian, they can be traced out, leaving an expression for the partition function which is an integral over the space and imaginary time dependent phonon field. The integrand takes the form of the square of the determinant of a matrix M of dimension the spatial lattice size, as well as a "bosonic" action [**125**] arising from the harmonic oscillator terms in Eq. (4.1). The square appears since the traces over the up and down fermions are identical, which leads to a case where the minus sign problem is absent for any electronic filling.

Nevertheless, we focus on the half-filled case, $\langle \hat{n}_{\mathbf{i},\sigma} \rangle = \frac{1}{2}$. This gives us access to the Dirac point where the DOS vanishes linearly. It is also the density for which CDW correlations are most pronounced. It can be shown, using an appropriate particle-hole transformation, that this filling occurs at $\mu = -\lambda^2/\omega_0^2$. We analyze lattices with linear sizes up to $L = 8$ (128 sites). By fixing the discretization mesh to $\Delta\tau = 1/20$, systematic Trotter errors become smaller than the statistical ones from Monte Carlo sampling. To facilitate the discussion, and eventual comparisons with the square lattice case, we introduce a dimensionless EPC: $\lambda_D = \lambda^2/(\omega_0^2\, W)$.

Charge ordering is characterized by the charge-density correlation function,

$$c(\mathbf{r}) = \left\langle \left(n_{\mathbf{i}\uparrow} + n_{\mathbf{i}\downarrow} \right) \left(n_{\mathbf{i}+\mathbf{r}\uparrow} + n_{\mathbf{i}+\mathbf{r}\downarrow} \right) \right\rangle, \tag{4.2}$$

and its Fourier transform, the CDW structure factor,

$$S_{\mathrm{cdw}} = \sum_{\mathbf{r}} (-1)^{\mathbf{r}} c(\mathbf{r})\,, \tag{4.3}$$

The -1 phase accesses the staggered pattern of the charge ordering. The long-range behavior is investigated by performing finite size scaling, and by tracking the evolution of the insulating gap in the CDW phase.

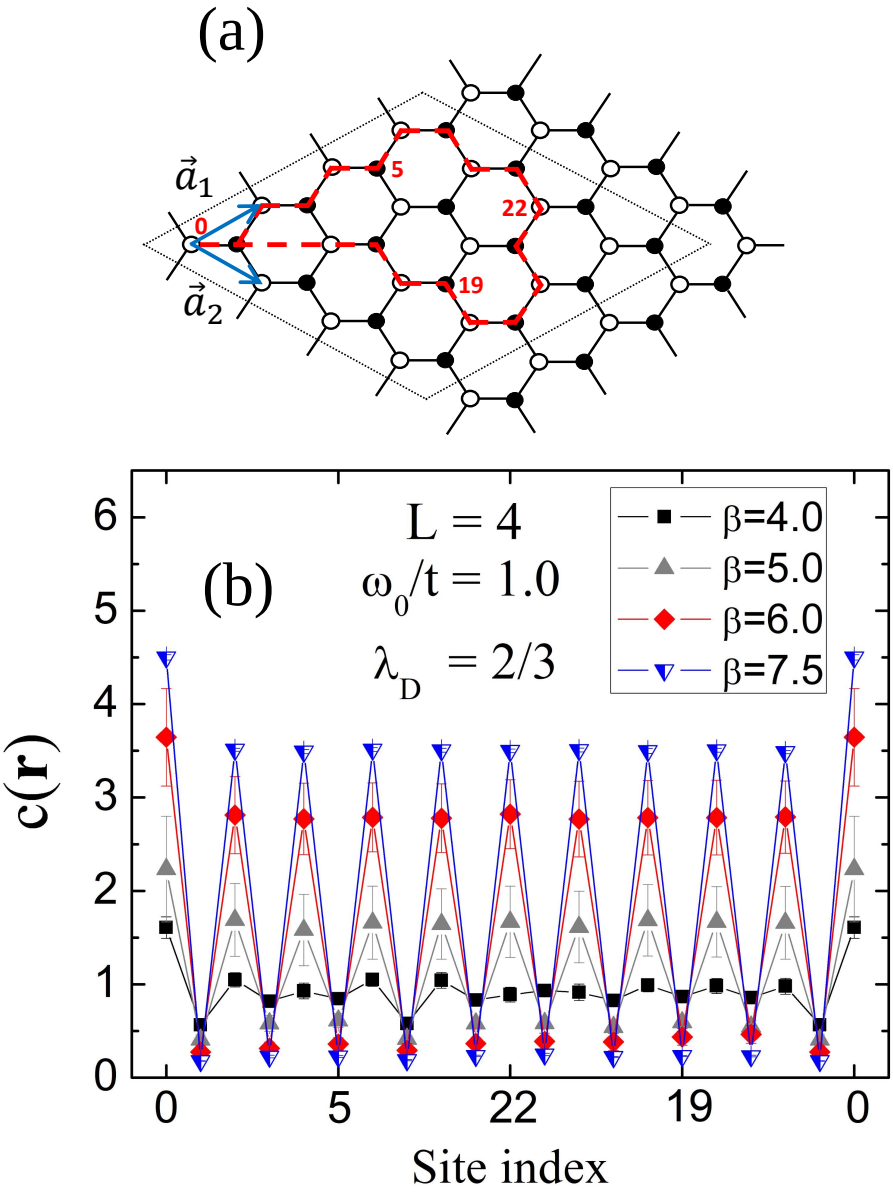

FIGURE 4.1. (a) A 4×4 honeycomb lattice, with the trajectory (red dashed line) corresponding to the horizontal axis of (b), which shows charge correlations $c(\mathbf{r})$ at $\lambda_D = 2/3$, $\omega_0 = 1$, and several temperatures. Here, and in all subsequent figures, when not shown, error bars are smaller than the symbol size.

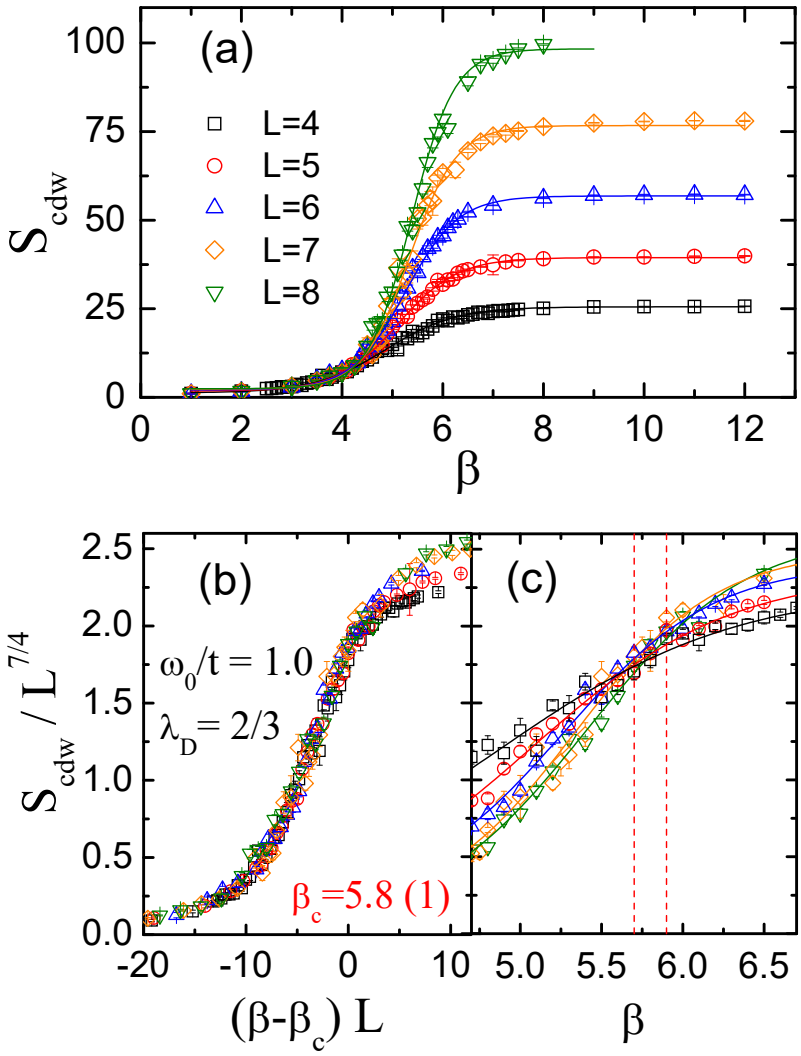

FIGURE 4.2. (a) The charge structure factor as a function of β, for different lattice sizes ($L = 4$-8), and its (b) best data collapse, with the 2D Ising critical exponents, which yields $\beta_c = 5.8$. (c) The crossing plot for $S_{\rm cdw}/L^{\gamma/\nu}$, with vertical dashed lines indicating the uncertainty in the critical temperature. Here $\lambda_D = 2/3$ and $\omega_0 = 1$.

4.3. Existence of CDW phase

We first consider the behavior of charge-density correlations when the temperature $T = \beta^{-1}$ is lowered. Figure 4.1 (b) displays $c(\mathbf{r})$ along the real space path of Fig. 4.1 (a), for $\lambda_D = 2/3$, $\omega_0 = 1$ and several inverse temperatures β. When T is high ($\beta = 4$), we find $c(\mathbf{r}) \approx \rho^2 = 1$, where ρ is the density, indicating an absence of long-range order. However, an enhancement of charge correlations starts to appear at $\beta = 5$, with the emergence of a staggered pattern, which is

even more pronounced at lower T, $\beta = 6$ and 7.5. This temperature evolution of real space charge correlations suggests a transition into a CDW phase.

A more compelling demonstration of long-range ordering (LRO) is provided by Fig. 4.2 (a), which exhibits the structure factor $S_{\rm cdw}$ as a function of β, for different linear sizes L. In the disordered phase at high T, $c(\mathbf{r})$ is short-ranged and, consequently, $S_{\rm cdw}$ is independent of lattice size L. The emergence of a lattice size dependence of $S_{\rm cdw}$, and, ultimately, its saturation at a value not far from $N = 2L^2$, signals the onset temperature of LRO, and a correlation length approaching the lattice size. Figure 4.2 (a) shows that a change between these two behaviors occurs around $\beta \sim 5 - 6$, giving an initial, rough estimate of β_c. The ground state is obtained for $\beta \gtrsim 8$; for larger values, the density correlations no longer change. The precise determination of the critical temperature T_c is accomplished by performing finite size scaling of these data, using the 2D Ising critical exponents $\gamma = 7/4$ and $\nu = 1$, as displayed in Fig. 4.2 (b). The best data collapse occurs at $\beta_c = 5.8\,(1)$, consistent with the crossing of $S_{\rm cdw}/L^{\gamma/\nu}$ presented in Fig. 4.2 (c), and the crossing in the Binder cumulants [**126**]. T_c for the honeycomb lattice is of the same order as that for the square lattice. For the latter at $\omega_0 = 1$, β_c ranges from $\beta_c \sim 16.7$ at $\lambda_D = 0.15$ to $\beta_c \sim 5$ at $\lambda_D = 0.27$ [**49**], and $\beta_c \sim 6.0$ at $\lambda_D = 0.25$ [**2**, **53**].

The Binder Ratio [**126**] provides another means to determining critical points. In Figure 4.3 we show results for

$$B = \frac{\langle\, S_{\rm cdw}^2 \,\rangle}{\langle\, S_{\rm cdw} \,\rangle^2}\,, \tag{4.4}$$

which is the direct analog of the usual $\langle\, M^4 \,\rangle \,/\, \langle\, M^2 \,\rangle^2$ since $S_{\rm cdw}$ is already a density-density correlation (see Eqs. (4.2),(4.3)). B has a crossing in the range $5.8 < \beta_c < 6.2$, a range which overlaps with the critical values inferred from the $S_{\rm cdw}$ scaling collapse (Fig. 4.2(b)) and crossing (Fig. 4.2 (c)) plots.

We note that there is a subtlety in the meaning of the expectation values in Eq. (4.4). Our procedure is to measure $S_{\rm cdw}$ for a given field configuration, via the appropriate Wick contractions of the fermionic operators, and then square that *number*. An alternate, and considerably more complicated procedure would involve the computation of the full Wick contractions of the eight fermion operators in $S_{\rm cdw}^2$. It is believed that the more simple procedure already captures the

essential feature of the Binder procedure [127]. The consistency of our results with the analysis above confirm this understanding.

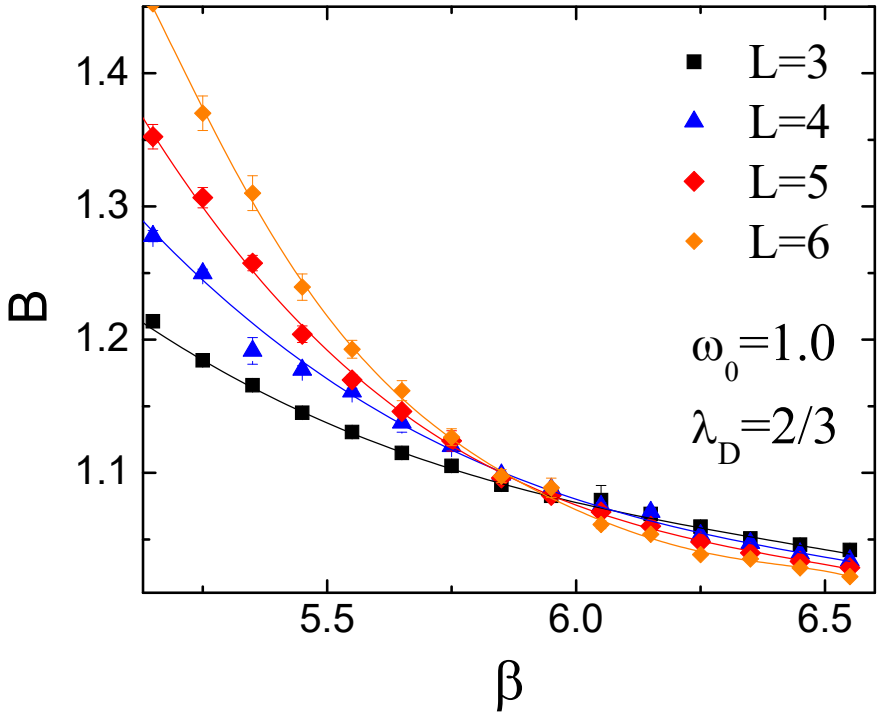

FIGURE 4.3. Binder ratio for $\lambda_D = 2/3$. The curves for different lattice sizes cross at $\beta_c \sim 5.8 - 6.1$, consistent with our estimate of the critical temperature from the finite size scaling of the charge structure factor (Fig. 4.2(b)).

For the range of EPC shown in [49], i.e. $0 \leq \lambda_D \leq 0.3$, β_c steadily decreases with increasing λ_D. A dynamical mean-field theory approach [47, 48] found that there is a minimal β_c (maximum in T_c) for an optimal coupling strength. This non-monotonicity is also present in the repulsive half-filled 3D Hubbard model; the AF β_{Neel} has a minimum at intermediate U. We return to this issue in what follows.

4.4. Finite critical coupling

We investigate next how charge correlations behave as a function of the EPC, and, specifically the possibility that CDW does not occur below a critical interaction strength, as is known to be the case for the Hubbard model on a honeycomb lattice. This is a somewhat challenging question, since at weak coupling one might expect $T_c \sim \omega_0\, e^{-1/\lambda_D}$ becomes small, necessitating a careful

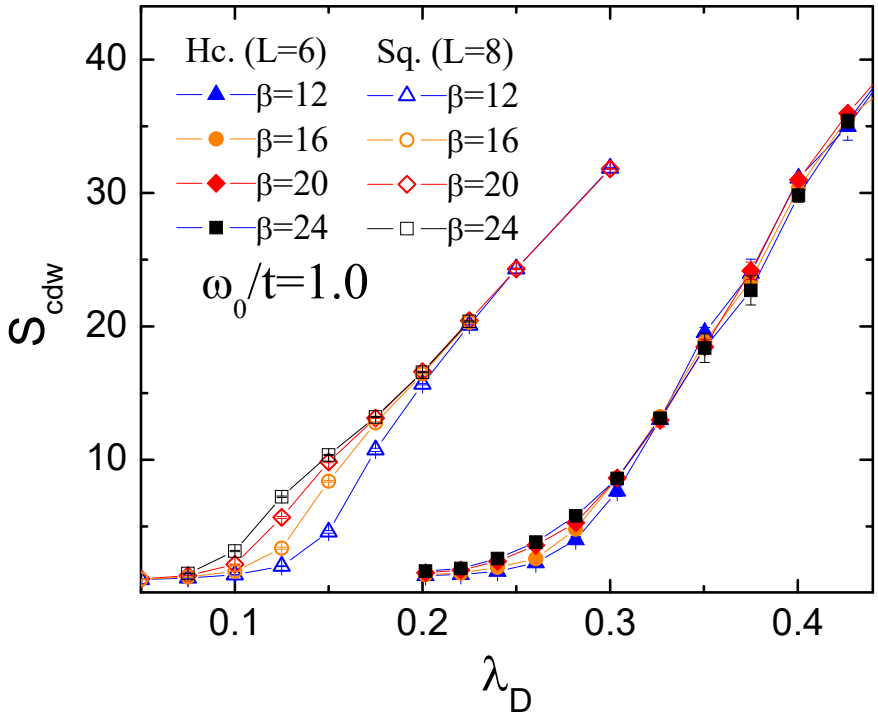

FIGURE 4.4. CDW structure factor $S_{\rm cdw}$ as a function of dimensionless coupling λ_D. $S_{\rm cdw}$ becomes small for $\lambda_D \lesssim 0.25$. For the square lattice, $S_{\rm cdw}$ is large to much smaller values of λ_D. In addition, for the honeycomb (Hc.) lattice $S_{\rm cdw}$ does not change for the two lowest temperatures, whereas $S_{\rm cdw}$ continues to grow at weak coupling for the square (Sq.) lattice.

distinction between the absence of a CDW transition and T_c decreasing below the simulation temperature. Figure 4.4 displays the CDW structure factor as a function of λ_D at different T, on square (open symbols) and honeycomb (filled symbols) lattices, for similar system sizes. The most noticeable feature is that $S_{\rm cdw}$ appears to vanish for weak coupling, $\lambda_D \lesssim 0.25$, strongly suggesting a finite critical EPC for CDW order on the honeycomb lattice. This is a qualitatively reasonable consequence of the vanishing DOS at half-filling, since having a finite DOS is part of the Peierls' requirement for CDW formation [**122**, **123**, **128**].

To ensure this is not a finite T effect, we contrast this behavior of $S_{\rm cdw}$ with that of the square lattice, for which it is believed that a CDW transition occurs at all nonzero λ_D owing to the divergence of the square lattice DOS [**49**]. We note first that $S_{\rm cdw}$ remains large for the square lattice down to values of λ_D a factor of $2-3$ below those of the honeycomb lattice. In addition, there is a distinct difference in the T dependence. In the square lattice case, CDW correlations

are enhanced as T is lowered. The $S_{\rm cdw}$ curves shift systematically to lower λ_D as β increases, consistent with order for all nonzero λ_D. On the other hand, $S_{\rm cdw}$ shows much less T dependence in the honeycomb case, with results from $\beta = 12$ to 20 being almost identical (within error bars).

We do not expect the fermion kinetic energy

$$KE = -t \sum_{\sigma} \langle\, c^{\dagger}_{\mathbf{i}\sigma}\, c_{\mathbf{j}\sigma} + c^{\dagger}_{\mathbf{j}\sigma}\, c_{\mathbf{i}\sigma}\,\rangle\,, \tag{4.5}$$

for near-neighbor sites $\mathbf{i}, \mathbf{j}$, to become zero in the CDW phase, since there are still local quantum fluctuations (hopping). In fact, as pointed out earlier, with only on-site interactions such processes are required for the establishment of a CDW phase. Nevertheless, it should be reduced in magnitude as order is established. Further, even in the absence of order, the fermions will become heavier with larger EPC and they evolve into a dressed 'polaron', also suggesting a reduced magnitude of kinetic energy. This behavior is illustrated in Fig. 4.5 (top). An analogous reduction in the electron kinetic energy is observed with the increase of electron-electron interaction U in the 2D repulsive Hubbard model [**13**].

In a perfect CDW phase at half-filling empty and doubly occupied sites alternate, so that the double occupancy,

$$D = \langle\, n_{\mathbf{i}\uparrow} n_{\mathbf{i}\downarrow}\,\rangle \tag{4.6}$$

goes to $D \to 0.5$. In a completely uncorrelated phase, on other hand, $D \to \langle n_{\mathbf{i}\uparrow}\rangle \langle n_{\mathbf{i}\downarrow}\rangle$ so that $D \to 0.25$ at half-filling. The evolution of D with λ_D is given in Fig. 4.5 (bottom) and properly exhibits these two limits.

The most rapid evolution of both $|KE|$ and D in Fig. 4.5 occurs at $\lambda_D \sim 0.34 - 0.35$. This is the same as the value for which $S_{\rm cdw}$ changes most quickly in Fig. 4.4. These quantities appear to become largely independent of λ_D below the critical value where CDW order no longer occurs.

Further insight into the existence of a critical EPC is provided by CDW gap, inferred from the plateau in $\rho(\mu)$ via $\Delta_c \equiv \mu(\rho = 1 + x) - \mu(\rho = 1 - x)$. Here we choose $x = 0.01$; other values of x give qualitatively similar results. Figure 4.6 (a) displays Δ_c for different λ_D and fixed $\beta = 10$ and 16. The gap has a non-monotonic dependence on the EPC, with a maximum at $\lambda_D \approx 0.43$. For smaller EPCs the CDW gap is strongly suppressed. A crossing of the curves occurs at $\lambda_D \sim 0.27$

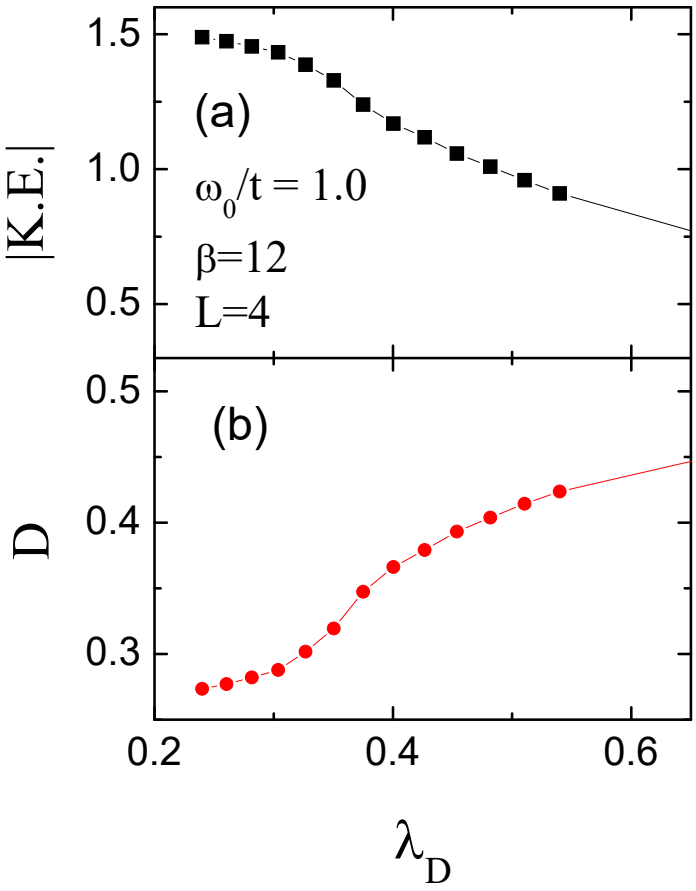

FIGURE 4.5. (a) The electron kinetic energy and (b) double occupancy as a functions of λ_D for an $L = 4$ honeycomb lattice at $\beta = 12$ and $\omega_0 = 1$.

so that Δ_c *decreases* as T is lowered for $\lambda_D \lesssim 0.27$, consistent with a critical EPC. The full plateau in $\rho(\tilde{\mu})$, for different λ_D and fixed $\beta = 10$ can be seen in Fig. 4.7. The compressibility $\kappa = \partial\rho/\partial\mu$ is presented as a function of λ_D in Fig. 4.6 (b) for honeycomb and square lattices at several T. We have normalized by the noninteracting value κ_0 (evaluated in the thermodynamics limit) to provide a comparison that eliminates trivial effects of the DOS. For the honeycomb lattice, κ/κ_0 shows a sharp increase around $\lambda_D \sim 0.27 \pm 0.01$, consistent with the vanishing of $S_{\rm cdw}$ in Fig. 4.4. Furthermore, κ/κ_0 grows with β. For the square lattice, κ/κ_0 vanishes down to much smaller λ_D, behaves more smoothly at the lowest T, and is an order of magnitude smaller. Its small residual value is a consequence of the exponentially divergence of the CDW ordering temperature as $\lambda_D \to 0$.

Finally, we have obtained T_c for a range of λ_D above the critical EPC, yielding the phase diagram in Fig. 4.8. T_c decreases rapidly at $\lambda_D \approx 0.28$. The inset shows the crossing of the

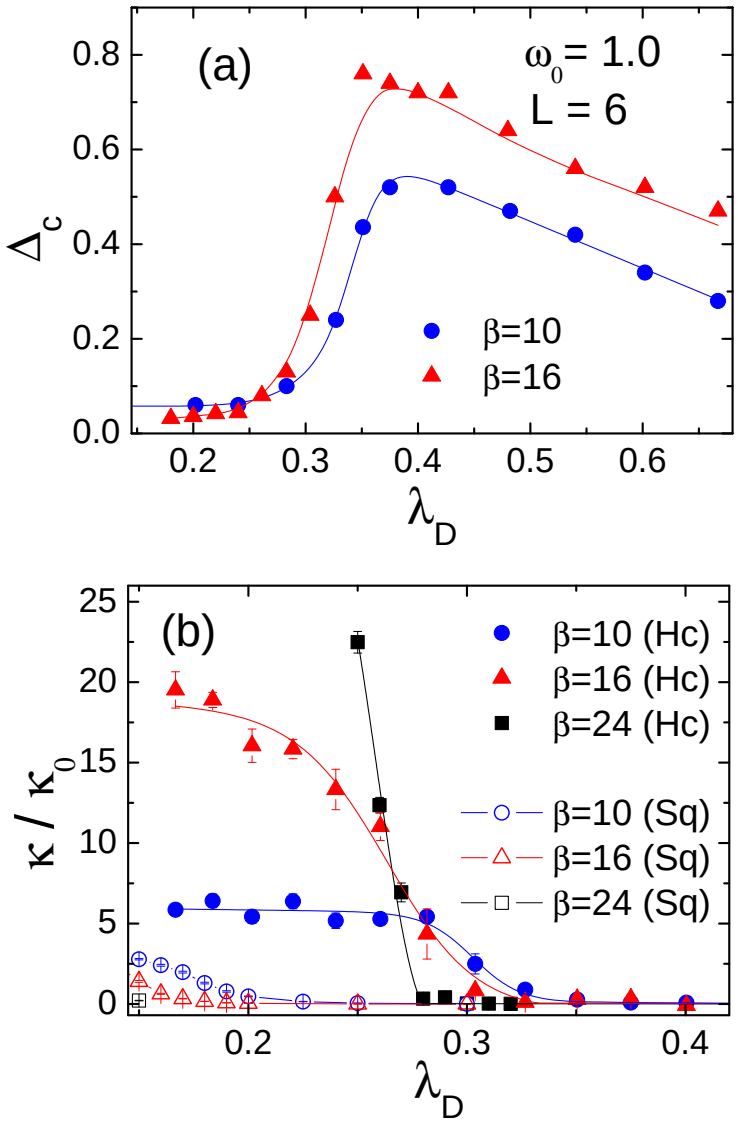

FIGURE 4.6. (a) The charge gap Δ_c (see text) as a function of λ_D. (b) The electronic compressibility κ as a function of λ_D for square (open symbols) and honeycomb (filled symbols) lattices with linear sizes $L = 8$ and 6, respectively.

invariant correlation ratio R_c, a quantity which is independent of lattice size at a quantum critical point (QCP) [126]. The invariant correlation length R_c,

$$R_c \equiv 1 - \frac{S(\mathbf{Q} + \delta\mathbf{q})}{S(\mathbf{Q})} \tag{4.7}$$

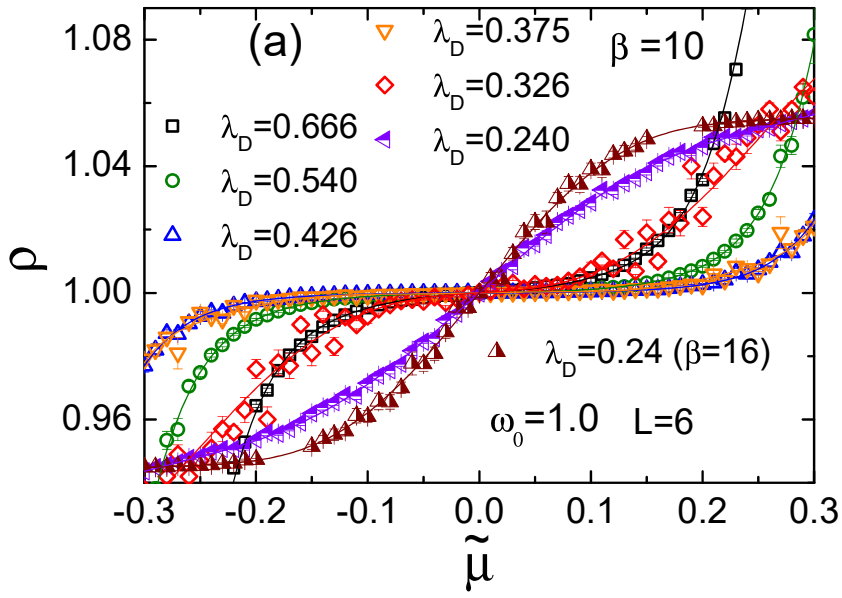

FIGURE 4.7. The electronic density as a function of the chemical potential for several couplings strengths. We have shifted the chemical potential so that half-filling occurs at $\tilde{\mu} = \mu - \lambda^2/\omega_0^2 = 0$ for all curves.

measures the fall off of the charge structure factor as $\mathbf{q}$ is shifted away from its CDW value at wavevector $\mathbf{Q}$, as shown in Eq. (4.3). R_c is advantageous to consider as it has, similar to the 'Binder ratio', more benign scaling corrections than does the charge structure factor itself [**126**]. T_c exhibits a maximum at $\lambda_D \sim 0.4$-0.5, which lies close to the coupling for which Δ_{cdw} is greatest (Fig. 4.6). The maximum in T_c reflects a competition between a growth with λ_D as it induces CDW order with a reduction as the EPC renormalizes the single electron mass, yielding a heavy polaron [**46**,**62**,**63**,**65**,**67**,**129**,**130**,**131**]. Unlike CDW order which arises directly from intersite interactions, in the Holstein model it is produced by a second order process: the lowering of the kinetic energy by virtual hopping between doubly occupied and empty sites. A mass renormalization-driven reduction in this hopping lowers T_c.

4.5. Conclusions

In this chapter we have presented DQMC simulations of the Holstein model on a honeycomb lattice. The existence of long-range charge order was established below a finite critical transition temperature in the range $T \sim t/6$, for sufficiently large EPC. T_c is similar for the square and

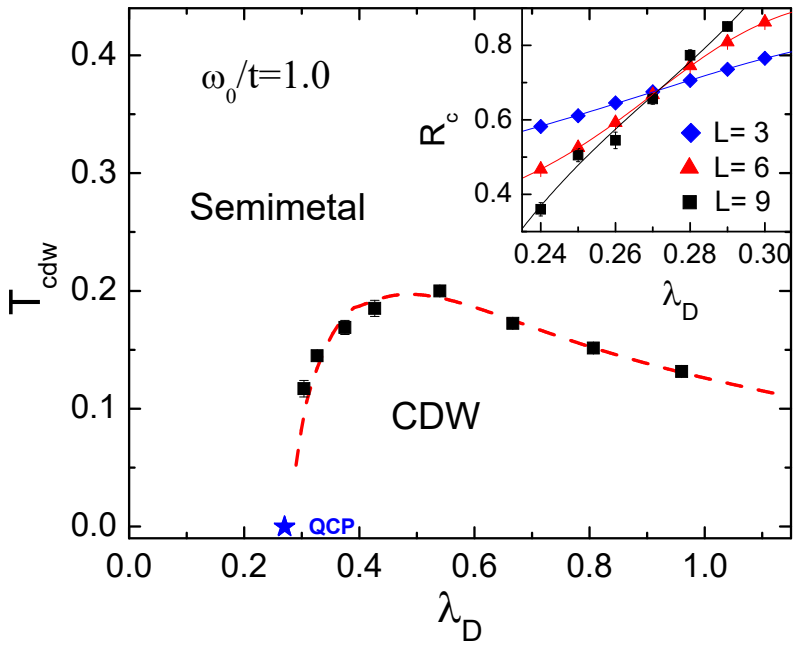

FIGURE 4.8. Critical temperature for the CDW transition in the honeycomb Holstein model inferred from finite size scaling analysis in Fig. 3.2. The inset shows the crossing of the invariant correlation ratio R_c (see text), resulting in the indicated QCP, in good agreement with the value at which an extrapolated T_c would vanish.

honeycomb lattices, despite the dramatic differences in their noninteracting densities of states: diverging in the former case, and vanishing in the latter.

Our data suggest that, as for the honeycomb Hubbard model, [28, 29, 30, 31, 108, 109], the vanishing non-interacting density of states of Dirac fermions gives rise to a minimal value for $\lambda_D \sim (0.27 \pm 0.01)\, t$, only above which does LRO occur. Thus although the critical CDW transition temperatures for the two geometries are similar *when order occurs*, the Dirac density of states does fundamentally alter the phase diagram by introducing a weak coupling regime in which order is absent. The 1D Holstein model is also known to have a metallic phase for electron-phonon couplings below a critical value [50, 132].

This initial study has focused on a simplified model. The phonon spectra of graphene and graphitic materials have been extensively explored [133] and, of course, are vastly more complex than the optical phonon mode incorporated in the Holstein Hamiltonian. However, as has been recently emphasized [53], including realistic phonon dispersion relations is relatively straightforward

in QMC simulations, since the associated modifications affect only the local bosonic portion of the action, and not the computationally challenging fermionic determinants. One important next step will be the study of more complex phonon modes, and the types of electronic order and phase transitions that they induce. Such investigations open the door to examining hexagonal CDW materials like the transition metal dichalcogenides [**134**, **135**, **136**, **137**]. However, their layered structures add considerable challenges to descriptions with simple models.

CHAPTER 5

Charge Density Wave in the π-flux Lattice

5.1. Introduction

The physics of massless Dirac points, as exhibited in the band structure of the honeycomb lattice of graphene, has driven intense study [138, 139, 140, 141]. The square lattice with π-flux per plaquette is an alternate tight-binding Hamiltonian which also contains Dirac points in its band structure. Initial investigations of the π-flux model focused on the non-interacting limit [142], but, as with the honeycomb lattice, considerable subsequent effort has gone into extending this understanding to incorporate the effect of electron-electron interactions. Numerical simulations of the Hubbard Hamiltonian with an on-site repulsion U between spin up and spin down fermions, including Exact Diagonalization [143] and Quantum Monte Carlo (QMC) [99, 109, 144, 145, 146, 147, 148, 149] revealed a quantum phase transition at $U_c \sim 5.55\,t$ into a Mott antiferromagnetic (AF) phase in the chiral Heisenberg Gross-Neveu universality class. For a spinless fermion system with near-neighbor interactions a chiral Ising Gross-Neveu universality class is suggested [150]. These results have been contrasted with those on a honeycomb lattice, which has a similar Dirac point structure, though at a smaller critical interaction $U_c \sim 3.85\,t$ [109].

In the case of the repulsive Hubbard Hamiltonian, there were two motivations for studying both the honeycomb and the π-flux geometries. The first was to verify that the quantum critical transitions to AF order as the on-site repulsion U increases share the same universality class, that of the Gross-Neveu model. The second was to confirm that an intermediate spin-liquid (SL) phase between the semi-metal and AF phases [29], which had been shown not to be present on a honeycomb lattice [151], was also absent on the π-flux geometry.

Studies of the SU(2) π-flux Hubbard model have also been extended to SU(4), using projector QMC [152], and to staggered flux where $\pm\pi$ hopping phases alternate on the lattice [153]. In the former case, the semi-metal to AF order transition was shown to be replaced by a semi-metal to

valence bond solid transition characterized by breaking of a $\mathcal{Z}_4$ symmetry. In the latter work, an intermediate phase with power-law decaying spin-spin correlations was suggested to exist between the semi-metal and AF.

A largely open question is how this physics is affected in the presence of electron-phonon rather than electron-electron interactions. A fundamental Hamiltonian, proposed by Holstein [39], includes an on-site coupling of electron density to the linear displacement of the phonon field. In the low density limit, extensive numerical work has quantified polaron and bipolaron formation, in which electrons are "dressed' by an accompanying lattice distortion [46, 62, 64, 65, 66, 68, 129, 130]. At sufficiently large coupling, electrons or pairs of electrons can become 'self-trapped' (localized). One of the most essential features of the Holstein model is that the lattice distortion of one electron creates an energetically favorable landscape for other electrons, so that there is an effective attraction mediated by the phonons. At higher densities, collective phenomena such as Charge-Density Wave (CDW) phases, and superconductivity (SC) have been widely studied [41, 42, 43, 44, 45, 47, 130, 132, 154]. CDW is especially favored on bipartite lattices and at fillings which correspond to double occupation of one of the two sublattices. SC tends to occur when one dopes away from these commensurate fillings.

Recent work on the Holstein model on the honeycomb lattice suggested a quantum phase transition from semi-metal to gapped CDW order [3, 56] similar to the results for the Hubbard Hamiltonian. However, a key difference between the Hubbard and Holstein models is the absence of the SU(2) symmetry of the order parameter in the latter case. Thus, while long-range AF order arising from electron-electron interaction occurs only at zero temperature in 2D, the CDW phase transition induced by electron-phonon coupling can occur at finite temperature- the symmetry being broken is that associated with two *discrete* sub-lattices. For classical phonons ($\omega_0 = 0$), the electron-phonon coupling becomes an on-site energy in the mean-field approximation. In the anti-adiabatic limit where phonon frequencies are set to infinity, the Holstein model maps onto the attractive Hubbard model.

Here we extend the existing work on the effect of EPC on Dirac fermions from the honeycomb geometry to the π-flux lattice. The π-flux state is realized by threading half of a magnetic flux

quantum through each plaquette of a square lattice [155]. Recently it has been experimentally realized in optical lattices using Raman assisted hopping [156]. There are also theoretical suggestions that the π-flux lattice might be engineered by the proximity of an Abrikosov lattice of vortices of a type-II superconductor, or via spontaneously generating a π-flux by coupling fermions to a $\mathcal{Z}_2$ gauge theory in (2+1) dimensions [157]. The π-flux hopping configuration has an additional interesting feature motivating our current work: it is the unique magnetic field value which minimizes the ground state energy for non-interacting fermions at half-filled on a bipartite lattice. Indeed, Lieb has shown that this theorem is also true at finite temperature, and furthermore holds in the presence of Hubbard inteactions [158]. Here we consider the thermodynamics of the π-flux lattice with EPC.

5.2. Model

The Holstein model [39] describes conduction electrons locally coupled to phonon degrees of freedom,

$$\hat{\mathcal{H}} = -\sum_{\langle \mathbf{i},\mathbf{j}\rangle,\sigma} \left(t_{\mathbf{i},\mathbf{j}}\, \hat{d}^{\dagger}_{\mathbf{i}\sigma}\hat{d}_{\mathbf{j}\sigma} + \text{h.c.}\right) - \mu \sum_{\mathbf{i},\sigma} \hat{n}_{\mathbf{i},\sigma} + \frac{1}{2M}\sum_{\mathbf{i}} \hat{P}^2_{\mathbf{i}} + \frac{\omega_0^2}{2}\sum_{\mathbf{i}} \hat{X}^2_{\mathbf{i}} + \lambda \sum_{\mathbf{i},\sigma} \hat{n}_{\mathbf{i},\sigma}\hat{X}_{\mathbf{i}} \ . \tag{5.1}$$

Same as described in previous chapter, the sums on $\mathbf{i}$ and σ run over all lattice sites and spins $\sigma = \uparrow, \downarrow$. $\langle \mathbf{i}, \mathbf{j}\rangle$ denotes nearest neighbors. $\hat{d}^{\dagger}_{\mathbf{i}\sigma}$ and $\hat{d}_{\mathbf{i}\sigma}$ are creation and annihilation operators of electrons with spin σ on a given site $\mathbf{i}$; $\hat{n}_{\mathbf{i},\sigma} = \hat{d}^{\dagger}_{\mathbf{i}\sigma}\hat{d}_{\mathbf{i}\sigma}$ is the number operator. The first term of Eq. (1) corresponds to the hopping of electrons $\mathcal{K}_{\text{el}}$, with chemical potential μ. The next line of the Hamiltonian describes optical phonons, local quantum harmonic oscillators of frequency ω_0 and phonon position and momentum operators, $\hat{X}_{\mathbf{i}}$ and $\hat{P}_{\mathbf{i}}$ respectively. The phonons are dispersionless since there are no terms connecting $\hat{X}_{\mathbf{i}}$ on different sites of the lattice. The phonon mass M is set to unity. The electron-phonon coupling is included in the last term. We set hopping $|t_{\mathbf{i},\mathbf{j}}| = t = 1$ as the energy scale and focus on half-filling, ($\langle \hat{n}\rangle = 1$), which can be achieved by setting $\mu = -\lambda^2/\omega_0^2$. It is useful to present results in terms of the dimensionless coupling $\lambda_D = \lambda^2/(\omega_0^2 W)$ which represents

the ratio of the effective electron-electron interaction obtained after integrating out the phonon degrees of freedom, and W is the kinetic energy bandwidth.

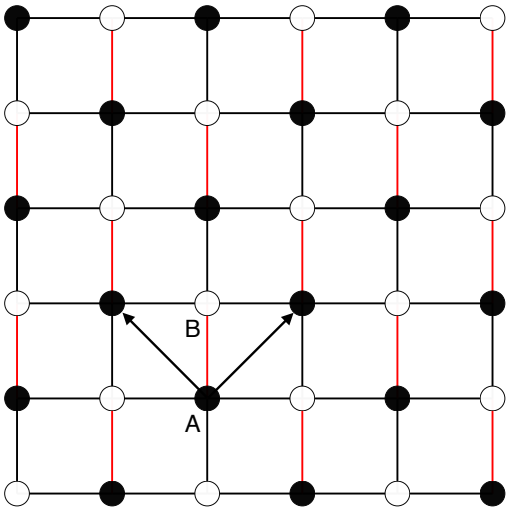

FIGURE 5.1. π-flux phase on a 6×6 square lattice. Sublattices A and B are shown by solid and open circles. Bonds in red correspond to hopping $t' = -t$, as opposite to black lines with hopping t. Arrows represent the basis vectors.

The two dimensional π-flux phase on a square lattice is schematically shown in Fig. 5.1. All hopping in the x direction are t, while half of the hoppings along the y-direction are set to $t' = t\, e^{i\pi} = -t$, where the phase π in the hopping amplitude arises from the Peierls prescription for the vector potential of the magnetic field. As a consequence, an electron hopping on a contour around each plaquette picks up a total phase π, corresponding to one half of a magnetic flux quantum $\Phi_0 = hc/e$ per plaquette. The lattice is bipartite, with two sublattices A and B. Each unit cell consists of two sites. In reciprocal space, with the reduced Brillouin zone ($|k_x| \leq \pi, |k_y| \leq |k_x|$), the non-interacting part of Hamiltonian Eq.(1) can be written as,

$$\hat{\mathcal{H}}_0 = \sum_{\mathbf{k}\sigma} \hat{\psi}^{\dagger}_{\mathbf{k}\sigma} \mathbf{H}_0(\mathbf{k}) \hat{\psi}_{\mathbf{k}\sigma}, \tag{5.2}$$

where

$$\hat{\psi}_{\mathbf{k}\sigma} = \begin{pmatrix} \hat{d}_{A\sigma} & \hat{d}_{B\sigma} \end{pmatrix}^T, \tag{5.3}$$

and the noninteracting Hamiltonian matrix

$$\mathbf{H}_0(\mathbf{k}) = \begin{pmatrix} 0 & 2\,t\cos k_x + 2\,i\,t\sin k_y \\ 2\,t\cos k_x - 2\,i\,t\sin k_y & 0 \end{pmatrix}. \tag{5.4}$$

The energy spectrum $E_{\mathbf{k}} = \pm 2\,t\sqrt{\cos^2 k_x + \sin^2 k_y}$ describes a semi-metal with two inequivalent Dirac points at $\mathbf{K}_\pm = (\pm\pi/2, 0)$, shown in Fig. 5.2. In the low-energy regime of the dispersion, the density of states (DOS) vanishes linearly near the Dirac point where $E_{\mathbf{k}} = 0$, as shown in Fig. 5.3. The bandwidth of the π-flux phase is $W = 4\sqrt{2}\,t$. In Fig. 5.3 the DOS of the honeycomb lattice is shown for comparison. The Dirac Fermi velocity is $v_{\mathrm{F}} = 2t$ $(1.5t)$ for the π-flux (honeycomb) lattice. Near the Dirac point, the DOS $\rho(\omega) \sim |\omega|/v_{\mathrm{F}}$, and the π-flux model has a smaller slope.

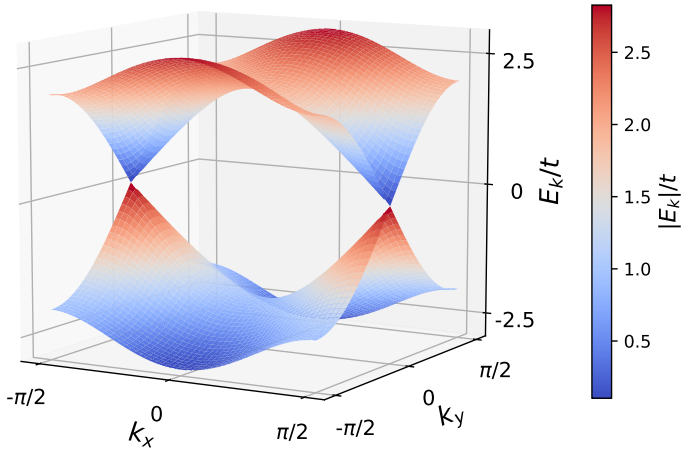

FIGURE 5.2. The dispersion relation $E_{\mathbf{k}}$ for π-flux phase on a square lattice. There are two Dirac points at $(k_x, k_y) = (\pm\pi/2, 0)$. The bandwidth for the π-flux model is $W = 4\sqrt{2}\,t$.

5.3. Mean-Field Theory results

In this section, we present a mean-field theory approach to solve the Holstein model. Semi-metal to superfluid transitions have previously been investigated with MFT in 2D and 3D [159,160]. Here we focus on the semi-metal to CDW transition. In the mean-field approximation, the phonon displacement at site $\mathbf{i}$ is replaced by its average value, modulated by a term which has opposite

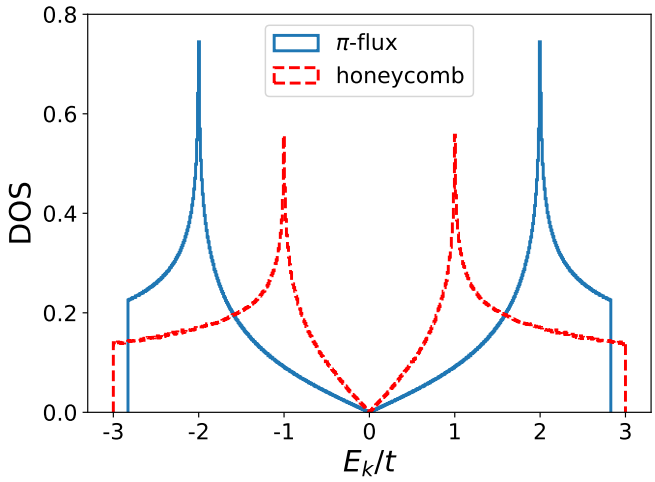

FIGURE 5.3. The density of states for the π-flux phase square lattice and the honeycomb lattice. The bandwidths are nearly identical, but the honeycomb lattice has a substantially larger slope of the linear increase of the DOS.

sign on the two sublattices,

$$\langle X_{\mathbf{i}} \rangle = X_0 \pm X_{\mathrm{mf}} \, (-1)^{\mathbf{i}} \, . \tag{5.5}$$

Here $X_0 = -\lambda/\omega_0^2$ is the "equilibrium position" at half-filling and X_{mf} is the mean-field order parameter. When $X_{\mathrm{mf}} = 0$, phonons on all sites have the same average displacement, indicating the system remains in semi-metal phase, whereas when $X_{\mathrm{mf}} \neq 0$, the last term in the Hamiltonian Eq. (1), i.e., $\lambda \sum_{\mathbf{i},\sigma} \hat{n}_{\mathbf{i},\sigma} \hat{X}_{\mathbf{i}}$, becomes an on-site staggered potential, which corresponds to the CDW phase. The phonon kinetic energy term is zero as a result of the static field. The resulting static mean-field Hamiltonian is quadratic in the fermion operators. Diagonalizing gives energy eigenvalues $\epsilon_n(X_{\mathrm{mf}})$. The free energy F can then be directly obtained by,

$$F(\beta, X_{\mathrm{mf}}) = -\frac{1}{\beta} \sum_n \ln(1 + e^{-\beta \epsilon_n}) + \frac{N\omega_0^2}{2}(X_0^2 + X_{\mathrm{mf}}^2), \tag{5.6}$$

Minimizing the free energy with respect to X_{mf} (or equivalently, a self-consistent calculation) will determine the order parameter. X_{mf} is found to be zero at high temperatures: the energy cost of the second term in Eq. 5.6 exceeds the energy decrease in the first term associated with opening of a gap in the spectrum ϵ_n. X_{mf} becomes nonzero below a critical temperature T_c.

T_c for the π-flux lattice is shown in Fig. 5.4, along with the result of analogous MFT calculations for the honeycomb and (zero flux) square geometries. The lattice size L = 180 is chosen for all three models. This is sufficiently large so that finite size effects are smaller than the statistical sampling error bars. At zero temperature, the CDW order exhibits a critical EPC for the π-flux and the honeycomb lattices. This QCP arises from the Dirac fermion dispersion, which has a vanishing DOS at the Fermi energy. The honeycomb lattice QCP has a smaller critical value. However, when measured in units of the Fermi velocity, the ratios $\lambda_{D,\mathrm{crit}}/v_\mathrm{F} = 0.13$ and 0.14 are quite close for the honeycomb and π-flux geometries respectively. We will see this is also the case for the exact DQMC calculations. For the square lattice, on the other hand, the DOS has a van Hove singularity at the Fermi energy, and the CDW develops at arbitrarily small coupling strength.

Another feature of the MFT phase diagram is that, as the coupling increases, T_c increases monotonically. This is in contrast to the exact DQMC results, where T_c decreases at large coupling strengths (Fig. 5.13). A similar failure of MFT is well known for the Hubbard Hamiltonian where the formation of AF ordering is related to two factors: the local moment $m_z^2 = (n_\uparrow - n_\downarrow)^2 = 1 - 2\langle n_\uparrow n_\downarrow \rangle$ and the exchange coupling $J = 4t^2/U$. The double occupancy $\langle n_\uparrow n_\downarrow \rangle$ is suppressed by the interaction, resulting in the growth of the local moment. Thus upon cooling, the Hubbard model has two characteristic temperatures: the temperature of local moment formation, which increases monotonically with U, and further the AF ordering scale, which falls as J. Since the interaction is simply decoupled locally and the exchange coupling is not addressed, within MFT the formation of the local moments, and their ordering, occur simultaneously. MFT thus predicts a monotonically increasing T_c with U.

5.4. DQMC results

Again we use the DQMC method to approach this problem.

5.4.1. Double occupancy and kinetic energy. We first show data for several local observables, the electron kinetic energy $|\mathcal{K}_\mathrm{el}| = |\sum_{\langle \mathbf{i},\mathbf{j}\rangle,\sigma} \left(t_{\mathbf{i},\mathbf{j}}\, \hat{d}^\dagger_{\mathbf{i}\sigma} \hat{d}_{\mathbf{j}\sigma} + \mathrm{h.c.}\right)|$ and double occupancy $\mathcal{D} = \langle\, n_{\mathbf{i}\uparrow} n_{\mathbf{i}\downarrow}\,\rangle$. For a tight-binding model on a bipartite lattice at half-filling, Lieb has shown that the energy-minimizing magnetic flux is π per plaquette, both in for noninteracting fermions and

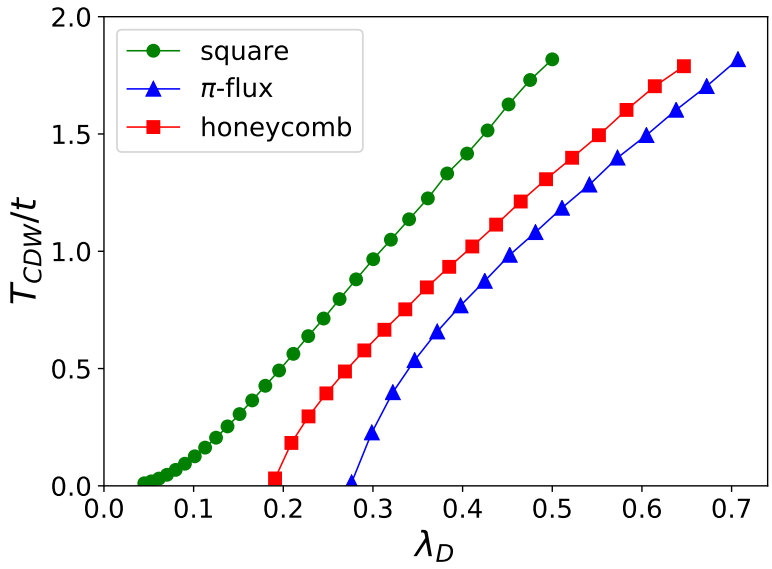

FIGURE 5.4. MFT T_c for CDW phase transition as a function of dimensionless coupling λ_D for the square lattice with no magnetic flux, the π-flux phase square lattice, and the honeycomb lattice. For the geometries with a Dirac spectrum MFT captures the existence for a QCP, a critical value of λ_D below which there is no CDW order even at $T = 0$, and the absence of a QCP for the conventional square lattice.

in the presence of a Hubbard U [158]. Here we show $|\mathcal{K}_{\rm el}|$ for the Holstein model, a case not hitherto considered.

Figure 5.5 shows $|\mathcal{K}_{\rm el}|$ (left panel) and $\mathcal{D}$ (right panel) as functions of the dimensionless EPC λ_D for $\beta = 6/t, 8/t, 10/t$. There is little temperature dependence for these local quantities. The magnitude of the kinetic energy $|\mathcal{K}_{\rm el}|$ decreases as λ_D grows, reflecting the gradual localization of the dressed electrons ("polarons").

At the same time, the double occupancy $\mathcal{D}$ evolves from its noninteracting value $\mathcal{D} = \langle n_{\mathbf{i}\uparrow} n_{\mathbf{i}\downarrow} \rangle = \langle n_{\mathbf{i}\uparrow} \rangle \langle n_{\mathbf{i}\downarrow} \rangle = 1/4$ at half-filling, to $\mathcal{D} = 1/2$ at large λ_D. In the strong coupling regime, we expect robust pair formation, so that half of the lattice sites will be empty and half will be doubly occupied.

The evolutions of $\mathcal{D}$ and $|\mathcal{K}_{\rm el}|$ have largest slope at $\lambda_D \sim 0.42$ which, as will be seen, coincides with the location of the QCP between the semi-metal and CDW phases.

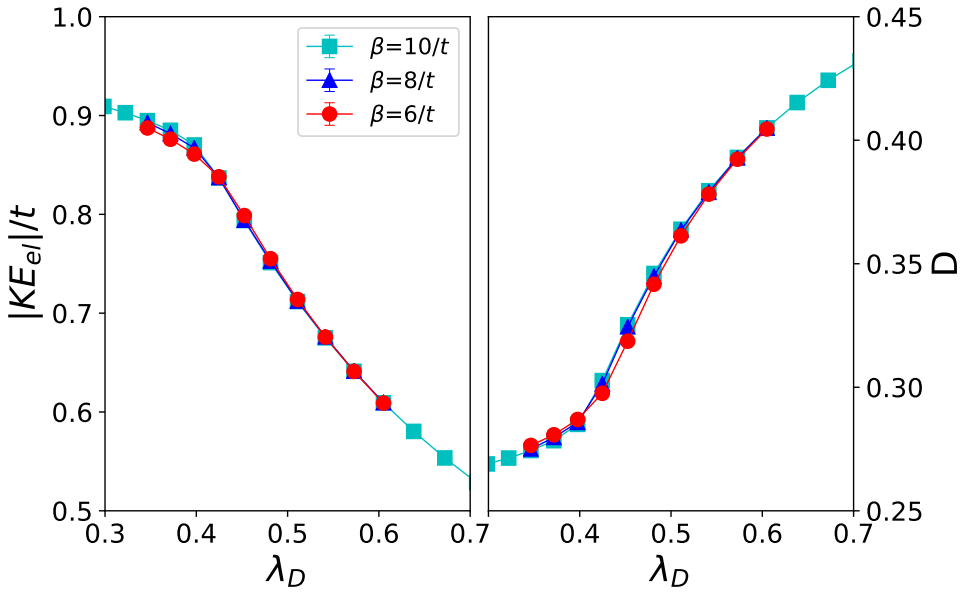

FIGURE 5.5. Left: The magnitude of electron kinetic energy $|\mathcal{K}_{\rm el}|$ as a function of EPC strength λ_D. Simulations are performed on a L = 10 lattice at inverse temperatures $\beta = 6/t, 8/t, 10/t$ and fixed $\omega_0 = 1.0\,t$. Right: Double occupancy D as a function of EPC strength λ_D.

5.4.2. Existence of long-range CDW order. The structure factor $S(\mathbf{Q})$ is the Fourier transform of the real-space spin-spin correlation function $c(\mathbf{r})$,

$$S(\mathbf{Q}) = \sum_{\mathbf{r}} e^{i\mathbf{Q}\cdot\mathbf{r}} c(\mathbf{r}),$$
$$c(\mathbf{r}) = \left\langle \left(n_{\mathbf{i}\uparrow} + n_{\mathbf{i}\downarrow} \right) \left(n_{\mathbf{i}+\mathbf{r}\uparrow} + n_{\mathbf{i}+\mathbf{r}\downarrow} \right) \right\rangle, \tag{5.7}$$

and characterizes the charge ordering. In a disordered phase $c(\mathbf{r})$ is short-ranged and $S(\mathbf{Q})$ is independent of lattice size. In an ordered phase, $c(\mathbf{r})$ remains large out to long distances, and the structure factor will be proportional to the number of sites, at the appropriate ordering wave vector $\mathbf{Q}$. At half-filling $S(\mathbf{Q})$ is largest at $\mathbf{Q} = (\pi, \pi)$. We define $S_{\rm cdw} \equiv S(\pi, \pi)$. Figure 5.6 displays $S_{\rm cdw}$ as a function of inverse temperature β at different phonon frequencies ω_0 and coupling strengths λ_D. The linear lattice size $L = 6$. At fixed ω_0 and strong coupling, $S_{\rm cdw}$ grows as temperature is lowered, and saturates to $S_{\rm cdw} \sim$ N, indicating the development of long-range order (LRO), i.e. the phase transition into CDW phase. Note that $\beta = 10/t$ is always in the plateau region,

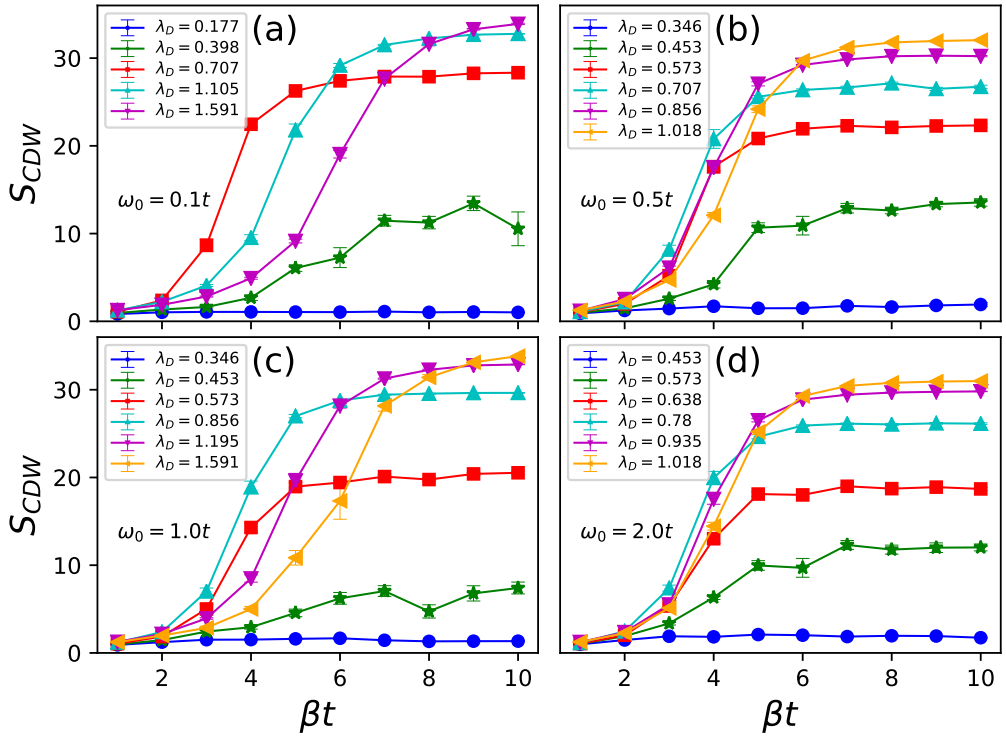

FIGURE 5.6. The CDW structure factor of the π-flux phase Holstein model as a function of inverse temperature β. The phonon frequencies ω_0 are (a), $0.1\,t$; (b), $0.5\,t$; (c), $1.0\,t$; (d), $2.0\,t$ in the four panels. The lattice size $L = 6$.

suggesting the correlation length has become larger than the lattice size, and the ground state has been reached. In the following, we use $\beta = 10/t$ to represent the properties at $T \to 0$.

However, as λ_D is decreased sufficiently, $S_{\rm cdw}$ eventually shows no signal of LRO even at large β, providing an indication that there is a QCP, with CDW order only occurring above a finite λ_D value. Figure 5.6 also suggests that the critical temperature T_c is non-monotonic with increasing λ_D. The values of β at which $S_{\rm cdw}$ grows first shift downward, but then become larger again. This non-monotonicity agrees with previous studies of Dirac fermions on the honeycomb lattice [3, 56]. We can estimate the maximum T_c to occur at $\lambda_D \approx 0.71, 0.71, 0.86$ and 0.78 for $\omega_0 = 0.1\,t, 0.5\,t, 1.0\,t, 2.0\,t$ respectively. In the anti-adiabatic limit $\omega_0 \to \infty$, the Holstein model maps onto the attractive Hubbard model, and $T_c = 0$ owing to the degeneracy of CDW and superconducting correlations [154]. (The order parameter has a continuous symmetry.) A recent

study [57] has shown that $\omega_0 \gtrsim 10^2\, t$ is required to achieve the $-U$ Hubbard model limit, a surprisingly large value.

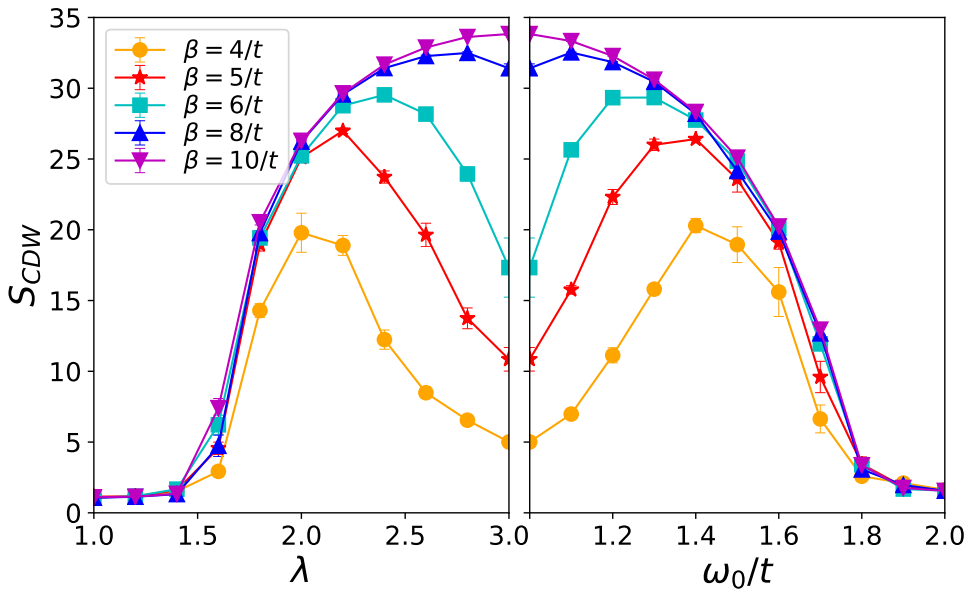

FIGURE 5.7. $S_{\rm cdw}$ (a) as a function of λ at fixed $\omega_0 = 1.0\,t$; and (b) as a function of ω_0 at fixed λ=3.0, at different inverse temperatures β. Lattice size $L = 6$ is used in this figure.

Figure 5.7(a) shows $S_{\rm cdw}$ as a function of λ at fixed $\omega_0 = 1.0\,t$. At the highest temperature shown, $\beta = 4/t$, $S_{\rm cdw}$ reaches maximum at intermediate coupling $\lambda \sim 2.0$, then decreases as λ gets larger. The region for which $S_{\rm cdw}$ is large is a measure of the range of λ for which the CDW ordering temperature T_c exceeds β^{-1}. As β increases, this range is enlarged. Figure 5.7(b) is an analogous plot of $S_{\rm cdw}$ as a function of ω_0 at fixed $\lambda = 3.0$. The two plots appear as mirror images of each other since the dimensionless EPC $\lambda_D = \lambda^2/(\omega_0^2 W)$ increases with λ, but decreases with ω_0.

It is interesting to ascertain the extent to which the physics of the Holstein Hamiltonian is determined by λ and ω_0 separately, versus only the combination λ_D. Figure 5.8 addresses this issue by replotting the data of Figs. 5.7(a,b) as a function of λ_D for two values of the inverse temperature. For $\lambda_D \gtrsim 0.8$, the data collapse well, whereas at small λ_D $S_{\rm cdw}$ can vary by as much as a factor of two even though λ_D is identical. It is suggestive that this disagreement occurs near the region of the QCP. (See Fig. 5.13.)

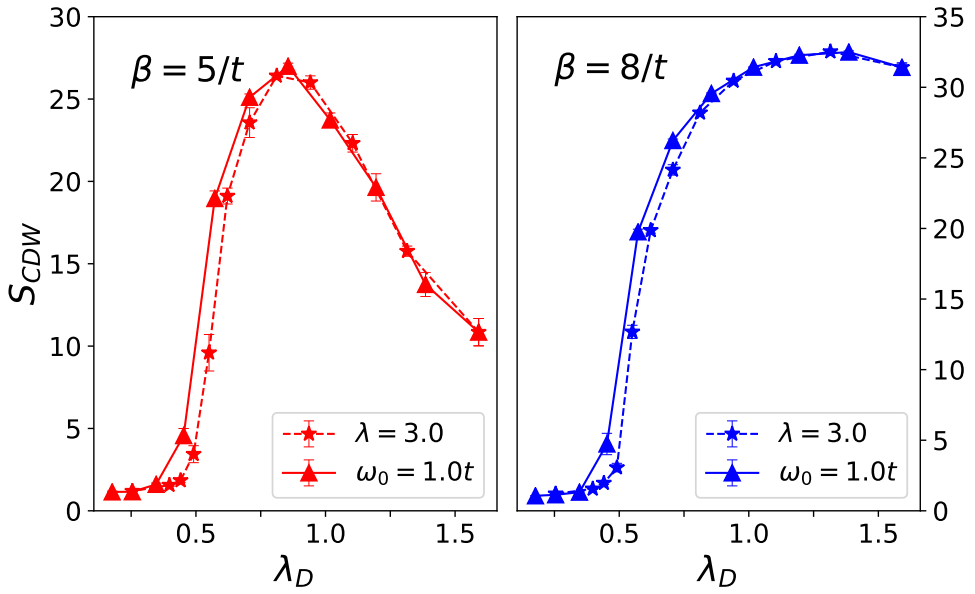

FIGURE 5.8. Comparison of the evolution of S_{cdw} with coupling strength by changing λ or changing ω_0. Data are taken from Fig. 5.7(a,b), for $\beta = 5/t$ (left) and $\beta = 8/t$ (right). The difference is negligible at $\lambda_D > 0.8$ but not in the coupling regime $0.4 < \lambda_D < 0.8$ near the QCP. (See Fig. 5.13.)

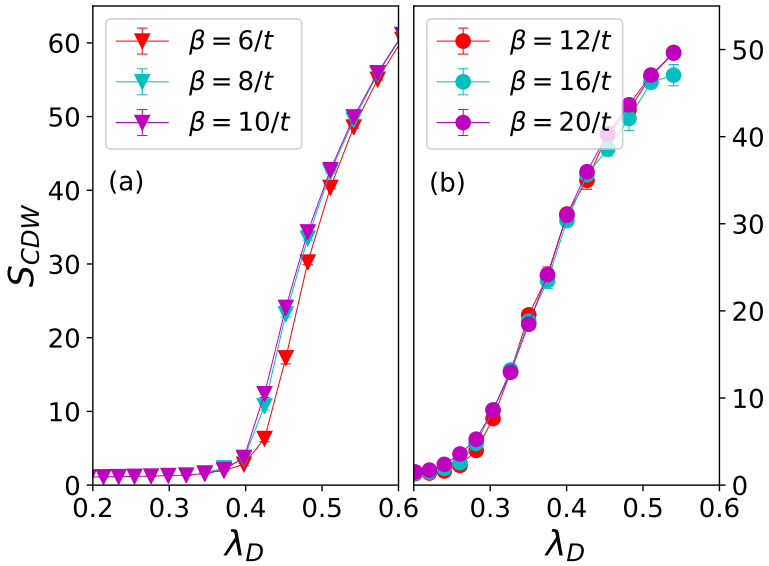

FIGURE 5.9. S_{cdw} as a function of λ_D for π-flux phase square lattice (left) and honeycomb model (right). The lattice size $L = 6$ is used for both geometries. λ_D is varied by changing λ at fixed $\omega_0 = 1.0\,t$. S_{cdw} does not change for the lowest temperatures, indicating that the ground state has been reached for this finite lattice size.

We compare the semi-metal to CDW transition with increasing λ_D for the π-flux phase and honeycomb lattices in Fig. 5.9. These data are at lower temperatures than those of Fig. 5.8, so that the ground state values of $S_{\rm cdw}$ have been reached for the system sizes shown.

5.4.3. Ground state in the (λ, ω_0) plane. Figure 5.10 provides another perspective on the dependence of the CDW order on λ and ω_0 individually, by giving a heat map of $S_{\rm cdw}$ in the (λ, ω_0) plane at low temperature. The bright yellow in upper-left indicates a strong CDW phase, whereas the dark purple region in lower-right indicates the Dirac semi-metal phase. The phase boundary is roughly linear, as would be expected if only the combination $\lambda_D = \lambda^2/(\omega_0^2 W)$ is relevant. We note, however, that this statement is only qualitatively true. The more precise line graphs of Fig. 5.8 indicate that along the line $\lambda = \sqrt{\lambda_{D,\rm crit} W}\,\omega_0 \sim 1.5\,\omega_0$, the separate values of λ and ω_0 are relevant.

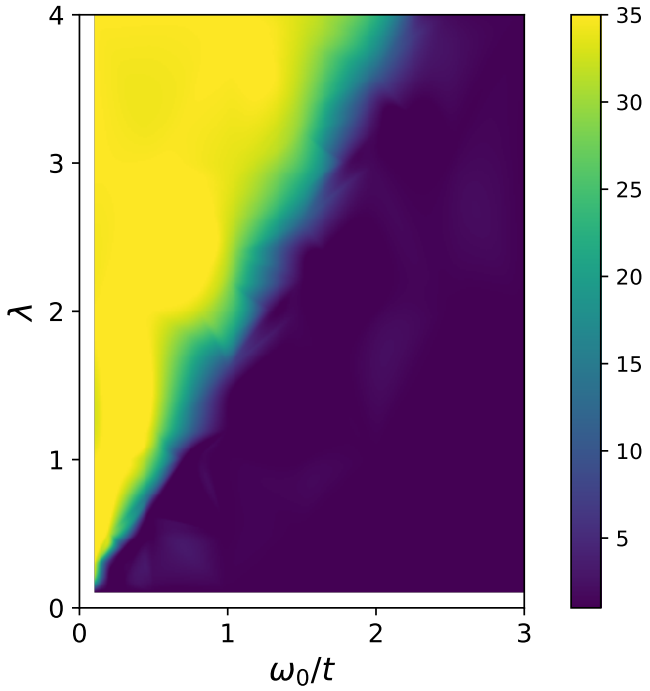

FIGURE 5.10. Heat map of the ground state values of $S_{\rm cdw}$ in the (λ, ω_0) plane.

5.4.4. Finite size scaling: finite T transition. A quantitative determination of the finite temperature and quantum critical points can be done with finite size scaling (FSS). Figure 5.11 gives both raw and scaled data for $S_{\rm cdw}$ for different lattice sizes $L = 4, 6, 8, 10$ at $\lambda = 2.0$, $\omega_0 = 1.0\,t$ as a function of β. Unscaled data are in panel (a): $S_{\rm cdw}$ is small and L-independent at small β

(high T) where $c(\mathbf{r})$ is short ranged. On the other hand, $S_{\rm cdw}$ is proportional to $N = L^2$ at large β (low T), reflecting the long-range CDW order in $c(\mathbf{r})$. Panel (b) shows a data crossing for different L occurs when $S_{\rm cdw}/L^{\gamma/\nu}$ is plotted versus β. A universal crossing is seen at $\beta\, t \sim 3.80 \pm 0.02$, giving a precise determination of critical temperature T_c. The 2D Ising critical exponents $\gamma = 7/4$ and $\nu = 1$ were used in this analysis, since the CDW phase transition breaks a similar discrete symmetry. Panel (c) shows a full data collapse when the β axis is also appropriately scaled by $L^{1/\nu}$. The best collapse occurs at $\beta_c = 3.80/t$, consistent with the result from the data crossing.

In the region immeditely above the QCP, the DQMC values for T_c are roughly five times lower than those obtained in MFT, and, indeed, the MFT over-estimation of T_c can be made arbitrarily large at strong coupling. This reflects both the relatively low dimensionality ($d = 2$) and the fact that MFT fails to distinguish moment-forming and moment-ordering temperature scales.

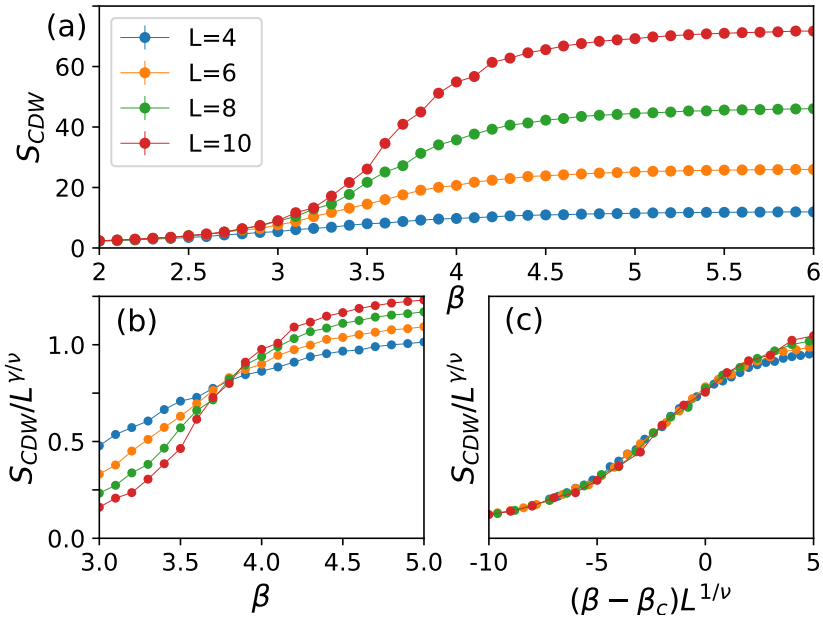

FIGURE 5.11. (a) The CDW structure factor $S_{\rm cdw}$ as a function of β for several lattice sizes. (b) The scaled CDW structure factor $S_{\rm cdw}/{\rm L}^{\gamma/\nu}$ as a function of β using Ising critical exponents $\gamma = 7/4$ and $\nu = 1$, showing a crossing of different L at $\beta_c = 3.80/t$. (c) $S_{\rm CDW}/{\rm L}^{\gamma/\nu}$ versus $(\beta - \beta_c){\rm L}$, giving a best data collapse at $\beta_c = 3.80/t$. Here the parameters are $\lambda = 2.0$ and $\omega_0 = 1.0\, t$.

5.4.5. Quantum phase transition. Analysis of the renormalization group invariant Binder cumulant [126],

$$\mathcal{B} = \frac{3}{2}\left(1 - \frac{1}{3}\frac{< S_{\rm cdw}^2 >}{< S_{\rm cdw} >^2}\right), \tag{5.8}$$

can be used to locate the quantum critical point precisely. Only lattice sizes $L = 4n$ where n is an integer can be used, for other L the Dirac points are not one of the allowed $\mathbf{k}$ values and finite size effects are much more significant. As exhibited in Fig. 5.12, for $L = 4, 8$ and 12, $\mathcal{B}$ exhibits a set of crossings in a range about $\lambda_D \approx 0.4$. An extrapolation in $1/L$, as shown in the inset of Fig. 5.12, gives $\lambda_{D,\rm crit} = 0.371 \pm 0.003$.

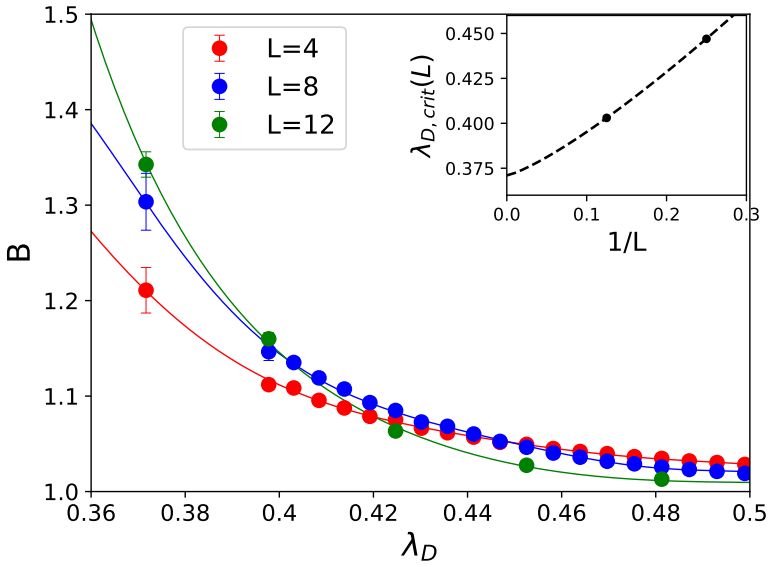

FIGURE 5.12. Main panel: Binder cumulant as a function of EPC strength λ_D for three lattice sizes. Inverse temperature is $\beta = 2\,L$ and ω_0 is fixed at $\omega_0 = 1.0\,t$. Inset: Extrapolation of the crossings for pairs of sizes as a function of $1/L$ to get the QCP in the thermodynamic limit.

5.4.6. Phase diagram. Location of the finite temperature phase boundary, Fig. 5.11, and the QCP, Fig. 5.12, can be combined into the phase diagram of Fig. 5.13. Results for the π-flux geometry (blue circles) are put in better context by compared with those of the honeycomb lattice (red triangles). Data were obtained at fixed $\omega_0 = 1.0\,t$. In both geometries, phase transitions into CDW order happen only above a finite $\lambda_{D,\rm crit}$. Beyond $\lambda_{D,\rm crit}$, T_c rises rapidly to its maximal

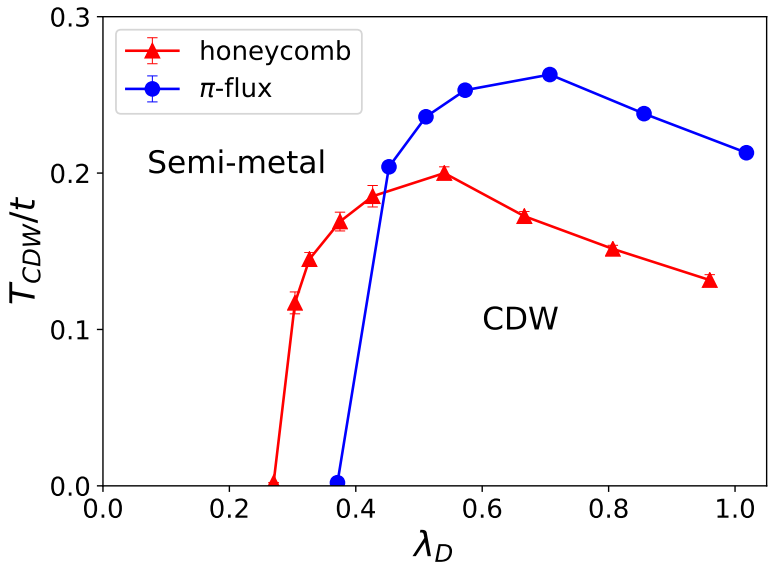

FIGURE 5.13. Critical temperature T_c for CDW phase transition, obtained from DQMC for both π-flux phase square lattice (blue line) and the honeycomb lattice (red line), in a range of coupling strength. λ_D is varied by changing λ at fixed $\omega_0 = 1.0\,t$ for both models. Quantum critical point is determined using Binder cumulant analysis (discussed below). Data for the honeycomb lattice are taken from [3] Error bars are smaller than symbol size for π-flux data.

value before decaying. For π-flux model, T_c reaches a maximum $T_{c,\max}/t \sim 0.26$ at $\lambda_D \sim 0.7$, whereas for the honeycomb lattice T_c reaches its maximum $T_{c,\max}/t \sim 0.20$ at $\lambda_D \sim 0.5$. Similarly $\lambda_{D,crit}$ for π-flux is larger than that of the honeycomb lattice, as $\lambda_{D,crit} = 0.42$ and 0.27 respectively. When measured in terms of the relative Fermi velocities $v_{\rm F} = 2\,t,\ 1.5\,t$ for the π-flux and honeycomb respectively, these values become very similar: $\lambda_{D,\rm crit}/v_{\rm F} = 0.21$ and 0.18 for π-flux and honeycomb; $T_{c,\max}/v_{\rm F} = 0.13$ and 0.13.

5.5. Conclusions

This chapter has determined the quantitative phase diagram for Dirac fermions interacting with local phonon modes on the π-flux lattice. A key feature, shared with the honeycomb geometry, is the presence of a quantum critical point $\lambda_{D,\rm crit}$ below which the system remains a semi-metal down to $T = 0$. The values of T_c and $\lambda_{D,\rm crit}$ for the two cases, when normalized to the Fermi velocities, agree to within roughly 10%.

We have also considered the question of whether the properties of the model can be described in terms of the single ratio λ^2/ω_0^2. We find that qualitatively this is indeed the case, but that, quantititively, the charge structure factor can depend significantly on the individual values of EPC and phonon frequency, especially in the vicinity of the QCP. However this more complex behavior is masked by the fact that T_c rises so rapidly with λ in that region. In investigating this issue we have studied substantially smaller values of ω_0 than have typically been investigated in QMC treatments of the Holstein Hamiltonian.

CHAPTER 6

Orbital Selective Charge Density Wave Transitions

6.1. Introduction

Over the last several decades, much attention has been focused in the condensed matter community on layered materials. One prominent example is that of the cuprate superconductors (SC) [161, 162, 163, 164, 165]. Bilayer graphene [166, 167, 168, 169, 170, 171] is another, more recent, realization. From a theoretical perspective, bilayer materials offer an opportunity to explore the competition between the formation of long range order at weak interlayer coupling and collections of independent local degrees of freedom in the limit of strong interlayer coupling. Computational studies have lent considerable insight into these phenomena, including quantitative values for the quantum critical points [172, 173, 174, 175, 176] separating antiferromagnetic and singlet phases at zero temperature.

This competition is central to that which occurs in multiorbital systems, notably the interplay of Ruderman-Kittel-Kasuya-Yosida order and singlet formation in the Kondo lattice and periodic Anderson models [177, 178, 179]. This close analogy originates in the observation that, in calculations on a model Hamiltonian, there is no difference between multi-layer and multi-orbital descriptions, apart from the interpretation of the additional label of the fermionic species : in both Hamiltonians, there are multiple species of electrons on the same spatial site, and different species can interact via hopping or interaction. For this reason we will use the two terminologies interchangeably here. In multi-orbital language, one of the key conceptual interests is the possibility that the distinct values of the ratio of interaction strength to kinetic energy in the different bands might result in *separate* insulator transitions, i.e. the possibility of an 'orbital-selective' Mott transition (OSMT) [180, 181, 182, 183, 184, 185, 186, 187, 188, 189, 190, 191].

Here we study analogous questions concerning bilayer (bi-orbital) systems in which the fermions interact with phonon degrees of freedom rather than via direct electron-electron correlations. A precise mathematical description of the mapping between the two situations is discussed. Quantum Monte Carlo (QMC) simulations have already been applied to the analysis of charge-density wave (CDW) and superconducting (SC) transitions in the single band Holstein model [39]. However, thus far, work has focused mostly on two-dimensional or three-dimensional models with a single kinetic energy scale [3, 41, 49, 51, 53, 54, 55, 56, 58, 59, 154, 192, 193, 194].

Using QMC simulations of the two-band Holstein model at half-filling, we will address the following questions concerning the effects of interband hybridization t_3: (i) Is there a transition in which CDW order is destroyed as t_3 is increased? What is the value of the critical coupling associated with the quantum critical point (QCP) in the ground state and the critical temperature for the thermal transitions at finite T? (ii) In a situation where the electron-phonon energy scales in the two bands are very different, can CDW order in one band coexist with metallic behavior in the other? These issues are in direct analogy with those addressed in multiband Hubbard Hamiltonians; we will discuss similarities and differences between the resulting phenomena.

6.2. Layered Holstein Hamiltonian

We focus on the bilayer Holstein model

$$\begin{aligned}\hat{\mathcal{H}} = &- \sum_{\langle ij\rangle,l,\sigma} \left(t_l\ \hat{c}^{\dagger}_{il\sigma}\hat{c}_{jl\sigma} + \text{h.c.}\right) - \sum_{i,l,\sigma} \mu_l \hat{n}_{il\sigma} \\ &+ \frac{1}{2M}\sum_{il} \hat{P}^2_{il} + \frac{1}{2}\sum_{i,l} \omega_l^2 \hat{X}^2_{il} + \sum_{i,l,\sigma} \lambda_l\, \hat{n}_{il\sigma}\hat{X}_{il} \\ &- \sum_{i,\langle ll'\rangle,\sigma} \left(t_{ll'}\ \hat{c}^{\dagger}_{il\sigma}\hat{c}_{il'\sigma} + \text{h.c.}\right) . \end{aligned} \tag{6.1}$$

$\hat{c}_{il\sigma}(\hat{c}^{\dagger}_{il\sigma})$ are annihilation (creation) operators for an electron on layer $l(=\pm 1)$, site i with spin σ, and $\hat{n}_{il\sigma} = \hat{c}^{\dagger}_{il\sigma}\hat{c}_{il\sigma}$ is the number operator. t_l and $t_{ll'} = t_3$ denote the intra- and inter-layer hopping respectively. Phonons are represented by local (dispersionless) quantum harmonic oscillators with frequency ω_l, and on-site electron-phonon interaction on layer l is introduced via λ_l. We choose intralayer hopping $t_l = t = 1$ throughout this work to set the energy scale, and all simulations are

done at half-filling $\langle \hat{n}_{il} \rangle = 1$, which can be achieved by setting the chemical potential $\mu_l = -\lambda_l^2/\omega_l^2$; phonon mass is set as $M = 1$. Each layer is an $L \times L$ site square lattice, as sketched in Fig. 6.1(a), with $N = 2 \times L \times L$ being the total number of sites. We focus on two cases in this work: a uniform bilayer Holstein model where $t_1 = t_{-1} = t$, $\mu_1 = \mu_{-1} = \mu$, $\omega_1 = \omega_{-1} = \omega$ and $\lambda_{+1} = \lambda_{-1} = \lambda$; and an interface between Holstein layer and "metal" layer, where only layer $l = +1$ has a non-zero electron-phonon coupling $\lambda_{+1} \neq 0$ and layer $l = -1$ has $\lambda_{-1} = 0$. We employ a recently developed Langevin quantum Monte Carlo (QMC) method [2] discussed in the next section.

We first define the local observables including the (layer-dependent) double occupancy,

$$\mathcal{D}_l \equiv \langle \hat{n}_{il\uparrow} \hat{n}_{il\downarrow} \rangle \tag{6.2}$$

the near-neighbor intra-layer Green's function,

$$\mathcal{G}_{\langle ij \rangle l} \equiv -\langle \hat{c}^\dagger_{il\sigma} \hat{c}_{jl\sigma} + \hat{c}^\dagger_{jl\sigma} \hat{c}_{il\sigma} \rangle \,, \tag{6.3}$$

and the near-neighbor inter-layer Green's function,

$$\mathcal{G}_{\langle ll' \rangle} \equiv -\langle \hat{c}^\dagger_{il\sigma} \hat{c}_{il'\sigma} + \hat{c}^\dagger_{il'\sigma} \hat{c}_{il\sigma} \rangle \,. \tag{6.4}$$

When multiplied by their associated hopping integrals, $t\,\mathcal{G}_{\langle ij \rangle l}$ and $t_3\,\mathcal{G}_{\langle ll' \rangle}$ give the intra- and inter-layer kinetic energies per site.

Two further observables, the density-density and pair-pair correlators, aid in characterizing the excitations between the planes.

$$\begin{aligned} d_{-1,1} &\equiv \frac{1}{4} \langle \hat{n}_{i,1} \hat{n}_{i,-1} - 1 \rangle \\ p_{-1,1} &\equiv -\frac{1}{4} \langle \hat{\Delta}_{i,1} \hat{\Delta}^\dagger_{i,-1} + \hat{\Delta}^\dagger_{i,1} \hat{\Delta}_{i,-1} \rangle \\ \hat{\Delta}^\dagger_{il} &\equiv \hat{c}^\dagger_{il\uparrow} \hat{c}^\dagger_{il\downarrow}. \end{aligned} \tag{6.5}$$

$d_{-1,1}$ and $p_{-1,1}$ are the analogs of the zz and xy spin correlations which enter into the characterization of interlayer singlet formation in the Hubbard and Heisenberg bilayers, see section 6.6. Because of rotational symmetry of those models, their magnetic analogs, obtained by the transformation $\hat{c}_{il\downarrow} \to \hat{c}^\dagger_{il\downarrow}$ (particle-hole transformation) are identical in value. $d_{-1,1} = p_{-1,1}$

would also hold in the attractive Hubbard Hamiltonian. Here, in the Holstein model, rotational symmetry is broken and we have $d_{-1,1} \neq p_{-1,1}$. We will discuss the implications further in the sections to follow.

Characterization of the CDW formation in the thermodynamic limit can be made by the analysis of the structure factor,

$$S_l^{\rm cdw} = \frac{2}{N} \sum_{ij} (-1)^{i+j} \langle \hat{n}_{il} \hat{n}_{jl} \rangle, \tag{6.6}$$

with $\hat{n}_{il} = \sum_\sigma \hat{n}_{il\sigma}$. It samples correlations across the entire lattice, and hence is a primary tool in the determination of long range order.

In the case of the uniform bilayer, the quantities defined in Eqs. 6.2-6.4 and 6.6 are independent of the layer index l, and in this case we suppress this index. But for the 'interface' geometry, which includes one layer with $\lambda_1 \neq 0$ and another with $\lambda_{-1} = 0$, measurements performed on the two layers are inequivalent.

The layer-resolved single-particle spectral function $A_l(\omega)$ is obtained by using the maximum entropy method to invert the integral equation relating the imaginary time dependent Green's function $G_{i=0}(\tau)$ and $A(\omega)$:

$$G_{i=0}(\tau) = \int d\omega \frac{e^{-\tau\omega}}{1+e^{\beta\omega}} A(\omega)$$

$$G_i(\tau) = \langle c_i(\tau) c_0^\dagger(0) \rangle = \langle e^{\tau\mathcal{H}} c_i(0) e^{-\tau\mathcal{H}} c_0^\dagger(0) \rangle \,. \tag{6.7}$$

τ represents imaginary time; layer and spin index is omitted here for simplicity. The appropriate local G is used to get $A_l(\omega)$ for the each layer l in the interface geometry.

We advance our key results in Figures 6.1(b) and 6.1(c): (i) At weak t_3 there is a phase transition at finite temperature T_c to a state with long range charge order. In the bilayer case, T_c initially increases with t_3 as the charge order is enhanced by increased coordination number. (ii) At $T = 0$, in both the Holstein bilayer and the Holstein-metal interface, CDW order is destroyed for t_3 exceeding a quantum critical value. (iii) The phase diagram of the interface geometry exhibits an 'orbitally selective CDW phase' (OSCDW) at low T and weak t_3. The specific description of

how these phase diagrams are obtained is given in the corresponding section containing the main results of each model.

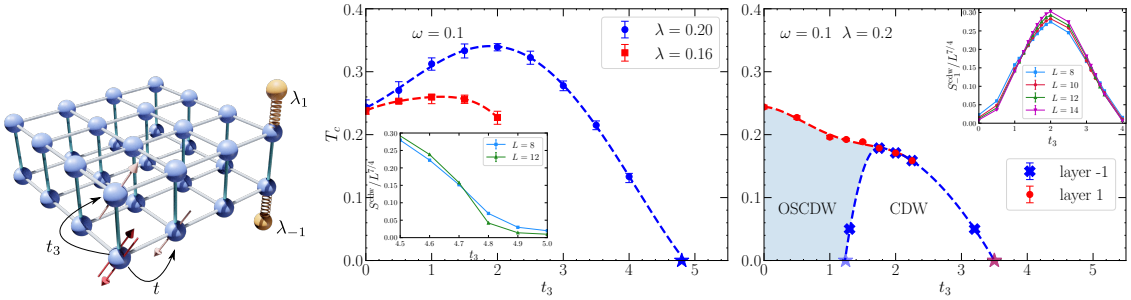

FIGURE 6.1. (a) Sketch of a bilayer with relevant terms in Eq. (6.1) marked. (b) Phase diagram of the Holstein bilayer giving the CDW transition temperature T_c as a function of inter-layer hopping t_3. Two values of electron-phonon coupling, $\lambda = 0.2$ and $\lambda = 0.16$, are shown. Dashed lines are guides to the eye. Inset shows crossing plot of $S^{\rm cdw}/L^{7/4}$ versus t_3 at $\lambda = 0.2$ and low temperature $\beta = 20$. (c) Analog of (b), but for the Holstein-metal interface. Two crossings at $t_3 \sim 1.3$ and $t_3 \sim 3.2$ are revealed in the inset for layer $l = -1$. The CDW phase in this layer is present only in the region between the two crossings. QCPs are marked by stars on x-axis in both panel (b) and (c). Phonon frequency is set at $\omega = 0.1$ for all data.

6.3. Holstein bilayer

We initially consider two identical layers with $\lambda = 0.2, \omega = 0.1$ and the question of the destruction of CDW order via the formation of "charge singlets" , i.e. a charge analog of singlet (spin liquid) physics, at large interlayer hopping t_3 before tackling the more complex issue of selective CDW transitions.

Figure 6.2(a) gives the CDW structure factor $S^{\rm cdw}$ as a function of t_3 at low temperature for two lattice sizes. Below $t_{3,c} \approx 4.8$, $S^{\rm cdw}$ is large, and grows with lattice size, suggesting long range charge order. Figure 6.2(b) focuses on the interlayer density-density $d_{-1,1}$ and pair-pair $p_{-1,1}$ correlations. For small t_3, only $d_{-1,1}$ is large in magnitude, indicating coherence in the charge order between the two layers. As t_3 increases, intersheet pair correlations $p_{-1,1}$ develop. $d_{-1,1}$ and $p_{-1,1}$ then become nearly degenerate at $t_{3,c}$, signalling the loss of CDW order and entry into the 'charge singlet' phase. Together, Figs. 6.2(a) and 6.2(b) motivate the bilayer phase diagram of Fig. 6.1(b).

Although the QCP in this Holstein bilayer is closely analogous to that occurring in Hubbard and Heisenberg bilayers as well as the periodic Anderson model, in those cases the electron-electron

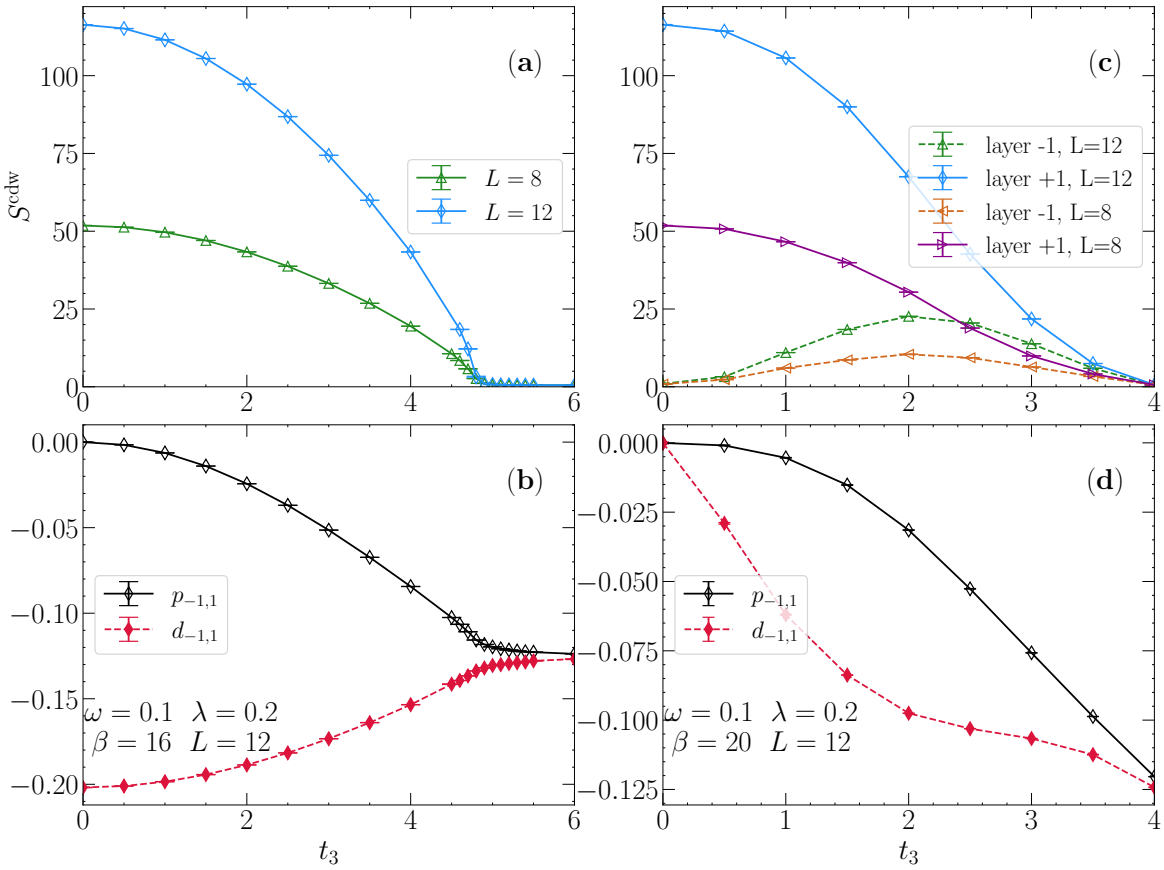

FIGURE 6.2. (a) Charge structure factor $S^{\rm cdw}$; and (b) $p_{-1,1}$ and $d_{-1,1}$ as a function of interlayer hopping t_3 for the Holstein bilayer at low temperature $\beta = 16$ and $\lambda_{+1} = \lambda_{-1} = 0.2$. $S^{\rm cdw}$ shows significant finite size effects in the ordered phase $t_3 \lesssim 4.8$. Note that $d_{-1,1}$ vanishes at $t_3 = 0$, but jumps discontinuously to a non-zero value for infinitesmal t_3. Panels (c,d) are analog of (a,b) for the Holstein-metal interface. The two curves in (c) correspond to layers $l = +1$ and $l = -1$, with $\lambda_{+1} = 0.2$ and $\lambda_{-1} = 0$ respectively and temperature $\beta = 20$. In all plots the phonon frequency is set at $\omega = 0.1$.

interaction gives rise to magnetic phases which form due to the breaking of a *continuous* spin symmetry. Thus in 2D and quasi-2D geometries, no long range order is possible at finite T. In contrast, here for the Holstein model, charge and pairing order are not degenerate, as emphasized by the data of Fig. 6.2(b). CDW correlations dominate at half-filling and a finite temperature phase transition can occur, terminating at a QCP as shown in Figs. 6.1(b) and 6.1(c). This distinction means that, in principle, our characterization of the unordered phase as a 'charge singlet' is somewhat loose: in the usual spin singlet the x, y, z components of the spin-spin correlations on

the two layers (or in the two orbitals) are equal. With that said, the equivalence of $p_{-1,1}$ and $d_{-1,1}$ in the large t_3 regime points to an emergent restoration of the symmetry (see section 6.6). It is worth noting that in the absence of t_3, e.g. in the 2D Holstein model, this restoration does not occur until the anti-adiabatic limit is reached, which requires very large values of ω [57].

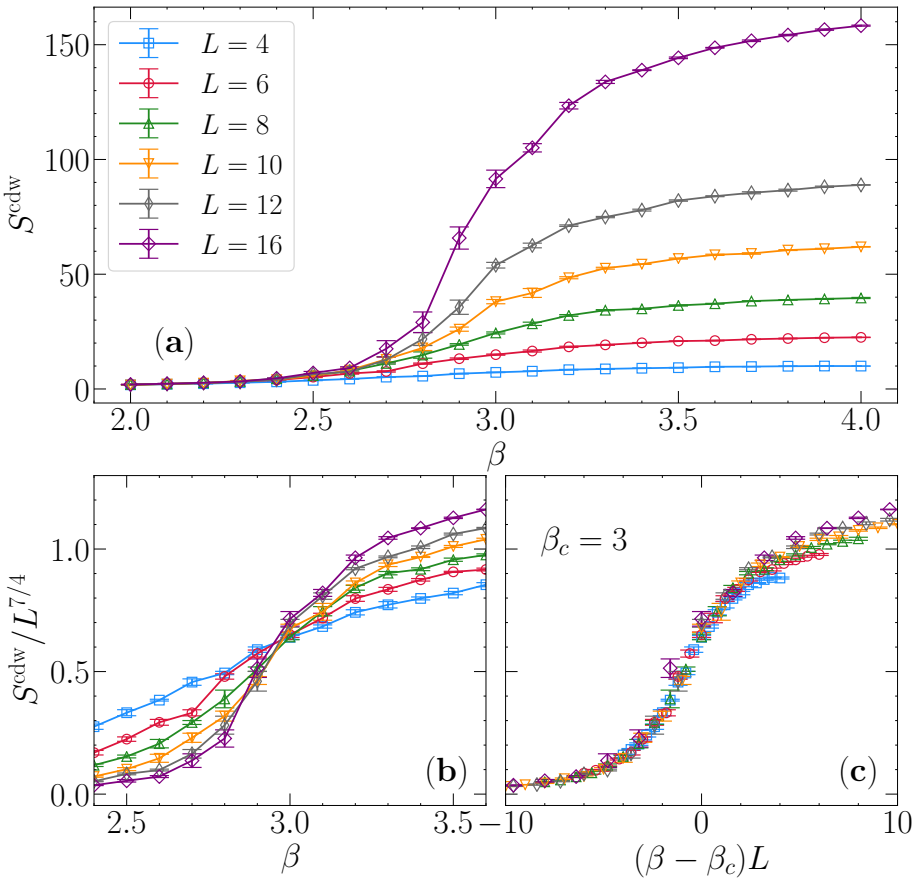

FIGURE 6.3. (a) CDW structure factor S^{cdw} dependence on the inverse temperature β and finite size scaling of the Holstein bilayer at $t_3 = 2$. Both the crossing plot (b), and the full data collapse (c) using 2D Ising critical exponents and $\beta_c \simeq 3.0$.

Figure 6.3 provides details of the behavior of the CDW structure factor. The top panel (a) gives raw values for S^{cdw} as a function of β at $t_3 = 2$ for different lattice sizes. At low β (high temperature), the correlation length ξ is short and S^{cdw} is independent of L. As β increases, so does ξ and when $\xi \sim L$, S^{cdw} becomes sensitive to L. This separation of the curves provides a crude estimate for β_c, which may then be determined precisely by finite size scaling (FSS).

In particular, in the vicinity of the critical temperature T_c, the CDW structure factor measured on finite lattices of linear dimension L should obey,

$$S^{\rm cdw} \sim L^{\gamma/\nu} f\left(\frac{T-T_c}{T_c} L^{1/\nu}\right) \ . \tag{6.8}$$

As a consequence, when plotting $S^{\rm cdw}/L^{\gamma/\nu}$ as a function of the inverse temperature β, different sizes L cross at $\beta = \beta_c$ [Fig. 6.3 (b)]. Following the scaling form given in Eq.(6.8) we note that when plotted against $(\beta - \beta_c)L^{1/\nu}$ all data collapse on a single curve – see Figs. 6.3(c) (and later for the Holstein-metal interface in Fig. 6.5). In this analysis we have used the critical exponents of the 2D Ising universality class ($\gamma = 7/4$ and $\nu = 1$), since the CDW phase breaks a Z_2 symmetry. A discussion of the degree to which the collapse worsens, and hence the accuracy with which the exponents can be determined, is given in the Appendix B.

Using such scaling procedure for various values of the interplane hybridization, allows us to extract the location of the thermal transition, as compiled in Fig. 6.1(b), using two values of the electron-phonon interaction. In this geometry, the critical temperature T_c initially increases as a consequence of the larger coordination number when the planes are coupled - the 2D to 3D crossover. However, at large t_3 the critical temperature decreases and ultimately vanishes at a quantum critical point.

6.4. Holstein-metal interface

We next consider the 'Holstein-metal interface' in which layer $l = +1$ has nonzero λ_{+1} but $\lambda_{-1} = 0$. The two layers are in contact via hybridization. Here, in addition to the question of charge singlet formation at large t_3, quenching CDW order, a different fundamental question arises: to what extent do CDW correlations in layer $l = +1$ 'penetrate' into layer $l = -1$, and, conversely, is the CDW in layer $l = +1$ disrupted by contact with the 'metallic' layer? We choose $\lambda = 0.2$ and $\omega = 0.1$ as in the previous section.

Figure 6.2(c) shows the CDW structure factor $S^{\rm cdw}$ in the two layers. $S^{\rm cdw}_{+1}$ decreases steadily with t_3: additional quantum fluctuations associated with contact with the metal reduce charge order. In contrast, $S^{\rm cdw}_{-1}$ is non-monotonic: charge order is initially induced in the metal via contact with the Holstein layer, but ultimately large t_3 is inimical to it. The behavior of $S^{\rm cdw}_{-1}$

provides a first clue that order in layer $l = -1$ might occur only for intermediate t_3. Figure 6.2(d) gives the interlayer density-density $d_{-1,1}$ and pair-pair $p_{-1,1}$ correlations for this interface geometry. The primary difference from the original bilayer case is the gradual development of $d_{-1,1}$ with t_3. This is a consequence of the absence of CDW in the metal layer when t_3 vanishes. The interlayer hopping thus must not only couple the charge correlations, but also induce them in layer $l = -1$. Similar to the bilayer case, $d_{-1,1}$ and $p_{-1,1}$ become degenerate for large t_3. This is again a signature of entering into the charge singlet phase.

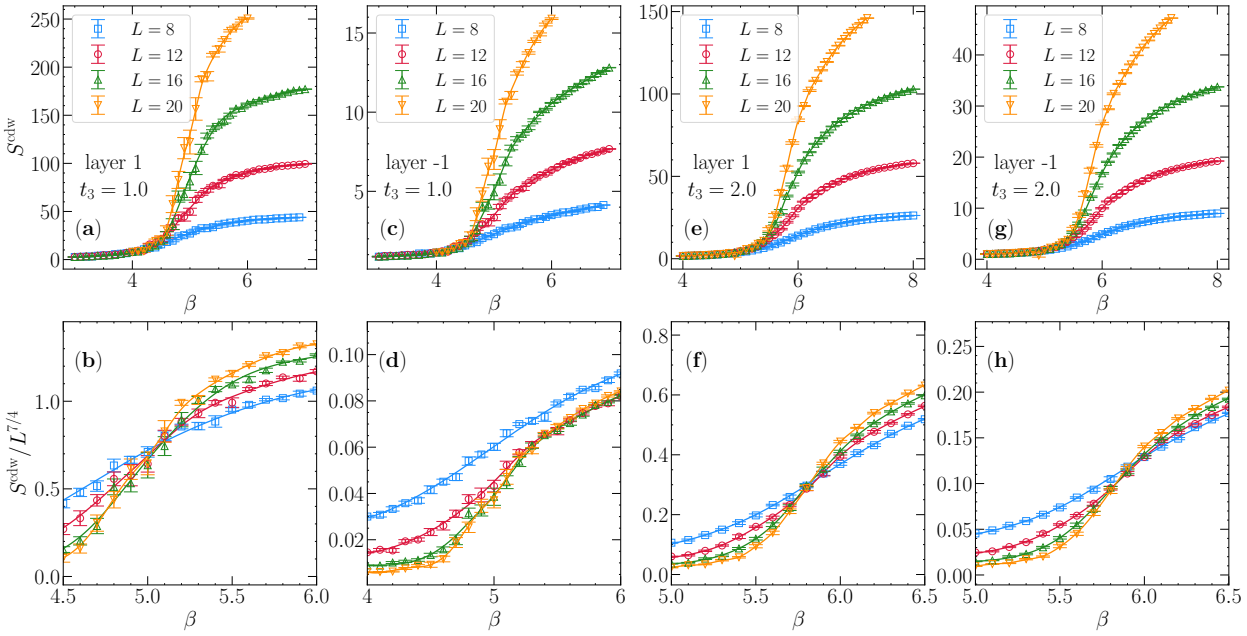

FIGURE 6.4. (a) CDW structure factor, $S^{\rm cdw}$, dependence on the inverse temperature, β, for layer 1 of the Holstein interface at $t_3 = 1$; (b) using 2D Ising critical exponents for finite size scaling (FSS). Panels (c) and (d) display the same but for the metallic layer $l = -1$. Panels (e–h) display the corresponding data for $t_3 = 2$. FSS in (f) and (h) show the same critical temperature for both layers at $t_3 = 2$, in contrast to $t_3 = 1$, where layer $l = +1$ (b) exhibits a clear CDW transition whereas data for layer $l = -1$ (d) does not exhibit crossing when using Ising critical exponents.

We now turn to a more careful FSS study of the layer-resolved $S^{\rm cdw}_l$. Our main interest is in determining how long range order in the two layers evolves with t_3. Figure 6.4 displays a detailed analysis of two representative values, $t_3 = 1$ and $t_3 = 2$. The former is a case when $S^{\rm cdw}_{-1}$ is just beginning to develop, and the latter is when $S^{\rm cdw}_{-1}$ has reached its maximal induced value [see

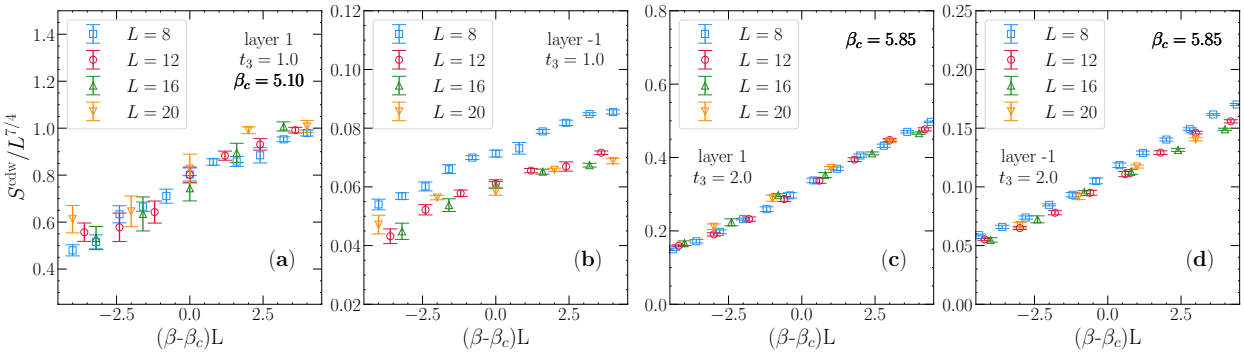

FIGURE 6.5. Full data collapse of the scaled CDW order parameter versus scaled reduced temperature in the 'Holstein interface' system. Only the Holstein layer (layer 1) shows a single universal curve for $t_3 = 1$ (a), while both collapse for $t_3 = 2t$ (panels b,d).

Fig. 6.2(c)]. There is a superficial resemblance in the unscaled data for both values of t_3, which rise as the temperature is lowered (β increases) and also increase with system size. A proper scaling analysis, however, reveals a profound distinction. As seen in Figs. 6.4(b) and 6.4(f), for both values of t_3, the layer $l = +1$ with non-zero electron-phonon coupling $\lambda_{+1} = 0.2$, has a scaled structure factor $L^{-7/4}S^{\rm cdw}_{+1}$ which exhibits a sharp crossing, indicating a finite temperature transition to long range CDW order. When $t_3 = 2$, this crossing occurs for the metallic layer with $\lambda_{-1} = 0$ as well [Fig. 6.4(h)]. However, when $t_3 = 1$ the data for the metallic layer do not cross for the studied system sizes [Fig. 6.4(d)], namely $L = 8 - 20$ for both t_3 values: L = 12,16 and 20 curves show collapse at $\beta > 5.4$ instead of crossing, whereas $L = 8$ data doesn't cross with other lattice sizes at all. Such distinction becomes even more apparent in Fig. 6.5, where a simultaneous data collapse for the scaled structure factor can be made possible at the same temperature for $t_3 = 2$, while it is unattainable for $t_3 = 1$.

We conclude that for $t_3 = 2$, the interface geometry has CDW order in both layers, with long range correlations in the metallic layer induced by proximity to the Holstein layer. For $t_3 = t$, the interface geometry exhibits *orbital selective* CDW order- the metal remains with only short range correlation despite its hybridization to the long range CDW layer. We emphasize that this conclusion is reinforced by the data in the inset to Fig. 6.1(b), where a low temperature ($\beta = 20$) sweep of the scaled $S^{\rm cdw}$ with t_3 has a pair of crossings $t_3 \sim 1.3$ and $t_3 \sim 3.2$. Long range CDW order exists in layer $l = -1$ only between these values.

6.5. Spectral functions and double occupancies

Having examined structure factors and inter-layer correlators, we now turn to the spectral functions and the double occupancies, both of which provide additional insight on the ground state properties. The layer-resolved spectral functions $A_l(\omega)$, shown in Fig. 6.6, the many-body analog of the single particle density of states, provide confirming evidence for the Holstein interface phase diagram of Fig. 6.1(c). In the top row, for small t_3, the Holstein layer $l = +1$ exhibits a CDW gap. The gap at $t_3 = 0$ is large; Hybridization with the metal produces peaks closer to $\omega = 0$, but a smaller gap remains. On the other hand the metal layer $l = -1$ has finite Fermi surface spectral weight $A_{-1}(\omega = 0) \neq 0$, thus showing the OSCDW. In the middle row, for intermediate t_3, both layers have a gap, consistent with the measurement of simultaneous long range CDW order. Finally, in the bottom row, for large t_3, both layers have finite Fermi surface spectral weight $A_l(\omega = 0) \neq 0$ for $l = +1, -1$. The system is in the charge singlet (charge liquid) phase.

We note that although the bilayer and interface geometries have many properties in common at large t_3, their spectral functions are different. There is a gap in the bilayer case, but not for the interface. We have verified, with separate exact diagonalization calculations, that for dimers (i.e. $t_3 \gg t$) with $\lambda_{+1} = \lambda_{-1}$ one finds $A(\omega)$ is gapped, while when λ_{+1} is nonzero $\lambda_{-1} = 0$ one reproduces the behavior shown in Fig. 6.6(c,f).

In a perfect CDW phase, half of the sites are doubly occupied and half are empty, and $\mathcal{D} = 0.5$. In the absence of interactions, $\lambda = 0$, all four site occupation possibilities $|0\rangle$, $|\uparrow\rangle$, $|\downarrow\rangle$, and $|\uparrow\downarrow\rangle$, are equally likely and $\mathcal{D} = 0.25$. This is also the case in the charge singlet phase. Figure 6.7 shows $\mathcal{D}$ as a function of t_3. Panel (a) is for the bilayer, where $\mathcal{D}_{+1} = \mathcal{D}_{-1}$, and panel (b) for the interface geometry where the two are inequivalent. In both cases, $\mathcal{D}_{+1}$ is seen to evolve between the CDW and singlet limits, although it never attains the value $\mathcal{D} = 0.5$ owing to the presence of quantum fluctuations. For the interface, $\mathcal{D}_{-1}$ begins at the uncorrelated value, $\mathcal{D}_{-1} = 0.25$ at $t_3 = 0$ since $\lambda_{-1} = 0$. The double occupancy evolution is quite similar to that of the structure factor, Fig. 6.2(a,c). However, since $\mathcal{D}$ is a local observable, it exhibits less sharp features than S^{cdw} in the vicinity of the QCP and thus only provides qualitative evidence for a cross-over between those two phases. Besides that, a simple model which exhibits a layer-dependent trivial CDW formation

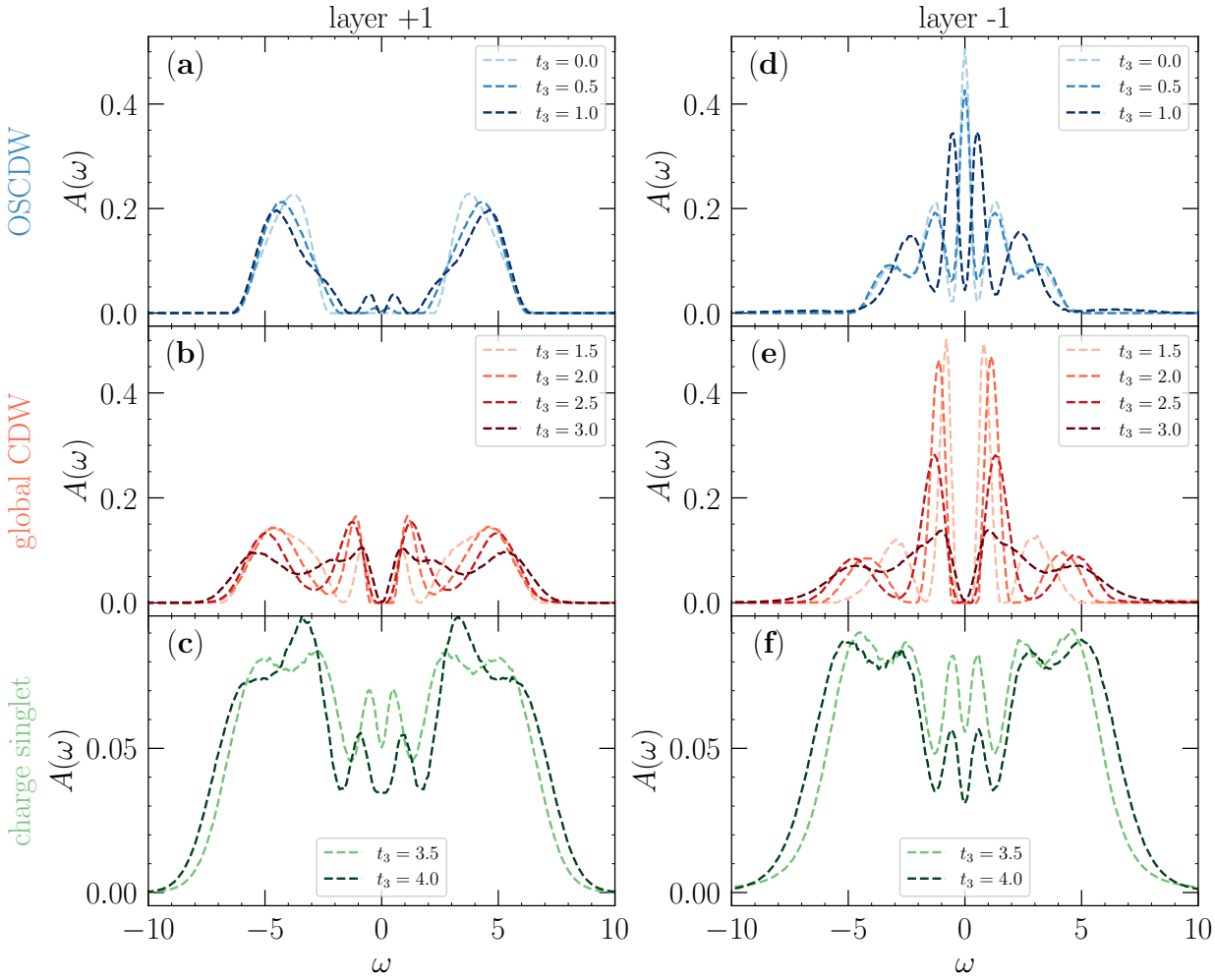

FIGURE 6.6. Spectral function $A(\omega)$ at $\beta = 12$ for several t_3 values cutting across the Holstein-metal interface phase diagram of Fig. 6.1. Top: Small t_3. Middle: Intermediate t_3. Bottom: Large t_3. Left and right columns correspond to Holstein and metallic layers $l = +1$ and $l = -1$ respectively.

with only electronic degrees of freedom, a bilayer ionic model, already displays this characteristic non-monotonicity with growing hybridization (see section 6.7).

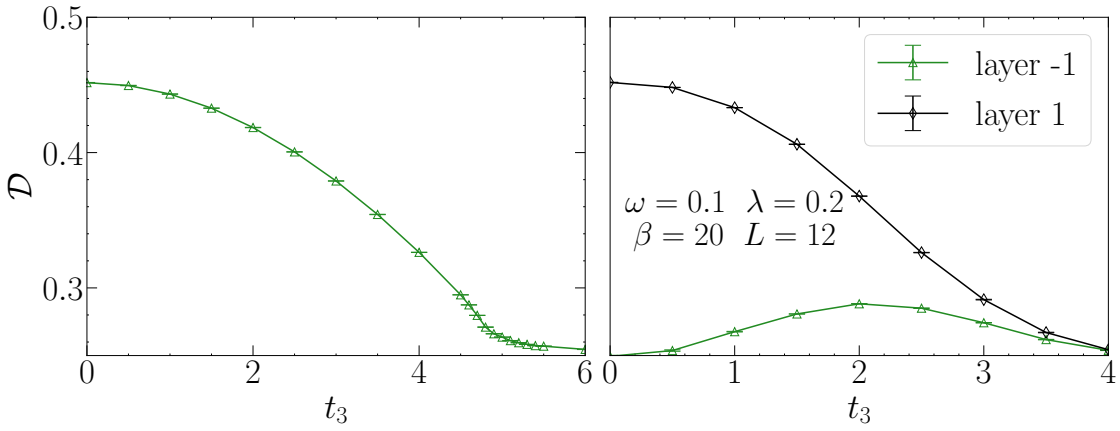

FIGURE 6.7. Double occupancy $\mathcal{D}$ shown as a function of interlayer hopping t_3 at low temperature $\beta = 20$. $\mathcal{D}$ is a local observable, and its value is the same for $L = 8$ and $L = 12$ to within the symbol size; we show the latter. (a) Holstein bilayer; (b) Holstein-metal interface. In (a) the two layers are equivalent and a single curve is shown. In (b) the green curve shows data on layer $l = -1$, whereas the grey curve represents layer $l = +1$.

6.6. Connection to magnetic language

In the repulsive 2D Hubbard model the dominant physics at half-filling on a bipartite lattice is anti-ferromagnetic order, characterized by the operators,

$$\begin{aligned}
\hat{S}^j_x &= \frac{1}{2}\big(\,\hat{S}^j_+ + \hat{S}^j_-\,\big) = \frac{1}{2}\big(\,\hat{c}^\dagger_{j\uparrow}\hat{c}_{j\downarrow} + \hat{c}^\dagger_{j\downarrow}\hat{c}_{j\uparrow}\,\big) \\
\hat{S}^j_y &= \frac{1}{2i}\big(\,\hat{S}^j_+ - \hat{S}^j_-\,\big) = \frac{1}{2i}\big(\,\hat{c}^\dagger_{j\uparrow}\hat{c}_{j\downarrow} - \hat{c}^\dagger_{j\downarrow}\hat{c}_{j\uparrow}\,\big) \\
\hat{S}^j_z &= \frac{1}{2}\big(\,\hat{n}_{j\uparrow} - \hat{n}_{j\downarrow}\,\big) = \frac{1}{2}\big(\,\hat{c}^\dagger_{j\uparrow}\hat{c}_{j\uparrow} - \hat{c}^\dagger_{j\downarrow}\hat{c}_{j\downarrow}\,\big)
\end{aligned} \tag{6.9}$$

From these relations, and as a consequence of the spin SU(2) symmetry of the Hubbard model,

$$\begin{aligned}
\langle \hat{S}^j_+\hat{S}^i_- + \hat{S}^j_-\hat{S}^i_+ \rangle &= 4\,\langle \hat{S}^j_z\hat{S}^i_z \rangle \\
\langle\, \hat{c}^\dagger_{j\uparrow}\hat{c}_{j\downarrow}\hat{c}^\dagger_{i\downarrow}\hat{c}_{i\uparrow} + \hat{c}^\dagger_{j\downarrow}\hat{c}_{j\uparrow}\hat{c}^\dagger_{i\uparrow}\hat{c}_{i\downarrow}\,\rangle &= \\
&\langle\, \big(\,\hat{c}^\dagger_{j\uparrow}\hat{c}_{j\uparrow} - \hat{c}^\dagger_{j\downarrow}\hat{c}_{j\downarrow}\,\big)\big(\,\hat{c}^\dagger_{i\uparrow}\hat{c}_{i\uparrow} - \hat{c}^\dagger_{i\downarrow}\hat{c}_{i\downarrow}\,\big)\,\rangle
\end{aligned} \tag{6.10}$$

If we perform a particle-hole transformation to the down spin fermions,

$$\begin{aligned}
\hat{c}^{\dagger}_{j\downarrow} &\rightarrow (-1)^j \hat{c}_{j\downarrow} \\
\hat{n}_{j\downarrow} &\rightarrow \big(1-\hat{n}_{j\downarrow}\big) \\
\hat{S}^j_+ = \hat{c}^{\dagger}_{j\uparrow}\hat{c}_{j\downarrow} &\rightarrow (-1)^j \hat{c}^{\dagger}_{j\uparrow}\hat{c}^{\dagger}_{j\downarrow} \equiv (-1)^j \hat{\Delta}^{\dagger}_j \\
\hat{S}^j_z = \frac{1}{2}\big(\hat{n}_{j\uparrow}-\hat{n}_{j\downarrow}\big) &\rightarrow \frac{1}{2}\big(\hat{n}_{j\uparrow}+\hat{n}_{j\downarrow}\big) \equiv \hat{n}_j
\end{aligned} \tag{6.11}$$

we conclude that,

$$-\langle \hat{\Delta}^{\dagger}_j \hat{\Delta}_i + \hat{\Delta}_i \hat{\Delta}^{\dagger}_j \rangle = \langle \big(\hat{n}_j - 1\big)\big(\hat{n}_i - 1\big)\big\rangle \tag{6.12}$$

assuming that sites i and j are on opposite sublattices.

If, finally, assuming we are at half-filling, so that $\langle \hat{n}_j \rangle = 1$,

$$-\langle \hat{\Delta}^{\dagger}_j \hat{\Delta}_i + \hat{\Delta}_i \hat{\Delta}^{\dagger}_j \rangle = \langle \hat{n}_j \hat{n}_i - 1 \rangle \tag{6.13}$$

This shows that the two correlation functions of Eq. 6.5 are equal: $p_{1,-1} = d_{1,-1}$. The merging of the two curves of Fig. 6.2(c,d) at a common value reflects a restoration of an SU(2) symmetry of the Hubbard model. It is interesting that this occurs even though the correlators are not in the singlet limit of $-1/4$ (due to the fact that we are not in Holstein analog of the large U limit).

6.7. Induced CDW in ionic Hubbard model

We can get additional insight into the Holstein interface by considering the following noninteracting, spinless, tight binding Hamiltonian,

$$\begin{aligned}
\hat{\mathcal{H}}_{\mathrm{BI-M}} = &-t \sum_{\langle ij\rangle, l} \big(\hat{c}^{\dagger}_{i,l}\hat{c}_{j,l} + \mathrm{h.c.}\big) + \delta \sum_i (-1)^i \hat{n}_{i,1} \\
&- t_3 \sum_j \big(\hat{c}^{\dagger}_{j,1}\hat{c}_{j,-1} + \mathrm{h.c.}\big).
\end{aligned} \tag{6.14}$$

Equation 6.14 describes two bands, labeled by $l = \pm 1$, each with hopping t on a 2D square lattice, which are hybridized with each other by t_3. Band $l = -1$ is metallic. At $t_3 = 0$ it has the usual 2D dispersion relation $\epsilon(k) = -2t\big(\cos k_x + \cos k_y\big)$. Band $l = +1$ is made insulating by the staggered

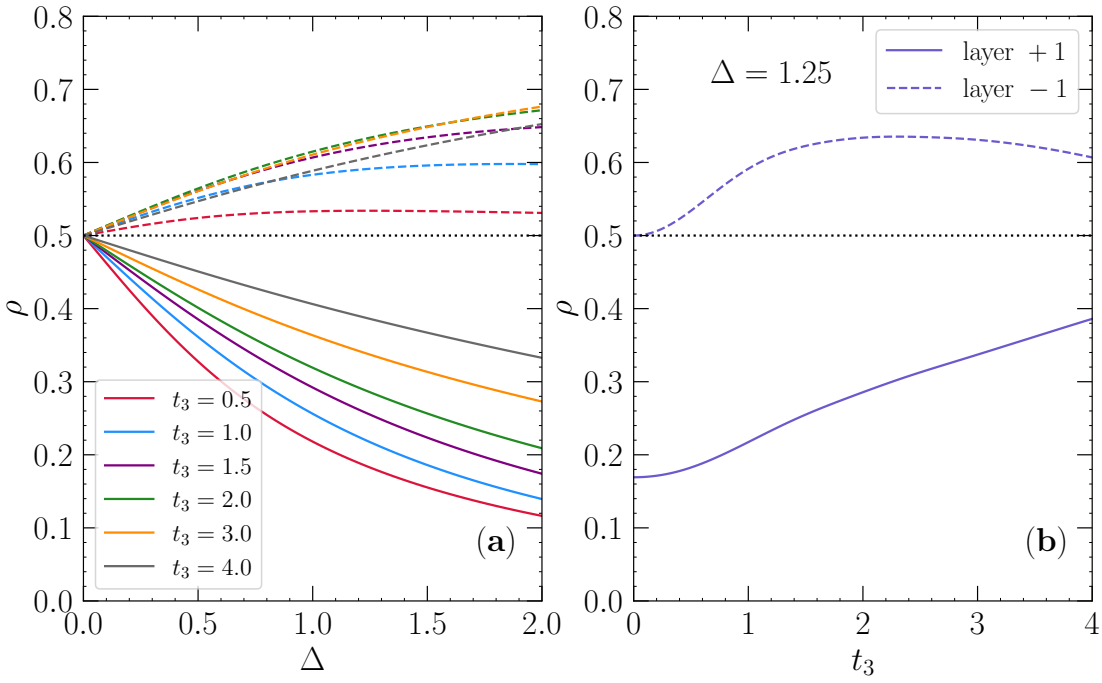

FIGURE 6.8. Solution of the tight binding Hamiltonian, Eq. 6.14. (a) Solid curves Occupations ρ on the $+\delta$ sites of the insulating band as functions of the magnitude of the staggered potential δ; Dashed curves: Occupations on the partner sites in the metallic band to which those $+\delta$ sites are hybridized by t_3. (b) Solid Curve: Occupations on the $+\delta$ sites of the insulating band as a function of interlayer hybridization t_3. Dashed curve: Occupations on the partner sites in the metallic band to which those $+\delta$ sites are hybridized by t_3. The staggered potential in this case is $\delta = 1.25$. In both panels the linear lattice size and the inverse temperature are $L = 12$ and $\beta = 4$, respectively.

potential δ, so that at $t_3 = 0$ its dispersion relation has two branches, $E_\pm(k) = \pm\sqrt{\epsilon(k)^2 + \delta^2}$. Both bands of Eq. 6.14 are half-filled (the chemical potential $\mu = 0$).

In addition to inducing a band gap 2δ in layer $l = +1$, the staggered potential also creates a CDW phase, with low occupancy $+\delta$ and high occupancy $-\delta$ sites. Here, the CDW order is trivial, in the sense of being induced by an external field, as opposed to arising spontaneously in a symmetric Hamiltonian like the Holstein model. Nevertheless we can still examine how this 'artificial' CDW in layer $l = +1$ affects the site occupations in the metallic band $l = -1$.

Figure 6.8(a) gives the occupations on the $+\delta$ sites of band $l = +1$ as functions of δ for different t_3. As δ grows, the occupation of the high energy sites in layer $l = +1$, which are directly coupled to the staggered field, get increasingly small (solid curves). In turn, the occupations of the partner

sites on layer $l = -1$ which are *not* coupled to δ are also shifted from $\rho = \frac{1}{2}$. These occupations increase in order to take advantage of the decrease in the Pauli blocking. What is interesting in the context of the simulations of the Holstein bilayers in the main part of this chapter is that, while the layer $l = +1$ occupations steadily return to half-filling with increasing t_3, the evolution of the layer $l = -1$ occupations is instead *non-monotonic*. The deviations of the occupations from half-filling first grow with t_3, but then shrink.

This non-monotonicity is seen more clearly in Fig. 6.8(b) which plots similar occupations as a function of t_3 for a fixed δ. The maximum at intermediate $t_3 \sim 2.28$ is reminiscent of the behavior of Fig. 6.2(c), which similarly shows a maximum in the induced CDW order at intermediate t_3 in the metallic layer of the Holstein interface model. Indeed, the agreement between the values of t_3 at which the induced order is maximal is remarkably *quantitative*. To within error bars, the positions of the maxima are the same, although the fall-off at large t_3 is more gradual in the BI-Metal interface case.

6.8. Discussion and conclusions

We have generalized our existing understanding of the effect of interlayer/interorbital hybridization t_3 on *magnetic* order driven by an on-site *electron-electron repulsion* in the Hubbard model to *charge* order originating in *electron-phonon interactions* in the Holstein model. The two scenarios, although qualitatively related, are quite distinct in detail owing to the lower symmetry of the CDW order parameter relative to the magnetic case. Despite this difference, and its consequences such as the appearance of charge order at finite temperature, the basic feature of the destruction of long range order in the limit of large hybridization is shown still to occur. Indeed, one remarkable conclusion of our work is that t_3 seems to restore the degeneracy of pairing and charge correlations at the QCP.

Our most interesting observation is that the coexistence of CDW order on a layer with non-zero electron-phonon coupling λ with a metallic phase on the $\lambda = 0$ layer, which is trivially true at $t_3 = 0$, likely extends out to finite t_3. This conclusion is based on the inability to scale the charge correlations in the $\lambda = 0$ layer unless $t_3 \gtrsim 1.4$ (for $\lambda_{+1} = 0.2$).

The possibility that charge order takes place selectively parallels the known occurrence of distinct Mott transitions in multi-orbital Hubbard models in the coexistence of metallic and insulating behavior. The connection is, however, not exact, since in principle a Mott transition might occur in the absence of spontaneous symmetry breaking, whereas the insulating CDW phase here breaks Z_2 symmetry. With that said, the Mott transition in its most common incarnation, the square lattice Hubbard model, *is* always accompanied by long range antiferromagnetic order. Thus our work does provide a close analog of the case of orbital selective transitions in bands with differing electron-electron interaction strengths.

CHAPTER 7

Photo-Induced Superconductivity in Plaquette Hubbard Model

7.1. Introduction

Out-of-equilibrium dynamics and photoinduced properties have been attracting intense attention recently. In a single-particle setting, periodic drives provide an additional "Floquet dimension", and can result in phenomena such as engineered Chern insulating behavior and Wannier-Stark localization [195]. These techniques have also allowed considerable new insight into strongly correlated systems, and many-body phases induced by either electron-electron or electron-phonon interactions [196, 197, 198, 199], including studies of photoinduced η-pairing [37, 200], bond-order wave (BOW) physics [34], dynamical topological engineering [201, 202], and especially superconductivity [35, 38, 203, 204, 205, 206, 207, 208, 209], both theoretically and experimentally. A focus has been on gaining new insight into cuprate systems, and the origin of pairing in high-T_c materials [210, 211, 212, 213].

One mechanism for the enhancement of superconductivity is the use of photoexcitation to transfer charge between orbitals, thereby shifting the doping away from 1/8 filling where the "stripe anomaly" leads to a suppressed T_c. Here exact diagonalization studies have clarified whether the emergence of superconductivity via photoexcitation seen experimentally results from phonon or electronic mechanisms [207]. Indeed, superconductivity can also be developed out of the 1/8 filling phase through photoexcitation of the Cu-O stretch mode in the plane of the stripes [38]. This coupling to vibrational modes offers advantages in that the lower energy photons have less likelihood of creating high temperature electronic distributions and heating the lattice.

In calculations similar to the study to be described here, a theoretical understanding of the enhancement of pairing is provided through the lifting of the degeneracy between superconducting and charge density wave (CDW) ground states in the attractive Hubbard Hamiltonian [205]. In

the Hubbard-Holstein model, inducing d-wave pairing has been shown to be especially effective at the quantum boundary between the CDW and spin density wave (SDW) ground state phases [207]. Theoretical work within a BCS model has also explored the role of the symmetry of the pair wave function. The existence of nodes in a d-wave phase allows for a more rapid decay, making the dynamics substantially faster than the s-wave channel [203].

In parallel with these developments, theoretical studies have shown that inhomogeneities such as stripe-like or plaquette decorations of two-dimensional square lattices could enhance d-wave pairing in equilibrium [214, 215, 216, 217, 218, 219, 220, 221, 222, 223, 224]. This is an especially rich area of inquiry given the complex entwining of spin and charge textures with pairing [22, 165, 225, 226, 227, 228]. Specifically, under some circumstances inhomogeneities clearly interfere with superconductivity, while in others they appear to play a role in its formation and stability.

In this chapter we *combine* these two themes of out-of-equilibrium dynamics and spatial inhomogeneity. In particular, we examine the effect of pumping on a geometry built up from attractive d-wave binding centers formed by 2×2 plaquettes. Our goal is to understand the interplay of these two effects which are already known *individually* to result in enhanced superconductivity. Our work will therefore examine the possibility that a greater signal of pairing might be thereby engineered, a prospect made particularly intriguing by the recent experimental emulation of fermionic models in 2×2 plaquettes in platforms of quantum dots [229].

7.2. Model and methodology

The two dimensional Hubbard model is described by

$$\hat{\mathcal{H}} = -\sum_{\langle \mathbf{i},\mathbf{j}\rangle,\sigma} \left(t_{\mathbf{i},\mathbf{j}}\, \hat{c}^{\dagger}_{\mathbf{i}\sigma} \hat{c}_{\mathbf{j}\sigma} + \text{H.c.} \right) + U \sum_{\mathbf{i}} \hat{n}_{\mathbf{i},\uparrow} \hat{n}_{\mathbf{i},\downarrow} \,, \tag{7.1}$$

where $\hat{c}_{\mathbf{i}\sigma}(\hat{c}^{\dagger}_{\mathbf{i}\sigma})$ is the annihilation (creation) operator for an electron on site $\mathbf{i}$ with spin $\sigma = \uparrow, \downarrow$ and $\hat{n}_{\mathbf{i},\sigma} = \hat{c}^{\dagger}_{\mathbf{i},\sigma} \hat{c}_{\mathbf{i},\sigma}$ is the number operator. $t_{\mathbf{i},\mathbf{j}} = t_h(t'_h)$ gives the hopping integral within (between) plaquettes, and on-site electron-electron interaction is tuned via U. We set $t_h = 1$ as the energy scale, and the time t is measured in terms of t_h^{-1} with $\hbar = 1$. Throughout this work, we use an $N = 4 \times 4$ lattice with periodic boundary conditions (PBC), as illustrated in Fig. 7.1.

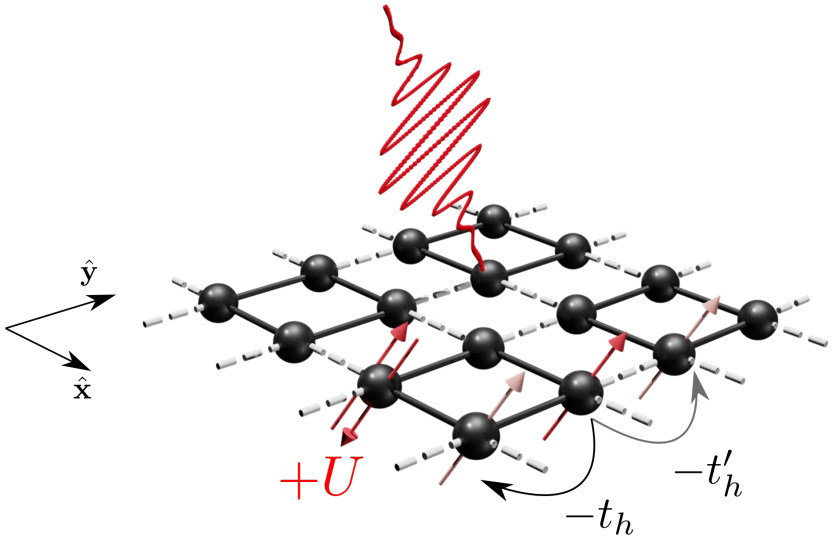

FIGURE 7.1. Schematic illustration of the plaquette Hubbard model on a 4×4 lattice with PBCs, with relevant terms in the Hamiltonian annotated. Dark (light) colored bonds represent the intra-(inter-) plaquette hopping $t_h(t'_h)$.

The system is driven by a time-dependent external field, which is introduced in the Hamiltonian via the Peierls' substitution

$$t_{\mathbf{i},\mathbf{j}}\, \hat{c}^{\dagger}_{\mathbf{i}\sigma} \hat{c}_{\mathbf{j}\sigma} + \text{H.c.} \rightarrow t_{\mathbf{i},\mathbf{j}}\, e^{i\mathbf{A}(t)\cdot(\mathbf{r_i}-\mathbf{r_j})}\, \hat{c}^{\dagger}_{\mathbf{i}\sigma} \hat{c}_{\mathbf{j}\sigma} + \text{H.c.}\ , \tag{7.2}$$

where $\mathbf{A}(t)$ is the spatially uniform vector potential. We choose $\mathbf{A}(t)$, mimicking an ultrafast photoirradiation, of the form

$$\mathbf{A}(t) = A_0 e^{-(t-t_0)^2/2t_d^2} \cos[\omega_0(t-t_0)+\varphi]\, \mathbf{e}_{\text{pol}}\ , \tag{7.3}$$

i.e., an oscillatory Gaussian centered at t_0 and width t_d, with amplitude A_0, frequency ω_0 and polarization direction $\mathbf{e}_{pol} = (\hat{\mathbf{x}} + \hat{\mathbf{y}})/\sqrt{2}$. Finally, φ is a time-phase of the pump pulse, allowing the possibility of phase-averaging that eliminates particular fast coherent oscillations tied to interaction magnitudes [196]. When applicable, results of the dynamics will employ an average over 10 equidistant values of φ in the range $[0, 2\pi)$. In what follows, we set $t_0 = 100\, t_h^{-1}$ and

$t_d = 25\, t_h^{-1}$, with maximum time chosen as $t_{\rm max} = 200\, t_h^{-1}$, which is well after the pump still exhibits a relevant amplitude.

Simulations are carried out with the time-dependent Lanczos method [103, 104], where the time-evolution is obtained via $|\Psi(t+dt)\rangle = e^{-i\hat{\mathcal{H}}(t)dt}|\Psi(t)\rangle$, with dt a sufficiently small time step. The initial state, $|\Psi(t \rightarrow -\infty)\rangle$, is the ground state of (7.1), with $|\Psi(t)\rangle$ and associated measurements being evaluated at each time step.

7.3. Equilibrium results

To map out where an out-of-equilibrium protocol would induce enhanced superconductivity, we start by examining the equilibrium properties of the plaquette Hubbard model across a range of $(t_h'/t_h, U, n_e)$ parameters. Some of these have already been explored at finite temperatures by means of quantum Monte Carlo simulations [221] or at the ground-state [216] in lattice sizes as in Fig. 7.1. Here, we go beyond that and investigate different equal-time correlators computed over the low-lying eigenspectrum of (7.1) [$\hat{\mathcal{H}}|\alpha\rangle = E_\alpha|\alpha\rangle$]. Among them, we calculate the pairing structure factor at different γ-channels

$$P_\gamma = \frac{1}{N}\sum_{\mathbf{i},\mathbf{dr}} \langle \hat{\Delta}_{\mathbf{i}}^{(\gamma)}\ \hat{\Delta}_{\mathbf{i}+\mathbf{dr}}^{(\gamma)\dagger}\rangle\ , \tag{7.4}$$

where $\hat{\Delta}_{\mathbf{i}}^{(\gamma)} = (\hat{c}_{\mathbf{i}+\hat{\mathbf{x}},\sigma} + f(\gamma)\hat{c}_{\mathbf{i}+\hat{\mathbf{y}},\sigma})\hat{c}_{\mathbf{i},\bar{\sigma}}$, with $f(\gamma) = -1(+1)$ for d-wave(extended s-wave, s^*) pairing. In a similar fashion, the *staggered* spin and charge correlations are probed as

$$S_x = \frac{1}{N}\sum_{\mathbf{i},\mathbf{dr}} \langle (-1)^{dx+dy}\hat{O}_{\mathbf{i}}^\dagger \hat{O}_{\mathbf{i}+\mathbf{dr}}\rangle\ , \tag{7.5}$$

where $\hat{O}_{\mathbf{i}} = \hat{n}_{\mathbf{i}\uparrow} \pm \hat{n}_{\mathbf{i}\downarrow}$, and the + sign defines charge (x = CDW) and the − sign spin (x = SDW) density wave order.

Over the large set of parameters available, we focus the investigation on both the doped ($\rho \equiv n_e/N = 0.875$) and undoped cases ($\rho = 1$); the latter described in the section 7.5. Due to geometric constraints in the lattice size we tackle, a period-8 magnetic stripe formation is not supported [21, 22, 230, 231]. The ground state properties of $\hat{\mathcal{H}}$, originally reported in Ref. [216], indicated that a maximum binding energy occurs at intermediate plaquette hopping energies ($t_h'/t_h \simeq 0.5$), and

large repulsive interactions $U \simeq 8\,t_h$. This serves as a paradigm to our investigation, in which we are interested in the set of parameters that maximize the expectation values of pairing correlators over states beyond that of the ground state $|0\rangle$.

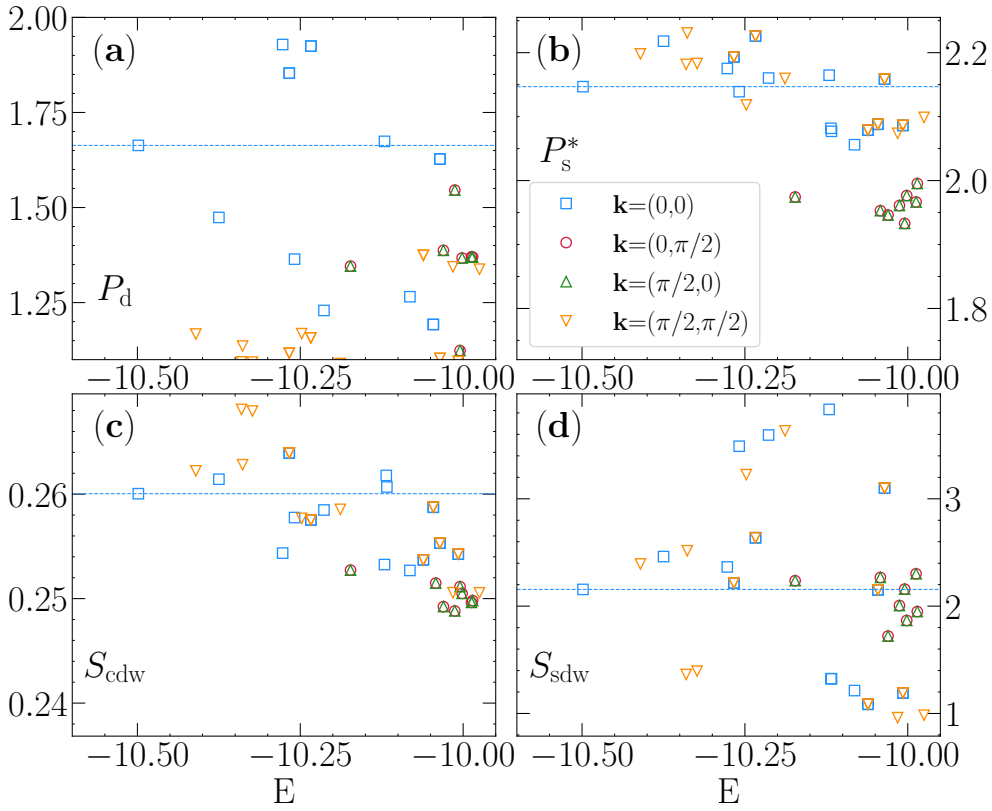

FIGURE 7.2. (a) d-wave, (b) extended s-wave, (c) CDW and (d) SDW structure factor, in the ground state (dashed lines) and the first few excited states. Different colors and symbols represent different quasi-momentum sectors. Parameters used are $t'_h/t_h = 0.8$, $U = 8\,t_h$ and $n_e = 14$. We show the different momentum sectors $\mathbf{k}$ for completeness, since for this filling the ground state always resides at $\mathbf{k} = (0, 0)$. Each sector displays various eigenstates $|\alpha\rangle$, some of which may display degeneracies owing to other point group symmetries not being resolved, e.g. mirror symmetries.

Figure 7.2 displays the eigenstate expectation values (EEV) of the previously introduced correlators for $t'_h/t_h = 0.8$, $U = 8\,t_h$. Most noticeably, a group of three excited states (two of them degenerate) with energy gap $E_\alpha - E_0 \simeq 0.25\,t_h$ (belonging to the same momentum sector) has d-wave pairing $P_d \simeq 1.9$, significantly higher than that of the ground state $P_d = 1.66$. With the exception of the staggered spin correlations, no similar substantial relative increase is seen in other correlators, including the extended s-wave or CDW channels. Equivalent simulations were

performed for other t'_h/t_h values, and a compilation of the results of the relative maximum enhancement over excited states with respect to the ground-state, $\Delta\mathcal{O} \equiv (\max\{\langle\alpha|\hat{\mathcal{O}}|\alpha\rangle\} - \langle 0|\hat{\mathcal{O}}|0\rangle)/\langle 0|\hat{\mathcal{O}}|0\rangle$, is given in Fig. 7.3. Although this maximum increase for the d-wave pairing is seen right in the vicinity of the homogeneous system ($t'_h = t_h$), we focus on $t'_h/t_h = 0.8$ to study the regime of robustly formed plaquettes.

7.4. Out-of-equilibrium results: photoirradiation

Having established that the expectation values of correlators, in particular P_d, measured in excited eigenstates of the Hamiltonian may possess larger values in comparison to the ones at the ground state, we turn to the out-of-equilibrium scenario, with an added time-dependent external field which can cause transitions to these states. Its associated vector potential amplitude is depicted at the top of Fig. 7.4. We follow a procedure that has been proven feasible in other contexts of photoirradiation [**34**, **202**]: by using a fine-tuned temporal perturbation, whose frequency is set resonantly with the target state one is aiming to excite ($\omega_0 \equiv E_{\text{target}} - E_0$), the dynamics at long times thus exhibit a large overlap with such eigenstate.

There are a number of constraints in this protocol. First, the initial and final states need similar quantum numbers. In particular, total momentum, as the vector potential used [Eq. (7.3)] is spatially uniform and does not break translation invariance. Second, the pump needs to be time-constrained, otherwise the system would indefinitely absorb energy from the drive, owing to the thermalizing properties of non-integrable systems [**232**]. In such case, heating towards an infinite temperature regime would ensue at sufficiently long-times, exhibiting featureless correlators.

Following these requirements, we use a pump with parameters $A_0 = 0.1$, $\omega_0 = 0.257\, t_h$ as to closely match that of the excited states with stronger d-wave pairing signal [see top of Fig. 7.2(a)]. These parameters are also reasonably aligned to the ones employed in recent experiments. Using $t_h \simeq 0.3$ eV, which is typically seen in most cuprates materials, $\omega_0 = 0.257\, t_h$ corresponds to 0.08 eV or 20 THz whereas $A_0 = 0.1$ translates into a pump fluence of ~ 0.02 J/cm^2, which are comparable to that used in photo-induced experiments [**38**, **213**]. A discussion of the neighboring frequencies that can influence the dynamics and the reason why we chose this specific ω_0 is given later in this section. One can, however, see from Fig. 7.2 that this ω_0 at least roughly corresponds to the

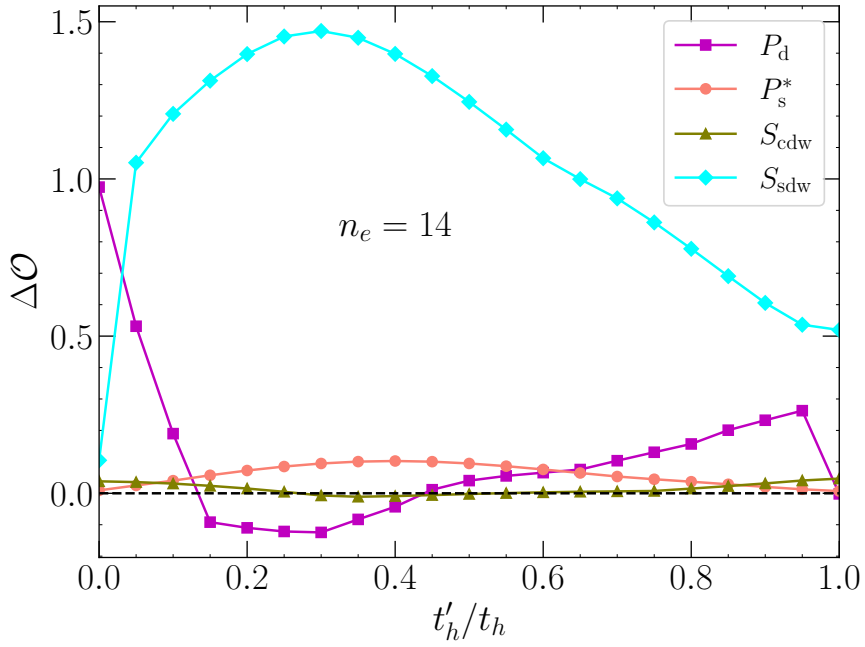

FIGURE 7.3. Relative variation of the maximum eigenstate expectation values $\Delta\mathcal{O}$, quantified over excited states, with respect to its ground-state average (see text) for different correlators, when taking into account at least 24 eigenstates in the low-lying spectrum for the $\mathbf{k} = (0, 0)$ momentum sector. Parameters are the same as in Fig. 7.2: $U = 8\,t_h$ and $n_e = 14$.

excitation energy of a set of states with enhanced P_d. In particular, a doublet of states ($|6\rangle$ and $|7\rangle$), energy-degenerate up to $10^{-12}\ t_h$, possesses one of the largest expectation values of the d-wave pairing P_d ($\simeq 1.92$). Under these conditions, Fig. 7.4(a) shows that a considerable enhancement in d-wave pairing is induced, accompanied by an energy increase, such that the mean energy at long times, $E = \langle\Psi(t = t_{\rm max})|\hat{\mathcal{H}}|\Psi(t = t_{\rm max})\rangle$, is close to the eigenenergy of the target states. Simultaneously, a similar large enhancement on the staggered spin correlations is also achieved [Fig. 7.4(b)].

To demonstrate that the dynamics is being influenced by the target and its neighboring states at these time scales, we compute the overlaps of the time-evolving wave functions and the eigenstates of the equilibrium Hamiltonian, $|\langle\Psi(t)|\alpha\rangle|^2$. We report those in Fig. 7.4(c), where one notices that the weight of the target doublet states rises up to 0.52 and 0.40 after the pump, for states $|7\rangle$ and $|6\rangle$, respectively, explaining thus the enhancement of d-wave pairing under these conditions. The participation of the ground state $|0\rangle$ decreases significantly, whereas the contribution of other

eigenstates is mostly negligible. In the insets, the EEVs of P_d and $S_{\rm sdw}$ are shown in this set of parameters, $(U/t_h, t_h'/t_h) = (8, 0.8)$, together with the mean energy of the system $E(t_{\rm max})$.

A first account of which eigenstates can significantly contribute to the dynamics at a given time is given by the width in energy of $|\Psi(t)\rangle$, defined as $\sigma_E = [\langle\Psi(t)|H^2|\Psi(t)\rangle - \langle\Psi(t)|H|\Psi(t)\rangle^2]^{1/2}$ [**233**, **234**]. This is displayed as a shaded area surrounding $E(t_{\rm max})$ in the insets of Fig. 7.4(a) and 7.4(b), where we notice that the eigenstates within the window are the ones that may display a large overlap with $|\Psi(t)\rangle$ in Fig. 7.4(c). While this window contains six eigenstates in the $\mathbf{k} = (0, 0)$ quasi-momentum sector, not all of them affect the dynamics. Symmetry requirements related to how they couple to the current operator $\hat{\mathcal{J}} = \sum_{\langle \mathbf{i},\mathbf{j}\rangle,\sigma} \left(-it_{\mathbf{i},\mathbf{j}}\, \hat{c}^{\dagger}_{\mathbf{i}\sigma}\hat{c}_{\mathbf{j}\sigma} + \text{H.c.}\right)$ dictate which ones will eventually couple to the external field. That is, besides energy requirements, overlaps $|\langle\alpha|\hat{\mathcal{J}}|0\rangle|^2$ also classify, in first order, the states most influencing the dynamics. Even if the pulse maintains the quasi-momentum of the time-evolving wavefunction, the polarization employed is not sufficient to mix all different mirror symmetry sectors, and as a result some eigenstates must not participate in the dynamical evolution process.

Now that we have confirmed that an enhancement of d-wave pairing is attainable for these pump parameters, we explore other combinations of (A_0, ω_0), identifying the ones that give optimal results in the enhancement of pair correlations at long times. Towards that end, we study the variation of different post-pump observables as $dP_d \equiv P_d(t = t_{\rm max}) - P_d(0)$ [Fig. 7.5(a)] and $dS_{\rm sdw} \equiv S_{\rm sdw}(t = t_{\rm max}) - S_{\rm sdw}(0)$ [Fig. 7.5(b)], quantifying the dynamical variations of d-wave pairing and staggered spin correlations. A relatively narrow band in pump amplitudes A_0 results in increased pairing for resonant drives. The reason can be seen by the map of injected energies $dE \equiv E(t = t_{\rm max}) - E_0$ in Fig. 7.5(c): Increasing A_0 leads to a systematically larger absorbed energy by the system, thereby a larger contribution of states in the bulk of the spectrum, not associated to an enhanced pairing amplitude, is manifest.

We note that not only a specific resonant drive with frequency ω_0, in principle, is able to target a state, but also higher harmonic contributions $2\,\omega_0, 3\,\omega_0, \ldots$. A tuning of other parameters of the pulse, as A_0 and t_d, is necessary in these conditions in order to control the injected energy in the system, while monitoring the typical width in energy of $|\Psi(t_{\rm max})\rangle$. Adjusting these parameters, within physically reasonable limits, thus presents as a systematic protocol to access the physics

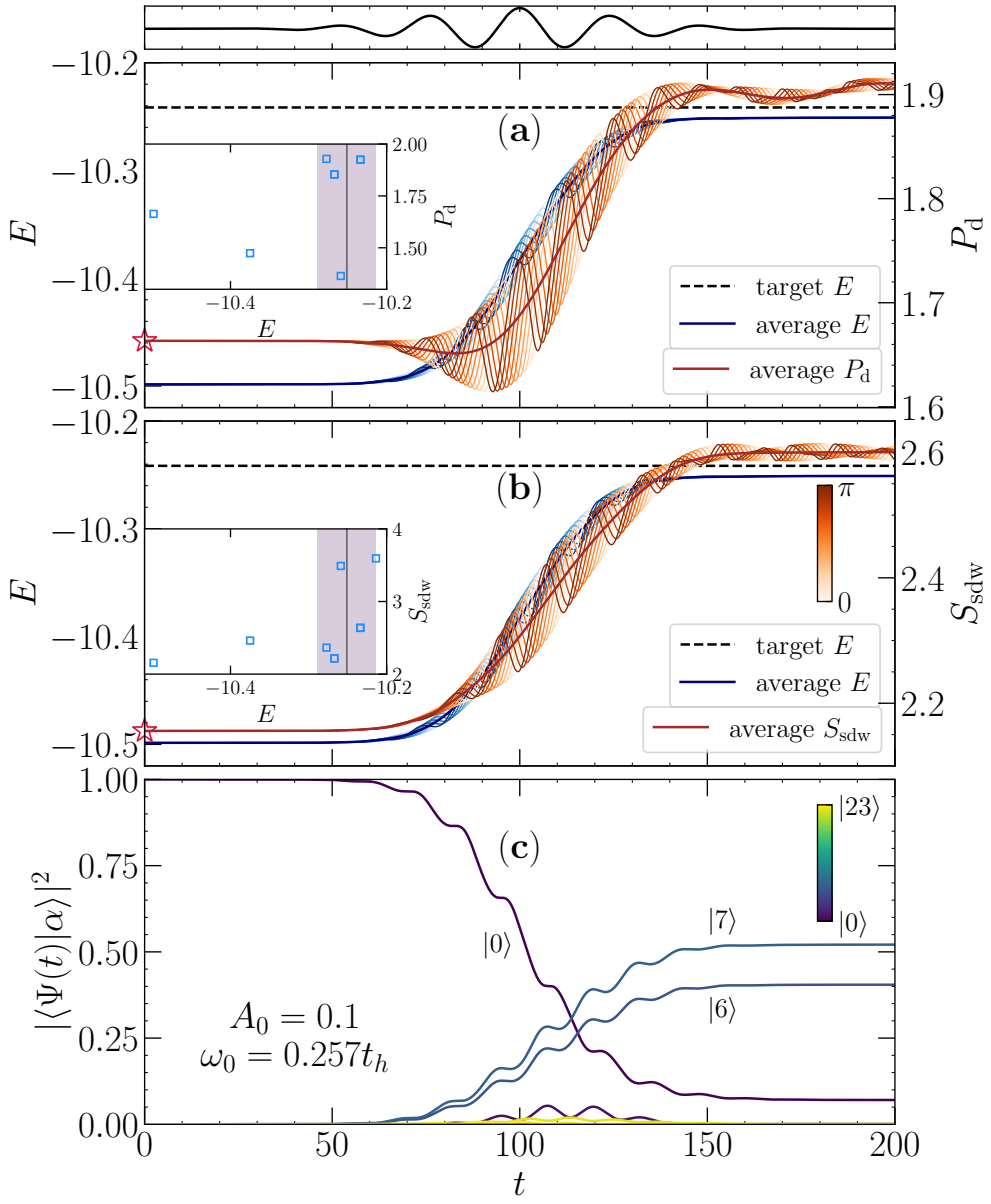

FIGURE 7.4. Top panel: schematics of the pulse amplitude over time. (a) Evolution of the phase-averaged d-wave pair correlation P_d (red solid curve) and mean energy E (blue solid curve). The different curves in shades of red and blue denote the values for each time-phase φ. (b) The same for the staggered spin structure factor. (c) Dynamics of the overlaps $|\langle\Psi(t)|\alpha\rangle|^2$ over the course of photoirradiation. Darker color curves represent lower energy states; the degenerate doublet, $|6\rangle$ and $7\rangle$, displays the largest contribution to $|\Psi(t)\rangle$ as marked, whereas the participation of $|0\rangle$, the initial state, diminishes significantly. The insets give the EEVs for both quantities with the mean energy at $t = t_{\max}$ and within a window given by σ_E (see text). Pump parameters are $A_0 = 0.1$ and $\omega_0 = 0.257\, t_h$.

of competing states close to the ground-state, guaranteeing that the long-time dynamics is largely influenced by the (group of) target excited state(s). Such entwining of different correlations is known to occur in doped Hubbard Hamiltonians and, as we demonstrated, engineered time-dependent perturbations are key to pick one (or more) type in detriment of others.

In the above we have used a specific pump frequency, $\omega_0 = 0.257\, t_h$. Here we discuss the rationale behind this choice, based on the results for the phase averaged enhancement of the P_d pairing correlators at different long times, as displayed in Fig. 7.6. The maximum enhancement of the d-wave pairing at times following the pulse are obtained for frequencies ω_0 slightly below $E_{6,7} - E_0 = 0.2648 t_h$. The reason is that, despite of the target doublet states being mostly excited, contributions from other states to the dynamics, as e.g. state $|1\rangle$, lead to an optimal selection of pump parameters that are slightly below a simple locked-in frequency analysis at $E_{\text{target}} - E_0$.

In other contexts, when initial and target states are related by a first order phase transition in a slightly different regime of parameters of the Hamiltonian, resonant-selection of the states is often highly effective [**34**, **202**], since in such cases they are well separated from the bulk of the spectrum [**235**]. This may explain recent observations of enhancement of d-wave pairing in the vicinity of a phase boundary in systems where the interplay of electron and phonon degrees of freedom is present [**35**, **207**].

7.5. The half-filled case

We have focused on the case of a hole-doped system ($n_e = 14$), guided by the enhanced superconducting properties in cuprate materials in these conditions, and by the large pair binding energy observed in a similar Hamiltonian [**216**]. Yet, the possibility that enhanced pairing can be obtained even when the parent system is a robust insulator has also been proven before [**37**, **207**]. Thus, using our guiding protocol to infer the likelihood that a photoirradiation perturbation, assessing first the properties of the low-lying spectrum, we compute the largest relative enhancement of correlators at half-filling ($n_e = 16$), in analogy to Fig. 7.3.

We notice that other than potentially larger spin fluctuations, the remaining observables we investigate do not possess large matrix elements in the low-lying eigenspectrum in comparison to

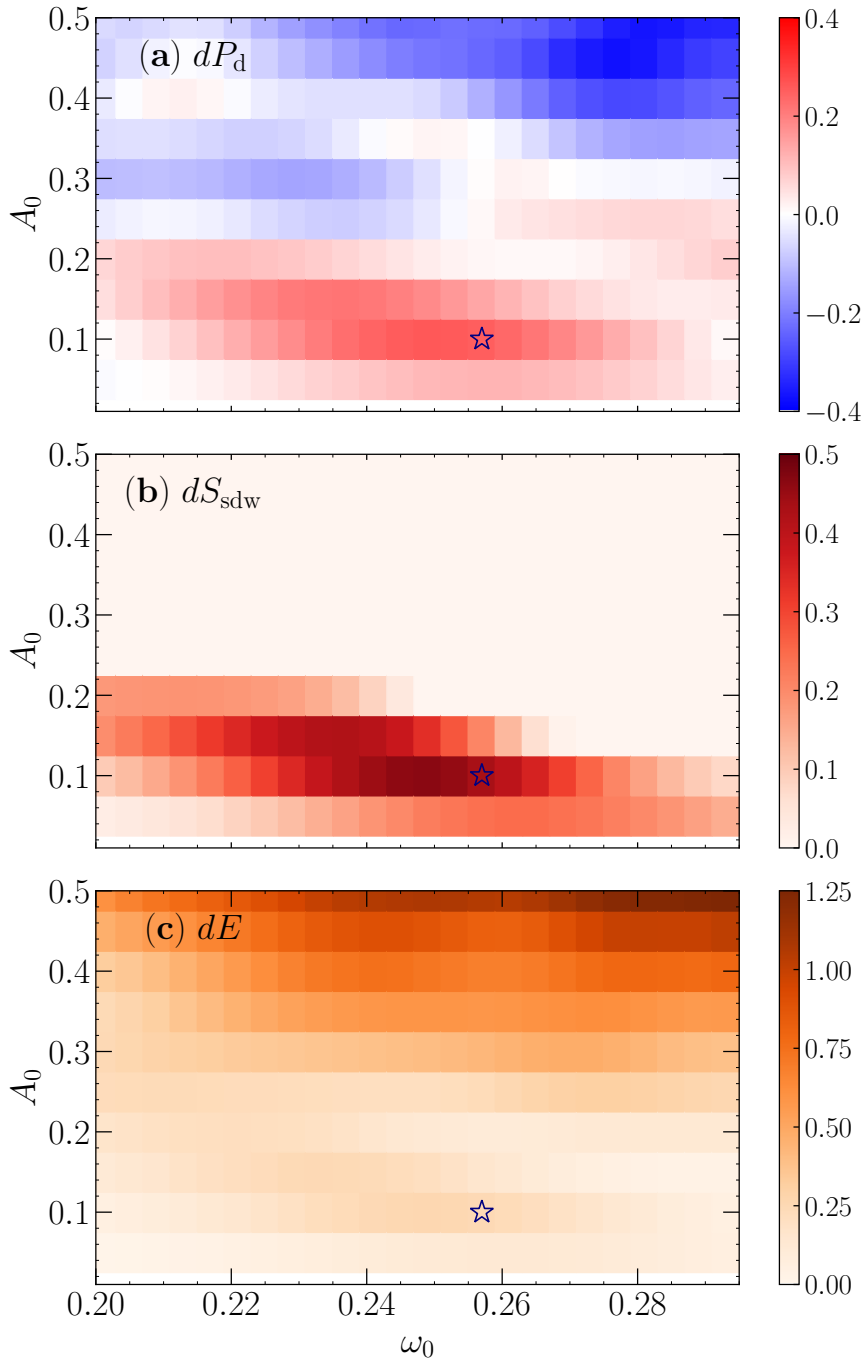

FIGURE 7.5. Contour plot of the enhancement of the d-wave pair [staggered spin] structure factor (a) [(b)] at $t = t_{\mathrm{max}}$ for various pump parameter (A_0, ω_0) values. (c) Similar results for the injected energy by the photoirradiation. All results are obtained for $\varphi = 0$. In all panels, star markers identify the pump parameters used in Fig. 7.4.

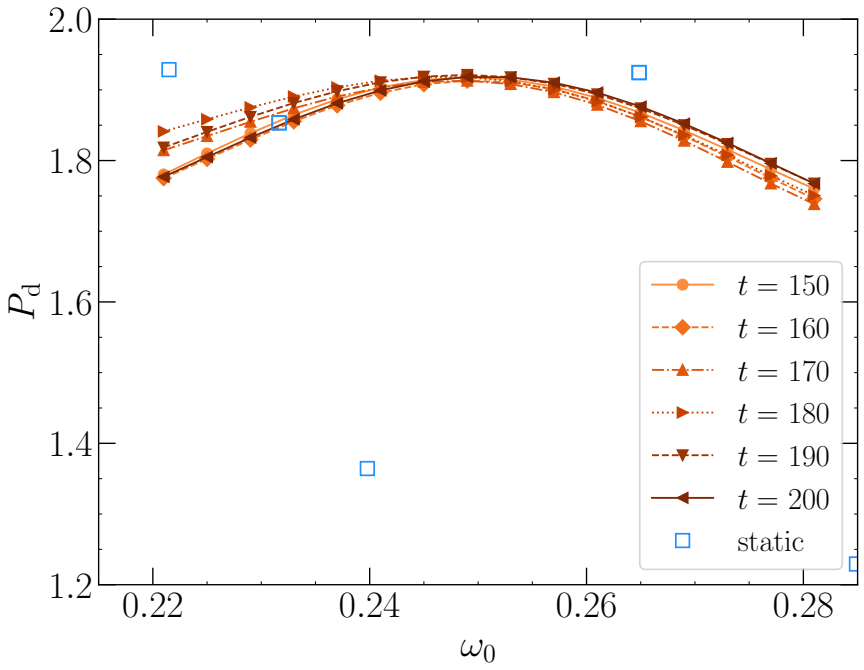

FIGURE 7.6. The phase averaged value of the d-wave pairing correlator at various late times as marked. Empty markers give the expectation values within various low-lying eigenstates.

the ground-state. As a result, no significant dynamical enhancement of pairing is expected in this scenario, including, specifically, d-wave pairing.

7.6. Summary and discussion

We studied the plaquette Hubbard model under photoirradiation, with a goal of dynamical enhancement of d-wave superconductivity. By focusing on a regime away from half-filling ($\rho = 0.875$), we observed a moderate increase of pairing (15% for $t_h'/t_h = 0.8$) at long times in relation to the equilibrium ground state. This is accompanied by enhanced staggered spin fluctuations. Such correlated behavior is not unfamiliar to the physics of unconventional superconductors, where a close competition or entwining of states displaying spin and pairing order is known to occur. That we dynamically reach a simultaneous enhancement of both pair and spin degrees of freedom provides a further, interesting window into the interplay of the low-energy physics of the weakly doped Hubbard model.

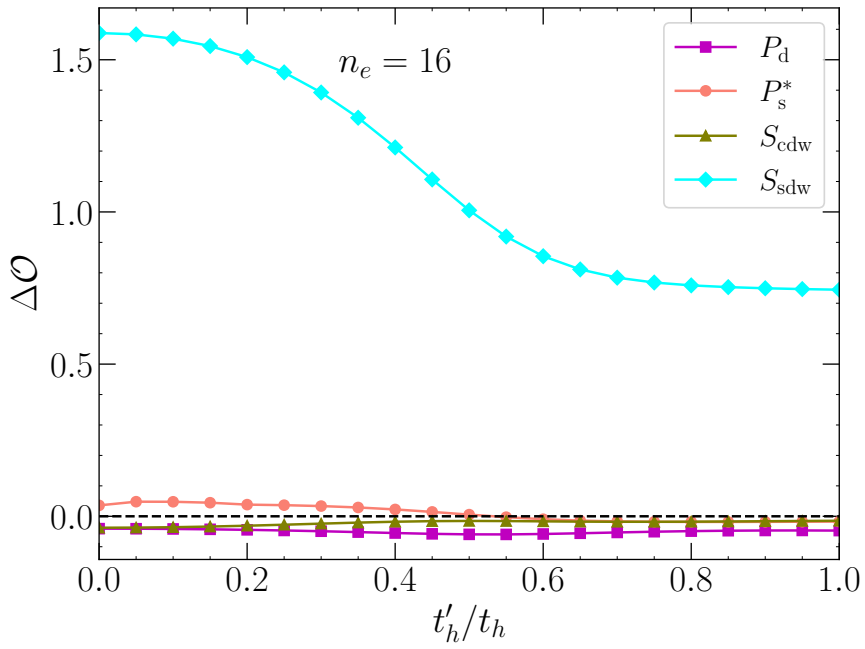

FIGURE 7.7. The equivalent of Fig. 7.3 but for the half-filled system at $U/t_h = 8$. Within a span of 24 eigenstates of the low-lying spectrum at zero quasi-momentum (the same where the ground-state resides) no siginificant increase of matrix elements for pairing correlators in respect to its ground-state average is observed.

A fundamental difference between our study and others that have numerically investigated the increase of superconducting correlations in time is that, in our case, the unperturbed Hamiltonian does not feature strong charge or spin fluctuations associated to long-range order. In particular, the unperturbed system is not a Mott insulator as in Ref. [37] nor a Peierls insulator as in Ref. [207]. Consequently, the gaps separating the ground state and others excited states are substantially smaller. This is one of the reasons behind our pump pulses having an approximate one order of magnitude smaller frequencies.

Our protocol, on the other hand, is intrinsically tied to the specific details of the Hamiltonian's low-lying spectrum, and can be used more generally to induce changes of the wave-function characteristics, surpassing the specific focus on superconductivity [34, 202]. It is worth noticing that a requirement to achieve an efficient targetting of states is that these are well separated in energy from the bulk of the spectrum, otherwise the overlaps with non-desired states is unavoidable. When approaching the thermodynamical limit (not addressed here) the low-lying

eigenspectrum is still discrete (that is, does not form a continuous bulk), and identification of targeting protocol is still feasible.

Nonetheless, a confirmation of these results in larger cluster sizes may shed light on the understanding of its impact in explaining potential connections to experimental results. We stress, however, that in dealing with small clusters, finite-size effects for d-wave correlators do not monotonic decrease with the system size, but are rather influenced by the number z_d of independent neighboring d-wave plaquettes [**236**]. In the thermodynamic limit $z_d = 4$, and the smallest cluster size featuring such configuration possess $N = 20$. This sits at the verge of what is computationally accessible within the scope of exact numerical methods. A potential venue of future investigation is to understand the competition of charge textures (as stripes) and pairing, now adding real-time dynamics to potentially enhance one degree of freedom in detriment of the other. This builds prospects to connect to recent experimental results in cuprates [**210**, **212**, **213**, **237**].

A word of caution, however, is that realistic treatment of such materials using model Hamiltonians might necessarily take into account either phonon degrees of freedom [**35**] or the effects of multiple bands [**36**], such as the distinct Cu and O orbitals. Still, the 'bottom-up' approach we develop to first understand the physics of the low-lying spectrum in order to justify dynamical modifications of suitable correlators should similarly work.

CHAPTER 8

Conclusion and Outlook

The physics of strongly correlated systems is a remarkably rich field with countless questions to explore. In this thesis, we illustrated this by providing several interesting studies with a variety of phase transitions to ordered phases.

In chapter 2 and 3, we have introduced two state-of-art numerical methods: quantum Monte Carlo method and exact diagonalization. The discovery and development of these algorithms, together with the advancement of modern computers themselves, have made these numerical researches possible; on the other hand, the push for further optimised and more efficient algorithms has been and will always be a continuous effort, especially with regards to QMC where the sign problem is still a major roadblock and the search for sign-problem-free Monte Carlo method has been a major research area.

In chapter 4, we have presented DQMC simulations of the Holstein model on a honeycomb lattice. We established the existence of long-range charge order below a finite critical transition temperature $T \sim t/6$ (similar to that of the square lattice), for sufficiently large EPC. The Dirac fermions at non-interacting density of states gives rise to a critical value for $\lambda_D \sim (0.27 \pm 0.01)\, t$, only above which does the long-range order occur; this quantum critical point is also found in the 1D Holstein model [**50**,**132**]. Of course the phonon spectra in real materials are much more complex than the optical phonon mode in the Holstein model, so incorporating realistic phonon dispersion relations in further QMC studies can be an interesting topic, with a focus on the types of electronic order and phase transitions that realistic phonon dispersion induce. A layered honeycomb geometry could be of interest as well, since such investigations open the door to compare layered hexagonal CDW materials like the transition metal dichalcogenides [**134**, **135**, **136**, **137**].

In chapter 5, we have determined the quantitative phase diagram for Dirac fermions interacting with local phonon modes on the π-flux lattice. Similar to that of the honeycomb geometry, we discovered the presence of a quantum critical point $\lambda_{D,\mathrm{crit}}$, below which the system remains a

semi-metal down to $T = 0$. We have compared the values of critical points, both T_c for the temperature-dependent phase transition and $\lambda_{D,\mathrm{crit}}$ for the quantum phase transition, for the two cases, when normalized to the Fermi velocities. We have also studied the dependence on two of the energy scales in the model, electron-phonon coupling λ and phonon frequency ω_0, and considered whether the properties of the model can be described in terms of the effective coupling λ^2/ω_0^2. We find that qualitatively this is indeed the case, but that, quantitatively, the charge structure factor can depend significantly on the individual values of EPC and phonon frequency, especially in the vicinity of the QCP. In investigating this issue we have pushed for substantially smaller values of phonon frequency, $\omega_0 = 0.1$, than what have typically been investigated in QMC treatments of the Holstein Hamiltonian. One more important topic with regard to Dirac fermions interacting with local phonon modes is the universality class of the quantum phase transition and the value of critical exponents, which can be determined through careful QMC studies.

There are many other areas that can be further explored. Away from half-filling, the physics of the Holstein model is much less understood. There have been studies on the 2D square lattice via the QMC method [**59**] which looked at the superconductivity and pairing behavior, but these are much harder than that of the half-filling case, because of the lower transition temperature of SC; the doped Holstein model on other geometries such as the honeycomb lattice, the Lieb lattice or the kagome lattice have not been investigated, and possible pairing and/or charge order on these geometries would be of great interest. The Hubbard-Holstein model is a more realistic model which accounts for both the electron-electron coupling and the electron-phonon coupling, and can greatly push people's understanding of the competition between magnetic order, charge order and pairing order. It's much tougher to carry out such study using QMC, but nonetheless it is still doable when combining different types of Monte Carlo, as well as other numerical methods. The Hubbard-Holstein model with other band structures including Dirac Fermions or flat bands have not been thoroughly studied as well.

In chapter 6, we investigated the effect of interlayer/interorbital hybridization t_3 on charge order originating in electron-phonon interactions in the Holstein model. The main observation suggests the existence of an orbital-selective charge density wave phase, which is the coexistence of CDW order on a layer with non-zero electron-phonon coupling λ with a metallic phase on the $\lambda = 0$

layer. We find this occurs at weak yet finite hybridization $0 < t_3 \lesssim 1.4$ (for $\lambda_{+1} = 0.2$). Another finding is the destruction of long range order in the limit of large hybridization, which is also seen in magnetic order in the case of Hubbard model. This behavior parallels the known occurrence of OSMT, the distinct Mott transitions in multi-orbital Hubbard models in the coexistence of metallic and insulating behavior. An obvious next step is to study the multi-layer hybridization beyond the interface model with two layers; a "2+2" model, i.e. two layers with non-zero electron-phonon interaction coupled with two metallic layers, would allow one to begin to explore the penetration depth of CDW order from the Holstein layers, as well as further investigation of the orbital-selective behavior.

In chapter 7, we studied the dynamic pairing, magnetic order and charge order, including d-wave and s-extended wave superconductivity, on a plaquette Hubbard model under photoirradiation, by employing unbiased time-resolved exact diagonalization. By focusing on a regime away from half-filling ($\rho = 0.875$), we observed an increase of d-wave pairing (15% for $t'_h/t_h = 0.8$) at long times in relation to the equilibrium ground state, accompanied by enhanced staggered spin fluctuations. Real-time dynamics has proven to be an increasingly interesting area of study both experimentally and theoretically, with many questions unanswered yet.

As a final conclusion, the advances of computational methods have enabled us to solve the many-body problem in a much more accurate manner, which have greatly advanced our understanding of strongly correlated systems. Still, many exciting physics phenomena have not been fully understood and much more effort is needed. This thesis provides several contributions to this ongoing quest, aiming to further our understanding on electron-phonon interactions, orbital-selective behaviors, as well as real-time dynamics under photoirradiation. We hope one day, with the collective effort of the wonderful condensed matter community, we will be able to raise a complete and satisfactory answer to the quantum many-body problem.

APPENDIX A

Finite Size Scaling

We have used Finite Size Scaling (FSS) analysis throughout the body of this thesis. Here we provide background and derivation of the FSS analysis approach.

A.1. Critical Behavior

Phase transitions, whether it's condensation of water vapor into liquid water, or between paramagnetic and ferromagnetic phases, can be mathematically expressed as a singular point in a "parameter plane". In the case of phase transition from gas to water, the parameters are pressure and temperature (p, T), whereas for magnetic phase transitions they can be magnetic field and temperature (h, T). The singular behavior in the vicinity of the critical point, can be characterized by a set of *critical exponents* [238], i.e. different quantities can be written as $A \propto t^{-\kappa}$ where t is the approaching parameter and κ is the critical exponent.

We start with the order parameter, which is a function that's different in each phase and hence can be used to identify the phase transition. For example the magnetization m is the order parameter in a magnetic phase transition. Close to the critical point, it behaves as

$$m(T, h = 0) \propto \begin{cases} 0 & \text{for } T > T_c \\ |t|^{\beta} & \text{for } T > T_c \end{cases} \tag{A.1}$$

$$m(T = T_c, h) \propto h^{1/\delta} \tag{A.2}$$

as a function of reduced temperature $t = \frac{T - T_c}{T_c}$ or magnetic field h, and β and δ are two critical exponents. Other quantities include the susceptibility

$$\chi_{\pm}(T, h = 0) \propto |t|^{-\gamma_{\pm}} \tag{A.3}$$

which is characterized by exponent γ, and heat capacity

$$C_{\pm}(T, h = 0) \propto |t|^{-\alpha_{\pm}} \tag{A.4}$$

which is characterized by exponent α. The $\pm$ denotes two side of the critical point. There is also the correlation length, which diverges as

$$\xi_{\pm}(T, h = 0) \propto |t|^{-\nu_{\pm}}\,, \tag{A.5}$$

which is characterized by exponent $\nu_+ = \nu_- = \nu_{\pm}$, and finally correlation functions, which scales as

$$c(r) \propto r^{-d+2-\eta}\,, \tag{A.6}$$

where d is the dimension of the system.

Different physical systems or different phase transitions that share the same set of critical exponents are called in the same *universality class*; for example the CDW phase transition in the Holstein model, studied in this thesis, is in the same universality class as the magnetic phase transition in 2D Ising model, since both break the discrete $\mathcal{Z}_2$ symmetry. The different exponents are not completely independent of each other, there are in fact only two independent ones, and others are related via

$$\begin{aligned} 2\beta + \gamma &= 2 - \alpha = d\nu \\ 2 - \eta &= \frac{\gamma}{\nu} \\ \delta - 1 &= \frac{\gamma}{\beta}\,. \end{aligned} \tag{A.7}$$

Critical exponents for certain universality classes have been calculated or measured over the years. Here we provide the critical exponents for 2D Ising universality class

α	β	γ	δ	ν	η
0	$\frac{1}{8}$	$\frac{7}{4}$	15	1	$\frac{1}{4}$

.

A.2. The Scaling Hypothesis

The scaling hypothesis, originated from Renormalization Group (RG) theory, starts from the basic assumption that the critical behavior would diverge from that of an infinite large system when the correlation length ξ becomes comparable with the finite system scale L [239]. When $L \ll \xi$, L instead of ξ becomes the relevant length scale of the system. For a quantity that diverges (in an infinite large system) as

$$A \propto |t|^{-\kappa}\,, \tag{A.8}$$

we can use Eq. (A.5) $|t| \propto \xi^{-1/\nu}$ to replace $|t|$ with correlation length ξ, so that

$$A \propto \xi^{\kappa/\nu}\,. \tag{A.9}$$

This holds true for $\xi \ll L$, but on a finite size lattice where $\xi \sim L$, the value of A cannot diverge with ξ anymore, so instead we should replace ξ with L

$$A \propto L^{\kappa/\nu}\,, \tag{A.10}$$

for example the reduced temperature

$$|t| \propto L^{-1/\nu}\,. \tag{A.11}$$

Another assumption of the scaling hypothesis is that an observable on a finite lattice, at the vicinity of the critical point, should be a non-singular function of the ratio ξ/L, i.e. A should have the form

$$A \propto L^{\kappa/\nu} f(\xi/L)\,, \tag{A.12}$$

or replacing ξ with t,

$$A \propto L^{\kappa/\nu} g(tL^{1/\nu})\,. \tag{A.13}$$

Equation (A.13) is the principle of finite size scaling analysis. In the CDW phase transition studied, the order parameter, which is the density difference on the two sub-lattices $|n_A - n_B|$,

diverges as

$$|n_A - n_B| \sim L^{-\beta/\nu} g(tL^{1/\nu}) \,, \tag{A.14}$$

and the correlation function

$$c(r) \sim (|n_A - n_B|)^2 \sim L^{-2\beta/\nu} g(tL^{1/\nu}) \,, \tag{A.15}$$

so the structure factor S_{CDW}

$$S_{\mathrm{CDW}} \sim \sum c(r) \sim L^{2-2\beta/\nu} g(tL^{1/\nu}) = L^{\gamma/\nu} g(L^{1/\nu} \frac{T - T_c}{T_c}) \,. \tag{A.16}$$

When plotting $S_{\mathrm{CDW}}/L^{\gamma/\nu}$ as a function of temperature T for different lattice sizes, only at the critical point $T = T_c$ would the function g get independent of L, meaning the curves for different lattice sizes will cross at the critical point; when plotting against $(\beta - \beta_c)L^{1/\nu}$, it will be independent of L throughout the vicinity of critical point, so different lattice sizes will collapse onto one curve, which is usually referred to as data collapse. Finite size scaling is therefore an useful tool when studying phase transitions, especially at locating the critical point.

APPENDIX B

Extracting the Critical Exponents

In chapters 4, 5 and 6, we used the known 2D Ising exponents to do the finite size scaling analysis. It is actually possible to extract critical exponents from QMC simulations, so here we demonstrate this and verify the exponents independently.

As a first example, we take the raw data for the CDW structure factor from chapter 4 Fig. 4.2, along with our estimate $\beta_c = 5.8$, and compute the scatter $\mathcal{S}$ of the scaled data $S_{\mathrm{cdw}}/L^{\gamma/\nu}$ for different lattice sizes $L = 4, 5, 6, 7, 8$. $\mathcal{S}$ is computed by taking data for all pairs L_1, L_2 and measuring the root mean square difference of their scaled structure factors. Fig. B.1 shows the result. The minimum scatter is obtained at $\gamma/\nu \sim 1.85$. We also investigate the critical exponents by performing data collapse using the Simplex algorithm, as described in Ref. [**240**] and references therein. For the same DQMC data, this method provides $\gamma/\nu = 1.89(5)$ and $\nu = 1.0(1)$, for $-10 < (\beta - \beta_c)L^{\nu} < 10$, in line with the previous scatter analysis. The Simplex method also obtains the two exponents separately, as opposed to just their ratio. Within a shorter range, *e.g.* $-6 < (\beta - \beta_c)L^{\nu} < 4$, one finds $\gamma/\nu = 1.8(1)$ and $\nu = 1.0(1)$. This is in reasonable agreement with the 2D Ising values, considering the finite lattice sizes employed.

For a more thorough analysis, we will use the data in chapter 6 for both cases (Holstein bilayer and Holstein-metal interface) as an example. We start by using the scaled data in a large range of critical exponents; subsequently, for each pair of (ν, γ), we proceed with a high-order polynomial fitting of the scaled data, storing the residual $S(\nu, \gamma)$ of the fitting procedure. The set of exponents that minimizes $S(\nu, \gamma)$ is taken as those that characterize the transition. The rationale is that if the dataset is well collapsed for a given (ν, γ), a high-order polynomial fit (with the number of degrees of freedom much smaller than the number of data points) will turn out to have a fairly small error.

Using this procedure, we show in Fig. B.2 the contour plot $S(\nu, \gamma)$ for the data corresponding to the Holstein bilayer at $t_3 = 2$. See Fig. 6.4(f,h) and Fig. 6.5(c,d). The minimum residual is annotated by the white marker. By observing its variation with slightly different critical inverse

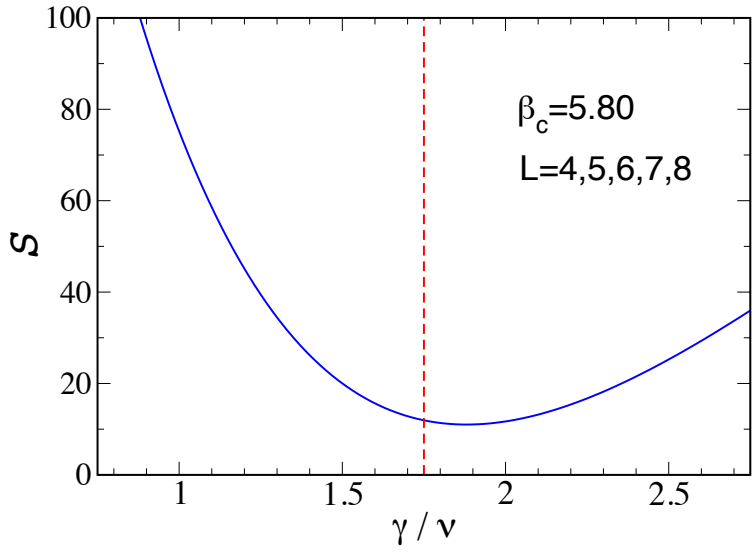

FIGURE B.1. The scatter $\mathcal{S}$ (see text) of DQMC data for $S_{\rm cdw}/L^{\gamma/\nu}$ on different lattice sizes as a function of scaling exponent γ/ν. The vertical dashed line is the 2D Ising value. Data within a range $-10 < (\beta - \beta_c)L < 10$ were used in computing $\mathcal{S}$. The critical value was chosen to be $\beta_c = 5.8$.

temperature β_c, and different polynomial orders used in the fits, we estimate $\nu = 0.95 \pm 0.07$ and $\gamma = 1.7 \pm 0.1$, remarkably close to the 2D Ising exponents $\nu_{\text{2D Ising}} = 1$ and $\gamma_{\text{2D Ising}} = 7/4$.

Figure B.3 shows the contour plot $S(\nu, \gamma)$ for the Holstein-metal interface at $t_3 = 2.0$, where the system is in the global CDW phase. Minimum $S(\nu, \gamma)$ occurred at $\nu = 0.95$ and $\gamma = 1.69$ for the Holstein layer, and $\nu = 1.03$ and $\gamma = 1.76$ for the metallic layer, both within error bars (which we estimate to be $\sim \pm 0.05$) to the 2D Ising exponents. Packages have been developed using this method to determine the critical point and/or critical exponents, for example Ref. [240].

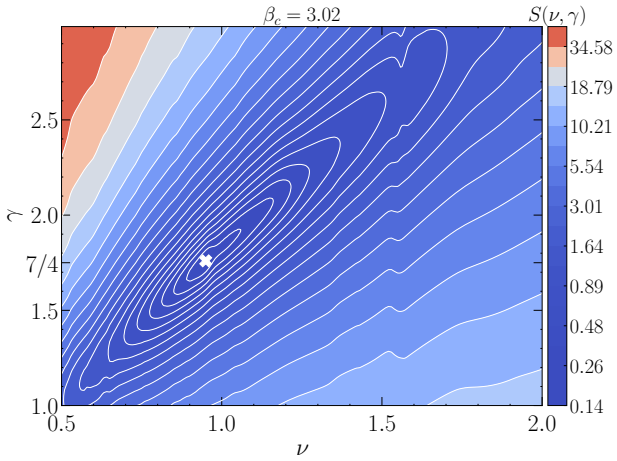

FIGURE B.2. Contour plot of the sum of squared residuals of the least-squares fit $S(\nu, \gamma)$ of the scaled data for the CDW structure factor S^{cdw} of the Holstein bilayer at $t_3 = 2$ (see Fig. 6.3 for the original data). A 16-th order polynomial is used to fit the dataset, and the critical inverse temperature used is $\beta_c = 3.02$. The white marker denotes the minimum $S(\nu, \gamma)$ in the displayed range of ν and γ.

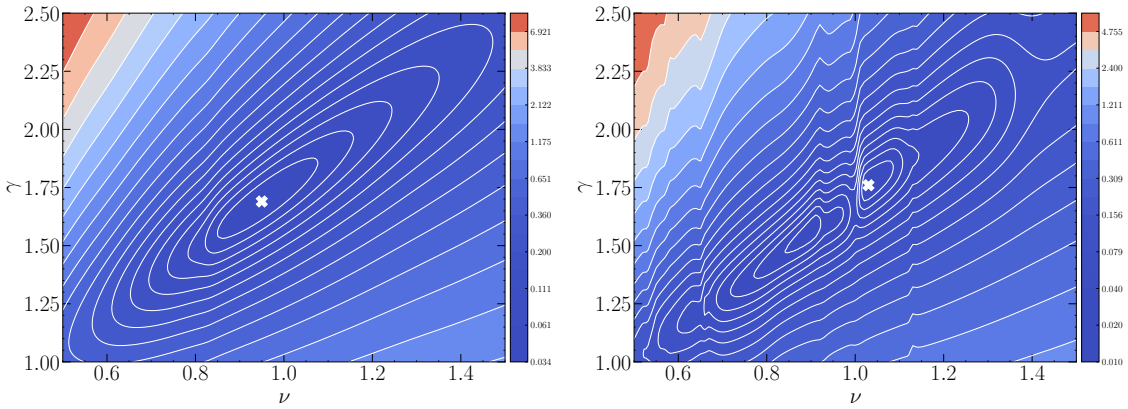

FIGURE B.3. Same analysis as B.2 for the Holstein-metal interface at $t_3 = 2$ for layer 1 (left) and layer -1 (right) (see Fig. 6.4 for the original data). Again a 16-th order polynomial is used. The critical inverse temperature is estimated at $\beta_c = 5.85$. The white marker denotes the minimum $S(\nu, \gamma)$ in the displayed range of ν and γ.

APPENDIX C

Analytic Continuation

Analytic continuation is a technique used to extrapolate data obtained on the imaginary time axis from QMC simulations to the real axis, such as response or spectral functions [241]. This continuation is very ill-conditioned, meaning small fluctuations in the input data can cause large fluctuations in the output data. For this reason, many methods have been proposed and developed [242, 243, 244]; here we will focus on the standard one, the so-called "maximum entropy method" (MaxEnt) [241].

The heart of analytic continuation is the relation between Green's functions on the imaginary-time axis and real frequency Green's functions, or the spectral function

$$G(\tau) = \int_{-\infty}^{\infty} d\omega A(\omega) K(\omega)\,, \tag{C.1}$$

where $K(\omega)$ is called the kernel of the analytic continuation. In the case of Fermionic Green's functions, the kernel is

$$K(\tau, \omega) = -\frac{e^{-\omega\tau}}{1 + e^{-\omega\beta}}\,. \tag{C.2}$$

It should be noticed that analytic continuation can be used on other kernels as well, such as Bosonic kernels. The "forward" question of calculating $G(\tau)$ from $A(\omega)$ would be easy; but the "backward" question of getting $A(\omega)$ from $G(\tau)$ is very hard. One can define a measure of "how good the fit is" via

$$\chi^2 = \sum_{i,j}^{M} [\bar{G}(\tau_i) - G(\tau_i)]^* C_{ij}^{-1} [\bar{G}(\tau_j) - G(\tau_j)]\,, \tag{C.3}$$

where M is the number of estimates for each Green's function component available in the output data, $\bar{G}(\tau_i)$ is the average over estimates

$$\bar{G}(\tau_i) = \frac{1}{M}\sum_{n=1}^{M} G^{(n)}(\tau_i)\,, \tag{C.4}$$

and C_{ij} is the covariance matrix

$$C_{ij} = \frac{1}{M(M-1)}\sum_{n=1}^{M}[G(\tau_i) - G^{(n)}(\tau_i)][G(\tau_j) - G^{(n)}(\tau_j)]\,. \tag{C.5}$$

In the maximum entropy method, an "entropy" term is defined as [245]

$$S[A] = \int d\omega \left[A(\omega) - D(\omega) - A(\omega)\ln\frac{A(\omega)}{D(\omega)}\right]\,, \tag{C.6}$$

where $D(\omega)$ is called the "default model", and the task becomes to minimize

$$Q = \frac{1}{2}\chi^2 - \alpha S[A]\,. \tag{C.7}$$

It is critical to determine the Lagrange multiplier α. Many algorithms have been utilized to find the best α that gives the most accurate spectral functions, including the classical method that uses Bayesian inference [241], Bryan's method [246], the "chi2kink" method [247] and others. Many modern MaxEnt packages have been developed with multiple kernels and multiple methods to choose from, for example the ones presented in Ref. [248] and [249].

Bibliography

[1] Che-Rung Lee, Zhi-Hung Chen, and Quey-Liang Kao. Parallelizing the Hamiltonian computation in DQMC simulations: Checkerboard method for sparse matrix exponentials on multicore and gpu. In *2012 IEEE 26th International Parallel and Distributed Processing Symposium Workshops & PhD Forum*, pages 1889–1897. IEEE, 2012.

[2] G. G. Batrouni and Richard T. Scalettar. Langevin simulations of a long-range electron-phonon model. *Phys. Rev. B*, 99:035114, Jan 2019.

[3] Y.-X. Zhang, W.-T. Chiu, N. C. Costa, G. G. Batrouni, and R. T. Scalettar. Charge order in the Holstein model on a honeycomb lattice. *Phys. Rev. Lett.*, 122:077602, Feb 2019.

[4] Philip W Anderson. More is different: broken symmetry and the nature of the hierarchical structure of science. *Science*, 177(4047):393–396, 1972.

[5] Leon N Cooper. Bound electron pairs in a degenerate Fermi gas. *Phys. Rev.*, 104(4):1189, 1956.

[6] John Bardeen, Leon N Cooper, and John Robert Schrieffer. Theory of superconductivity. *Physical review*, 108(5):1175, 1957.

[7] J George Bednorz and K Alex Müller. Possible high T_c superconductivity in the Ba-La-Cu-O system. *Zeitschrift für Physik B Condensed Matter*, 64(2):189–193, 1986.

[8] Piers Coleman. *Introduction to many-body physics*. Cambridge University Press, 2015.

[9] John Hubbard. Electron correlations in narrow energy bands. *Proceedings of the Royal Society of London. Series A. Mathematical and Physical Sciences*, 276(1365):238–257, 1963.

[10] Mingpu Qin, Thomas Schäfer, Sabine Andergassen, Philippe Corboz, and Emanuel Gull. The Hubbard model: A computational perspective. *Annual Review of Condensed Matter Physics*, 13:275–302, 2022.

[11] EY Loh Jr, JE Gubernatis, RT Scalettar, SR White, DJ Scalapino, and RL Sugar. Sign problem in the numerical simulation of many-electron systems. *Phys. Rev. B*, 41(13):9301, 1990.

[12] J. E. Hirsch. Two-dimensional Hubbard model: Numerical simulation study. *Phys. Rev. B*, 31:4403–4419, Apr 1985.

[13] S. R. White, D. J. Scalapino, R. L. Sugar, E. Y. Loh, J. E. Gubernatis, and R. T. Scalettar. Numerical study of the two-dimensional Hubbard model. *Phys. Rev. B*, 40:506–516, Jul 1989.

[14] Fakher F Assaad and Masatoshi Imada. Insulator-metal transition in the one-and two-dimensional Hubbard models. *Phys. Rev. Lett.*, 76(17):3176, 1996.

[15] CN Varney, C-R Lee, ZJ Bai, S Chiesa, M Jarrell, and RT Scalettar. Quantum Monte Carlo study of the two-dimensional fermion Hubbard model. *Phys. Rev. B*, 80(7):075116, 2009.

[16] Nevill F Mott. The basis of the electron theory of metals, with special reference to the transition metals. *Proceedings of the Physical Society. Section A*, 62(7):416, 1949.

[17] JC Slater. Magnetic effects and the Hartree-Fock equation. *Phys. Rev.*, 82(4):538, 1951.

[18] Aaram J Kim, Fedor Simkovic IV, and Evgeny Kozik. Spin and charge correlations across the metal-to-insulator crossover in the half-filled 2D Hubbard model. *Phys. Rev. Lett.*, 124(11):117602, 2020.

[19] NE Bickers, DJ Scalapino, and SR White. Conserving approximations for strongly correlated electron systems: Bethe-Salpeter equation and dynamics for the two-dimensional Hubbard model. *Phys. Rev. Lett.*, 62(8):961, 1989.

[20] S Raghu, SA Kivelson, and DJ Scalapino. Superconductivity in the repulsive Hubbard model: An asymptotically exact weak-coupling solution. *Phys. Rev. B*, 81(22):224505, 2010.

[21] Bo-Xiao Zheng, Chia-Min Chung, Philippe Corboz, Georg Ehlers, Ming-Pu Qin, Reinhard M. Noack, Hao Shi, Steven R. White, Shiwei Zhang, and Garnet Kin-Lic Chan. Stripe order in the underdoped region of the two-dimensional Hubbard model. *Science*, 358(6367):1155–1160, 2017.

[22] Edwin W Huang, Christian B Mendl, Hong-Chen Jiang, Brian Moritz, and Thomas P Devereaux. Stripe order from the perspective of the Hubbard model. *npj Quantum Materials*, 3(1):1–6, 2018.

[23] Hong-Chen Jiang and Thomas P Devereaux. Superconductivity in the doped Hubbard model and its interplay with next-nearest hopping t'. *Science*, 365(6460):1424–1428, 2019.

[24] RT Scalettar, EY Loh, JE Gubernatis, A Moreo, SR White, DJ Scalapino, RL Sugar, and E Dagotto. Phase diagram of the two-dimensional negative-U Hubbard model. *Phys. Rev. Lett.*, 62(12):1407, 1989.

[25] A Moreo and DJ Scalapino. Two-dimensional negative-U Hubbard model. *Phys. Rev. Lett.*, 66(7):946, 1991.

[26] Rodrigo A Fontenele, Natanael C Costa, Raimundo R dos Santos, and Thereza Paiva. The 2D attractive Hubbard model and the BCS-BEC crossover. *arXiv preprint arXiv:2201.02156*, 2022.

[27] Sandro Sorella and Erio Tosatti. Semi-metal-insulator transition of the Hubbard model in the honeycomb lattice. *EPL (Europhysics Letters)*, 19(8):699, 1992.

[28] Thereza Paiva, R. T. Scalettar, W. Zheng, R. R. P. Singh, and J. Oitmaa. Ground-state and finite-temperature signatures of quantum phase transitions in the half-filled Hubbard model on a honeycomb lattice. *Phys. Rev. B*, 72:085123, Aug 2005.

[29] Z.Y. Meng, T.C. Lang, S. Wessel, F.F. Assaad, and A. Muramatsu. Quantum spin liquid emerging in two-dimensional correlated Dirac fermions. *Nature*, 464(7290):847–851, 2010.

[30] S. Sorella, Y. Otsuka, and S. Yunoki. Absence of a spin liquid phase in the Hubbard model on the honeycomb lattice. *Scientific Reports*, 2:992, 2012.

[31] Fakher F. Assaad and Igor F. Herbut. Pinning the order: The nature of quantum criticality in the Hubbard model on honeycomb lattice. *Phys. Rev. X*, 3:031010, Aug 2013.

[32] Luca F Tocchio, Arianna Montorsi, and Federico Becca. Magnetic and spin-liquid phases in the frustrated t-t' Hubbard model on the triangular lattice. *Phys. Rev. B*, 102(11):115150, 2020.

[33] Aaron Szasz, Johannes Motruk, Michael P Zaletel, and Joel E Moore. Chiral spin liquid phase of the triangular lattice Hubbard model: a density matrix renormalization group study. *Phys. Rev. X*, 10(2):021042, 2020.

[34] Can Shao, Hantao Lu, Hong-Gang Luo, and Rubem Mondaini. Photoinduced enhancement of bond order in the one-dimensional extended Hubbard model. *Phys. Rev. B*, 100(4):041114, 2019.

[35] Yao Wang, Tao Shi, and Cheng-Chien Chen. Fluctuating nature of light-enhanced d-wave superconductivity: A time-dependent variational non-Gaussian exact diagonalization study. *Phys. Rev. X*, 11:041028, Nov 2021.

[36] Yao Wang, Yuan Chen, Thomas P. Devereaux, Brian Moritz, and Matteo Mitrano. X-ray scattering from light-driven spin fluctuations in a doped Mott insulator. *Communications Physics*, 4(1):212, Sep 2021.

[37] Tatsuya Kaneko, Tomonori Shirakawa, Sandro Sorella, and Seiji Yunoki. Photoinduced η pairing in the Hubbard model. *Phys. Rev. Lett.*, 122(7):077002, 2019.

[38] Andrea Cavalleri. Photo-induced superconductivity. *Contemporary Physics*, 59(1):31–46, 2018.

[39] T Holstein. Studies of polaron motion: Part I. the molecular-crystal model. *Annals of Physics*, 8(3):325 – 342, 1959.

[40] Dominic Marchand. *Polaron physics beyond the Holstein model.* PhD thesis, University of British Columbia, 2011.

[41] F. Marsiglio. Pairing and charge-density-wave correlations in the Holstein model at half-filling. *Phys. Rev. B*, 42:2416, Aug 1990.

[42] M. Vekic, R.M. Noack, and S.R. White. Charge-density waves versus superconductivity in the Holstein model with next-nearest-neighbor hopping. *Phys. Rev. B*, 46:271, 1992.

[43] Parhat Niyaz, J. E. Gubernatis, R. T. Scalettar, and C. Y. Fong. Charge-density-wave-gap formation in the two-dimensional Holstein model at half-filling. *Phys. Rev. B*, 48:16011–16022, Dec 1993.

[44] M. Vekić and S. R. White. Gap formation in the density of states for the Holstein model. *Phys. Rev. B*, 48:7643–7650, Sep 1993.

[45] H. Zheng and S. Y. Zhu. Charge-density-wave and superconducting states in the Holstein model on a square lattice. *Phys. Rev. B*, 55:3803–3815, Feb 1997.

[46] A. Macridin, G. A. Sawatzky, and M. Jarrell. Two dimensional Hubbard-Holstein bipolaron. *Phys. Rev. B*, 69:245111, 2004.

[47] JK Freericks, M Jarrell, and DJ Scalapino. Holstein model in infinite dimensions. *Phys. Rev. B*, 48:6302–6314, Sep 1993.

[48] Stefan Blawid and Andrew J. Millis. Quantum phonons and the charge-density-wave transition temperature: A dynamical mean-field study. *Phys. Rev. B*, 63:115114, Mar 2001.

[49] Manuel Weber and Martin Hohenadler. Two-dimensional Holstein-Hubbard model: Critical temperature, Ising universality, and bipolaron liquid. *Phys. Rev. B*, 98:085405, Aug 2018.

[50] Martin Hohenadler and Holger Fehske. Density waves in strongly correlated quantum chains. *The European Physical Journal B*, 91(9):1–14, 2018.

[51] M. Hohenadler and G.G. Batrouni. Dominant charge density wave correlations in the Holstein model on the half-filled square lattice. *Phys. Rev. B*, 100(16):165114, 2019.

[52] Maykon V Araújo, José P de Lima, Sandro Sorella, and Natanael C Costa. Two-dimensional t- t' Holstein model. *Phys. Rev. B*, 105(16):165103, 2022.

[53] N. C. Costa, T. Blommel, W.-T. Chiu, G. Batrouni, and R. T. Scalettar. Phonon dispersion and the competition between pairing and charge order. *Phys. Rev. Lett.*, 120:187003, May 2018.

[54] B. Cohen-Stead, N. C. Costa, E. Khatami, and R. T. Scalettar. Effect of strain on charge density wave order in the Holstein model. *Phys. Rev. B*, 100:045125, Jul 2019.

[55] Z.-X. Li, M. L. Cohen, and D.-H. Lee. Enhancement of superconductivity by frustrating the charge order. *Phys. Rev. B*, 100(24):245105, 2019.

[56] Chuang Chen, Xiao Yan Xu, Zi Yang Meng, and Martin Hohenadler. Charge-density-wave transitions of Dirac fermions coupled to phonons. *Phys. Rev. Lett.*, 122:077601, Feb 2019.

[57] Chunhan Feng, Huaiming Guo, and Richard T Scalettar. Charge density waves on a half-filled decorated honeycomb lattice. *Phys. Rev. B*, 101(20):205103, 2020.

[58] Y.-X. Zhang, H.-M. Guo, and R. T. Scalettar. Charge density wave order on a π-flux square lattice. *Phys. Rev. B*, 101(20):205139, 2020.

[59] Owen Bradley, George G Batrouni, and Richard T Scalettar. Superconductivity and charge density wave order in the two-dimensional Holstein model. *Phys. Rev. B*, 103(23):235104, 2021.

[60] Natanael C Costa, Kazuhiro Seki, and Sandro Sorella. Magnetism and charge order in the honeycomb lattice. *Phys. Rev. Lett.*, 126(10):107205, 2021.

[61] Nikolai V Prokof'ev and Boris V Svistunov. Polaron problem by diagrammatic quantum Monte Carlo. *Phys. Rev. Lett.*, 81(12):2514, 1998.

[62] P.E. Kornilovitch. Continuous-time quantum Monte Carlo algorithm for the lattice polaron. *Phys. Rev. Lett.*, 81:5382, 1998.

[63] Eric Jeckelmann and Steven R. White. Density-matrix renormalization-group study of the polaron problem in the Holstein model. *Phys. Rev. B*, 57:6376–6385, Mar 1998.

[64] P. E. Kornilovitch. Ground-state dispersion and density of states from path-integral Monte Carlo: Application to the lattice polaron. *Phys. Rev. B*, 60:3237–3243, Aug 1999.

[65] Li-Chung Ku, S. A. Trugman, and J. Bonča. Dimensionality effects on the Holstein polaron. *Phys. Rev. B*, 65:174306, Apr 2002.

[66] P. E. Spencer, J. H. Samson, P. E. Kornilovitch, and A. S. Alexandrov. Effect of electron-phonon interaction range on lattice polaron dynamics: A continuous-time quantum Monte Carlo study. *Phys. Rev. B*, 71:184310, May 2005.

[67] J. Bonča, S. A. Trugman, and I. Batistić. Holstein polaron. *Phys. Rev. B*, 60:1633–1642, Jul 1999.

[68] A. S. Alexandrov. Polaron dynamics and bipolaron condensation in cuprates. *Phys. Rev. B*, 61:12315–12327, May 2000.

[69] Ilya Esterlis, SA Kivelson, and DJ Scalapino. Pseudogap crossover in the electron-phonon system. *Phys. Rev. B*, 99(17):174516, 2019.

[70] WP Su, JR Schrieffer, and Ao J Heeger. Solitons in polyacetylene. *Phys. Rev. Lett.*, 42(25):1698, 1979.

[71] Manuel Weber, Fakher F Assaad, and Martin Hohenadler. Excitation spectra and correlation functions of quantum Su-Schrieffer-Heeger models. *Phys. Rev. B*, 91(24):245147, 2015.

[72] Stefan Beyl, Florian Goth, and Fakher F Assaad. Revisiting the hybrid quantum Monte Carlo method for Hubbard and electron-phonon models. *Phys. Rev. B*, 97(8):085144, 2018.

[73] Manuel Weber, Francesco Parisen Toldin, and Martin Hohenadler. Competing orders and unconventional criticality in the Su-Schrieffer-Heeger model. *Phys. Rev. Research*, 2(2):023013, 2020.

[74] Shaozhi Li and Steven Johnston. Quantum monte carlo study of lattice polarons in the two-dimensional three-orbital Su-Schrieffer-Heeger model. *npj Quantum Materials*, 5(1):1–10, 2020.

[75] Bo Xing, Wei-Ting Chiu, Dario Poletti, Richard T Scalettar, and George Batrouni. Quantum Monte Carlo simulations of the 2D Su-Schrieffer-Heeger model. *Phys. Rev. Lett.*, 126(1):017601, 2021.

[76] Chunhan Feng, Bo Xing, Dario Poletti, Richard Scalettar, and George Batrouni. Phase diagram of the Su-Schrieffer-Heeger-Hubbard model on a square lattice. *arXiv preprint arXiv:2109.09206*, 2021.

[77] Xun Cai, Zi-Xiang Li, and Hong Yao. Antiferromagnetism induced by bond Su-Schrieffer-Heeger electron-phonon coupling: A quantum Monte Carlo study. *Phys. Rev. Lett.*, 127(24):247203, 2021.

[78] A Götz, S Beyl, M Hohenadler, and FF Assaad. Valence-bond solid to antiferromagnet transition in the two-dimensional Su-Schrieffer-Heeger model by Langevin dynamics. *Phys. Rev. B*, 105(8):085151, 2022.

[79] Xun Cai, Zi-Xiang Li, and Hong Yao. Robustness of antiferromagnetism in the Su-Schrieffer-Heeger-Hubbard model. *arXiv preprint arXiv:2112.14744*, 2021.

[80] Werner Krauth. *Statistical mechanics: algorithms and computations*, volume 13. OUP Oxford, 2006.

[81] R. Blankenbecler, D. J. Scalapino, and R. L. Sugar. Monte Carlo calculations of coupled boson-fermion systems. i. *Phys. Rev. D*, 24:2278–2286, Oct 1981.

[82] Anders W Sandvik and Juhani Kurkijärvi. Quantum Monte Carlo simulation method for spin systems. *Phys. Rev. B*, 43(7):5950, 1991.

[83] AW Sandvik. A generalization of Handscomb's quantum Monte Carlo scheme-application to the 1D Hubbard model. *Journal of Physics A: Mathematical and General*, 25(13):3667, 1992.

[84] Nikolai V Prokof'ev, Boris V Svistunov, and Igor S Tupitsyn. Exact quantum Monte Carlo process for the statistics of discrete systems. *Journal of Experimental and Theoretical Physics Letters*, 64(12):911–916, 1996.

[85] Bernard Borodel Beard and U-J Wiese. Simulations of discrete quantum systems in continuous euclidean time. *Phys. Rev. Lett.*, 77(25):5130, 1996.

[86] Malvin H Kalos. Monte Carlo calculations of the ground state of three-and four-body nuclei. *Phys. Rev.*, 128(4):1791, 1962.

[87] MH Kalos. Energy of a simple triton model. *Nuclear Physics A*, 126(3):609–614, 1969.

[88] James B Anderson. A random-walk simulation of the Schrödinger equation: H^+_3. *The Journal of Chemical Physics*, 63(4):1499–1503, 1975.

[89] Sandro Sorella, S Baroni, Roberto Car, and M Parrinello. A novel technique for the simulation of interacting fermion systems. *EPL (Europhysics Letters)*, 8(7):663, 1989.

[90] DJ Scalapino and RL Sugar. Monte Carlo calculations of coupled boson-fermion systems. II. *Phys. Rev. B*, 24(8):4295, 1981.

[91] JE Hirsch, DJ Scalapino, RL Sugar, and Richard Blankenbecler. Efficient Monte Carlo procedure for systems with fermions. *Phys. Rev. Lett.*, 47(22):1628, 1981.

[92] Jorge E Hirsch, Robert L Sugar, Doug J Scalapino, and Richard Blankenbecler. Monte Carlo simulations of one-dimensional fermion systems. *Phys. Rev. B*, 26(9):5033, 1982.

[93] Jorge E Hirsch and R Martin Fye. Monte Carlo method for magnetic impurities in metals. *Phys. Rev. Lett.*, 56(23):2521, 1986.

[94] Chia-Chen Chang, Sergiy Gogolenko, Jeffrey Perez, Zhaojun Bai, and Richard T Scalettar. Recent advances in determinant quantum Monte Carlo. *Philosophical Magazine*, 95(12):1260–1281, 2015.

[95] James Gubernatis, Naoki Kawashima, and Philipp Werner. *Quantum Monte Carlo Methods*. Cambridge University Press, 2016.

[96] GG Batrouni, GR Katz, Andreas S Kronfeld, GP Lepage, B Svetitsky, and KG Wilson. Langevin simulations of lattice field theories. *Phys. Rev. D*, 32(10):2736, 1985.

[97] Richard Theodore Scalettar, DJ Scalapino, and RL Sugar. New algorithm for the numerical simulation of fermions. *Phys. Rev. B*, 34(11):7911, 1986.

[98] Zi-Xiang Li and Hong Yao. Sign-problem-free fermionic quantum Monte Carlo: Developments and applications. *Annual Review of Condensed Matter Physics*, 10:337–356, 2019.

[99] Zi-Xiang Li, Yi-Fan Jiang, and Hong Yao. Fermion-sign-free Majarana-quantum-Monte-Carlo studies of quantum critical phenomena of Dirac fermions in two dimensions. *New J. of Phys.*, 17(8):085003, 2015.

[100] Alexander Weiße and Holger Fehske. Exact diagonalization techniques. In *Computational many-particle physics*, pages 529–544. Springer, 2008.

[101] Erik Koch. Exact diagonalization and Lanczos method. In Eva Pavarini, Erik Koch, and Shiwei Zhang, editors, *Many-Body Methods for Real Materials*, volume 9, chapter 7. Forschungszentrum Jülich GmbH, Institute of Advanced Simulation, 2019.

[102] Cornelius Lanczos. An iteration method for the solution of the eigenvalue problem of linear differential and integral operators. 1950.

[103] S. R. Manmana, A. Muramatsu, and R. M. Noack. Time evolution of one-dimensional quantum many body systems. *AIP Conf. Proc.*, 789(1):269–278, 2005.

[104] P. Prelovšek and J. Bonča. *Ground State and Finite Temperature Lanczos Methods*, pages 1–30. Springer Berlin Heidelberg, Berlin, Heidelberg, 2013.

[105] A.K. Geim and K.S. Novoselov. The rise of graphene. *Nature Materials*, 6(3):183–191, 2007.

[106] A.M. Black-Schaffer and C. Honerkamp. Chiral d-wave superconductivity in doped graphene. *Journal of Physics Condensed Matter*, 26(42):423201, 2014.

[107] B. Wunsch, F. Guinea, and F. Sols. Dirac-point engineering and topological phase transitions in honeycomb optical lattices. *New Journal of Physics*, 10:103027, 2008.

[108] B. K. Clark, D. A. Abanin, and S. L. Sondhi. Nature of the spin liquid state of the Hubbard model on a honeycomb lattice. *Phys. Rev. Lett.*, 107:087204, Aug 2011.

[109] Yuichi Otsuka, Seiji Yunoki, and Sandro Sorella. Universal quantum criticality in the metal-insulator transition of two-dimensional interacting Dirac electrons. *Phys. Rev. X*, 6:011029, Mar 2016.

[110] Annica M. Black-Schaffer and Sebastian Doniach. Resonating valence bonds and mean-field d-wave superconductivity in graphite. *Phys. Rev. B*, 75:134512, Apr 2007.

[111] R. Nandkishore, L.S. Levitov, and A.V. Chubukov. Chiral superconductivity from repulsive interactions in doped graphene. *Nature Physics*, 8(2):158–163, 2012.

[112] Carsten Honerkamp. Density waves and cooper pairing on the honeycomb lattice. *Phys. Rev. Lett.*, 100:146404, Apr 2008.

[113] Wan-Sheng Wang, Yuan-Yuan Xiang, Qiang-Hua Wang, Fa Wang, Fan Yang, and Dung-Hai Lee. Functional renormalization group and variational Monte Carlo studies of the electronic instabilities in graphene near $\frac{1}{4}$ doping. *Phys. Rev. B*, 85:035414, Jan 2012.

[114] Maximilian L. Kiesel, Christian Platt, Werner Hanke, Dmitry A. Abanin, and Ronny Thomale. Competing many-body instabilities and unconventional superconductivity in graphene. *Phys. Rev. B*, 86:020507, Jul 2012.

[115] Sandeep Pathak, Vijay B. Shenoy, and G. Baskaran. Possible high-temperature superconducting state with a $d + id$ pairing symmetry in doped graphene. *Phys. Rev. B*, 81:085431, Feb 2010.

[116] Tianxing Ma, Zhongbing Huang, Feiming Hu, and Hai-Qing Lin. Pairing in graphene: A quantum Monte Carlo study. *Phys. Rev. B*, 84:121410, Sep 2011.

[117] Zheng-Cheng Gu, Hong-Chen Jiang, D. N. Sheng, Hong Yao, Leon Balents, and Xiao-Gang Wen. Time-reversal symmetry breaking superconducting ground state in the doped Mott insulator on the honeycomb lattice. *Phys. Rev. B*, 88:155112, Oct 2013.

[118] Shenghan Jiang, Andrej Mesaros, and Ying Ran. Chiral spin-density wave, spin-charge-chern liquid, and $d+id$ superconductivity in 1/4-doped correlated electronic systems on the honeycomb lattice. *Phys. Rev. X*, 4:031040, Sep 2014.

[119] Xiao Yan Xu, Stefan Wessel, and Zi Yang Meng. Competing pairing channels in the doped honeycomb lattice Hubbard model. *Phys. Rev. B*, 94:115105, Sep 2016.

[120] T. O. Wehling, E. Şaşıoğlu, C. Friedrich, A. I. Lichtenstein, M. I. Katsnelson, and S. Blügel. Strength of effective Coulomb interactions in graphene and graphite. *Phys. Rev. Lett.*, 106:236805, Jun 2011.

[121] Igor F. Herbut. Interactions and phase transitions on graphene's honeycomb lattice. *Phys. Rev. Lett.*, 97:146401, Oct 2006.

[122] G. Grüner. The dynamics of charge-density waves. *Rev. Mod. Phys.*, 60:1129–1181, Oct 1988.

[123] G. Grüner. *Density Waves in Solids*, volume 89. Addison-Welsley, 1994.

[124] Natanael C. Costa, Wenjian Hu, Z. J. Bai, Richard T. Scalettar, and Rajiv R. P. Singh. Principal component analysis for fermionic critical points. *Phys. Rev. B*, 96:195138, Nov 2017.

[125] M. Creutz and B. Freedman. A statistical approach to quantum mechanics. *Annals of Physics*, 132:427, 1981.

[126] Kurt Binder. Finite size scaling analysis of Ising model block distribution functions. *Zeitschrift für Physik B Condensed Matter*, 43(2):119–140, 1981.

[127] Anders Sandvik, private communication.

[128] R.E. Peierls. *Quantum Theory of Solids*. Oxford University, New York, 1955.

[129] Aldo H. Romero, David W. Brown, and Katja Lindenberg. Effects of dimensionality and anisotropy on the Holstein polaron. *Phys. Rev. B*, 60:14080–14091, Nov 1999.

[130] M. Hohenadler, H. G. Evertz, and W. von der Linden. Quantum Monte Carlo and variational approaches to the Holstein model. *Phys. Rev. B*, 69:024301, 2004.

[131] G.L. Goodvin, M. Berciu, and G.A. Sawatzky. Green's function of the Holstein polaron. *Phys. Rev. B*, 74:245104, 2006.

[132] Eric Jeckelmann, Chunli Zhang, and Steven R. White. Metal-insulator transition in the one-dimensional Holstein model at half filling. *Phys. Rev. B*, 60:7950–7955, Sep 1999.

[133] L.J. Karssemeijer and A. Fasolino. Phonons of graphene and graphitic materials derived from the empirical potential lcbopii. *Surface Science*, 605(17-18):1611–1615, 2011.

[134] Xuetao Zhu, Yanwei Cao, Jiandi Zhang, E. W. Plummer, and Jiandong Guo. Classification of charge density waves based on their nature. *Proceedings of the National Academy of Sciences*, 112(8):2367–2371, 2015.

[135] C. J. Arguello, S. P. Chockalingam, E. P. Rosenthal, L. Zhao, C. Gutiérrez, J. H. Kang, W. C. Chung, R. M. Fernandes, S. Jia, A. J. Millis, R. J. Cava, and A. N. Pasupathy. Visualizing the charge density wave transition in 2H-$NbSe_2$ in real space. *Phys. Rev. B*, 89:235115, Jun 2014.

[136] Jixia Dai, Eduardo Calleja, Jacob Alldredge, Xiangde Zhu, Lijun Li, Wenjian Lu, Yuping Sun, Thomas Wolf, Helmuth Berger, and Kyle McElroy. Microscopic evidence for strong periodic lattice distortion in two-dimensional charge-density wave systems. *Phys. Rev. B*, 89:165140, Apr 2014.

[137] William Sacks, Dmitri Roditchev, and Jean Klein. Voltage-dependent STM image of a charge density wave. *Phys. Rev. B*, 57:13118–13131, May 1998.

[138] A. H. Castro Neto, F. Guinea, N. M. R. Peres, K. S. Novoselov, and A. K. Geim. The electronic properties of graphene. *Rev. Mod. Phys.*, 81:109–162, Jan 2009.

[139] A.K. Geim. Graphene: Status and prospects. *Science*, 324:1530, 2009.

[140] Wonbong Choi, Indranil Lahiri, Raghunandan Seelaboyina, and Yong Soo Kang. Synthesis of graphene and its applications: A review. *Crit. Rev. in Solid State and Mat. Sci.*, 35(1):52–71, 2010.

[141] Konstantin S Novoselov, VI Fal, L Colombo, PR Gellert, MG Schwab, K Kim, et al. A roadmap for graphene. *nature*, 490(7419):192–200, 2012.

[142] A Brooks Harris, Tom C Lubensky, and Eugene J Mele. Flux phases in two-dimensional tight-binding models. *Phys. Rev. B*, 40(4):2631, 1989.

[143] Yongfei Jia, Huaiming Guo, Ziyu Chen, Shun-Qing Shen, and Shiping Feng. Effect of interactions on two-dimensional Dirac fermions. *Phys. Rev. B*, 88(7):075101, 2013.

[144] Y. Otsuka and Y. Hatsugai. Mott transition in the two-dimensional flux phase. *Phys. Rev. B*, 65:073101, Jan 2002.

[145] Yuichi Otsuka, Seiji Yunoki, and Sandro Sorella. Mott transition in the 2D Hubbard model with π-flux. In *Proceedings of the International Conference on Strongly Correlated Electron Systems (SCES2013)*, page 013021, 2014.

[146] Francesco Parisen Toldin, Martin Hohenadler, Fakher F Assaad, and Igor F Herbut. Fermionic quantum criticality in honeycomb and π-flux Hubbard models: Finite-size scaling of renormalization-group-invariant observables from quantum Monte Carlo. *Phys. Rev. B*, 91(16):165108, 2015.

[147] Thomas C. Lang and Andreas M. Läuchli. Quantum Monte Carlo simulation of the Chiral Heisenberg Gross-Neveu-Yukawa phase transition with a single Dirac cone. *Phys. Rev. Lett.*, 123:137602, Sep 2019.

[148] H-M Guo, Lei Wang, and RT Scalettar. Quantum phase transitions of multispecies Dirac fermions. *Phys. Rev. B*, 97(23):235152, 2018.

[149] Huaiming Guo, Ehsan Khatami, Yao Wang, Thomas P Devereaux, Rajiv RP Singh, and Richard T Scalettar. Unconventional pairing symmetry of interacting Dirac fermions on a π-flux lattice. *Phys. Rev. B*, 97(15):155146, 2018.

[150] Lei Wang, Philippe Corboz, and Matthias Troyer. Fermionic quantum critical point of spinless fermions on a honeycomb lattice. *New J. of Phys.*, 16(10):103008, 2014.

[151] Y. Otsuka, S. Yunoki, and S. Sorella. Quantum Monte Carlo study of the half-filled Hubbard model on the honeycomb lattice. *Journal of Physics: Conference Series*, 454(1):012045, 2013.

[152] Zhichao Zhou, Congjun Wu, and Yu Wang. Mott transition in the π-flux SU(4) Hubbard model on a square lattice. *Phys. Rev. B*, 97:195122, May 2018.

[153] Chia-Chen Chang and Richard T. Scalettar. Quantum disordered phase near the Mott transition in the staggered-flux Hubbard model on a square lattice. *Phys. Rev. Lett.*, 109:026404, Jul 2012.

[154] R. T. Scalettar, N. E. Bickers, and D. J. Scalapino. Competition of pairing and Peierls–charge-density-wave correlations in a two-dimensional electron-phonon model. *Phys. Rev. B*, 40:197, Jul 1989.

[155] Ian Affleck and J Brad Marston. Large-n limit of the Heisenberg-Hubbard model: Implications for high-T_c superconductors. *Phys. Rev. B*, 37(7):3774, 1988.

[156] Monika Aidelsburger, Marcos Atala, Sylvain Nascimbene, Stefan Trotzky, Y-A Chen, and Immanuel Bloch. Experimental realization of strong effective magnetic fields in an optical lattice. *Phys. Rev. Lett.*, 107(25):255301, 2011.

[157] Snir Gazit, Mohit Randeria, and Ashvin Vishwanath. Emergent Dirac fermions and broken symmetries in confined and deconfined phases of Z_2 gauge theories. *Nature Physics*, 13(5):484–490, 2017.

[158] Elliott H. Lieb. Flux phase of the half-filled band. *Phys. Rev. Lett.*, 73:2158–2161, Oct 1994.

[159] Gabriel Mazzucchi, Luca Lepori, and Andrea Trombettoni. Semimetal–superfluid quantum phase transitions in 2D and 3D lattices with Dirac points. *J. of Phys,. B: Atomic, Mol. and Opt. Phys.*, 46(13):134014, 2013.

[160] Ya-Jie Wu, Jiang Zhou, and Su-Peng Kou. Strongly fluctuating fermionic superfluid in the attractive π-flux Hubbard model. *Phys. Rev. A*, 89:013619, Jan 2014.

[161] J. Georg Bednorz and K. Alex Müller. Perovskite-type oxides—the new approach to high-T_c superconductivity. *Rev. Mod. Phys.*, 60(3):585, 1988.

[162] MA Kastner, RJ Birgeneau, G Shirane, and Y Endoh. Magnetic, transport, and optical properties of monolayer copper oxides. *Rev. Mod. Phys.*, 70(3):897, 1998.

[163] T. Timusk and B. Statt. The pseudogap in high-temperature superconductors: an experimental survey. *Rep. Prog. Phys.*, 62(1):61, 1999.

[164] P. A. Lee, N. Nagaosa, and X.-G. Wen. Doping a Mott insulator: Physics of high-temperature superconductivity. *Rev. Mod. Phys.*, 78:17, Jan 2006.

[165] Matthias Vojta. Lattice symmetry breaking in cuprate superconductors: stripes, nematics, and superconductivity. *Advances in Physics*, 58(6):699–820, 2009.

[166] J. M. B. Lopes dos Santos, N. M. R. Peres, and A. H. Castro Neto. Graphene bilayer with a twist: Electronic structure. *Phys. Rev. Lett.*, 99:256802, Dec 2007.

[167] R. Bistritzer and A. H. MacDonald. Transport between twisted graphene layers. *Phys. Rev. B*, 81(24):245412, 2010.

[168] G. Trambly de Laissardiére, D. Mayou, and L. Magaud. Localization of Dirac electrons in rotated graphene bilayers. *Nano Lett.*, 10(3):804–808, 2010.

[169] J. Xue, J. Sanchez-Yamagishi, D. Bulmash, P. Jacquod, A. Deshpande, K. Watanabe, T. Taniguchi, P. Jarillo-Herrero, and B. J. LeRoy. Scanning tunnelling microscopy and spectroscopy of ultra-flat graphene on hexagonal boron nitride. *Nat. Mater.*, 10(4):282, 2011.

[170] T. C. Lang, Z. Y. Meng, M. M. Scherer, S. Uebelacker, F. F. Assaad, A. Muramatsu, C. Honerkamp, and S. Wessel. Antiferromagnetism in the Hubbard model on the bernal-stacked honeycomb bilayer. *Phys. Rev. Lett.*, 109:126402, Sep 2012.

[171] E. McCann and M. Koshino. The electronic properties of bilayer graphene. *Rep. Prog. Phys*, 76(5):056503, 2013.

[172] A. W. Sandvik and D. J. Scalapino. Order-disorder transition in a two-layer quantum antiferromagnet. *Phys. Rev. Lett.*, 72:2777, Apr 1994.

[173] R. T. Scalettar, J. W. Cannon, D. J. Scalapino, and R. L. Sugar. Magnetic and pairing correlations in coupled Hubbard planes. *Phys. Rev. B*, 50:13419, Nov 1994.

[174] M. Vekic, J.W. Cannon, D.J. Scalapino, R.T. Scalettar, and R.L. Sugar. Competition between antiferromagnetic order and spin liquid behavior in the two-dimensional periodic Anderson model at half-filling. *Phys. Rev. Lett.*, 74(12):2367, 1995.

[175] L. Wang, K. S. D. Beach, and A. W. Sandvik. High-precision finite-size scaling analysis of the quantum-critical point of $S = 1/2$ Heisenberg antiferromagnetic bilayers. *Phys. Rev. B*, 73:014431, Jan 2006.

[176] Michael Golor, Timo Reckling, Laura Classen, Michael M. Scherer, and Stefan Wessel. Ground-state phase diagram of the half-filled bilayer Hubbard model. *Phys. Rev. B*, 90:195131, Nov 2014.

[177] S. Doniach. The Kondo lattice and weak antiferromagnetism. *Physica B+C*, 91:231, July 1977.

[178] D.W. Hess, P.S. Riseborough, and J.L. Smith. In G.L. Trigg, editor, *Encyclopedia of Applied Physics*, volume 7, page 435. VCH, New York, 1993.

[179] N. Grewe and F. Steglich. In Jr. K.A.Gschneidner and L.L. Eyring, editors, *Handbook Physics and Chemistry of Rare Earths*, volume 14, page 343. Elsevier, Amsterdam, 1991.

[180] A Liebsch. Single Mott transition in the multiorbital Hubbard model. *Phys. Rev. B*, 70(16):165103, 2004.

[181] C. Knecht, N. Blümer, and P.G.J. Van Dongen. Orbital-selective Mott transitions in the anisotropic two-band Hubbard model at finite temperatures. *Phys. Rev. B*, 72(8):081103, 2005.

[182] K. Bouadim, G. G. Batrouni, and R. T. Scalettar. Determinant quantum Monte Carlo study of the orbitally selective Mott transition. *Phys. Rev. Lett.*, 102(22):226402, 2009.

[183] A. Koga, N. Kawakami, T. M. Rice, and M. Sigrist. Orbital-selective Mott transitions in the degenerate Hubbard model. *Phys. Rev. Lett.*, 92:216402, May 2004.

[184] L. De Leo, M. Civelli, and G. Kotliar. $T = 0$ heavy-fermion quantum critical point as an orbital-selective Mott transition. *Phys. Rev. Lett.*, 101(25):256404, 2008.

[185] Luca de' Medici, S. R. Hassan, Massimo Capone, and Xi Dai. Orbital-selective Mott transition out of band degeneracy lifting. *Phys. Rev. Lett.*, 102:126401, Mar 2009.

[186] Z.-Y. Song, H. Lee, and Y.-Z. Zhang. Possible origin of orbital selective Mott transitions in iron-based superconductors and $Ca_{2-x}Sr_xRuO_4$. *New J. Phys.*, 17(3):033034, 2015.

[187] Z.-Y. Song, X.-C. Jiang, H.-Q. Lin, and Y.-Z. Zhang. Distinct nature of orbital-selective Mott phases dominated by low-energy local spin fluctuations. *Phys. Rev. B*, 96(23):235119, 2017.

[188] J Herbrych, J Heverhagen, ND Patel, Gonzalo Alvarez, Maria Daghofer, Adriana Moreo, and E Dagotto. Novel magnetic block states in low-dimensional iron-based superconductors. *Phys. Rev. Lett.*, 123(2):027203, 2019.

[189] Jacek Herbrych, Gonzalo Alvarez, Adriana Moreo, and E Dagotto. Block orbital-selective Mott insulators: a spin excitation analysis. *Phys. Rev. B*, 102(11):115134, 2020.

[190] Bradraj Pandey, Ling-Fang Lin, Rahul Soni, Nitin Kaushal, Jacek Herbrych, Gonzalo Alvarez, and Elbio Dagotto. Prediction of exotic magnetic states in the alkali-metal quasi-one-dimensional iron selenide compound Na_2FeSe_2. *Phys. Rev. B*, 102(3):035149, 2020.

[191] Maksymilian Środa, Elbio Dagotto, and Jacek Herbrych. Quantum magnetism of iron-based ladders: Blocks, spirals, and spin flux. *Phys. Rev. B*, 104(4):045128, 2021.

[192] B. Xiao, N. C. Costa, E. Khatami, G. G. Batrouni, and R. T. Scalettar. Charge density wave and superconductivity in the disordered Holstein model. *Phys. Rev. B*, 103:L060501, Feb 2021.

[193] Studies of attractive Hubbard models, the anti-adiabatic limit of the Holstein model considered here, within the Dynamical Cluster Approximation are in progress. Philip Dee, Steven Johnston and Thomas Maier, private communication, work in progress.

[194] C. Feng and R. T. Scalettar. Interplay of flat electronic bands with Holstein phonons. *Phys. Rev. B*, 102(23):235152, 2020.

[195] Takashi Oka and Sota Kitamura. Floquet engineering of quantum materials. *Annual Review of Condensed Matter Physics*, 10(1):387–408, 2019.

[196] Yao Wang, Martin Claassen, B. Moritz, and T.P. Devereaux. Producing coherent excitations in pumped Mott antiferromagnetic insulators. *Phys. Rev. B*, 96(23):235142, 2017.

[197] Yao Wang, Martin Claassen, Chaitanya Das Pemmaraju, Chunjing Jia, Brian Moritz, and Thomas P. Devereaux. Theoretical understanding of photon spectroscopies in correlated materials in and out of equilibrium. *Nature Reviews Materials*, 3(9):312–323, 2018.

[198] Joseph Tindall, Frank Schlawin, Michele Buzzi, Daniele Nicoletti, JR Coulthard, H Gao, Andrea Cavalleri, MA Sentef, and Dieter Jaksch. Dynamical order and superconductivity in a frustrated many-body system. *Phys. Rev. Lett.*, 125(13):137001, 2020.

[199] John Sous, Benedikt Kloss, Dante M Kennes, David R Reichman, and Andrew J Millis. Phonon-induced disorder in dynamics of optically pumped metals from nonlinear electron-phonon coupling. *Nature communications*, 12(1):1–8, 2021.

[200] Tomonori Shirakawa, Shohei Miyakoshi, and Seiji Yunoki. Photoinduced η pairing in the Kondo lattice model. *Phys. Rev. B*, 101:174307, May 2020.

[201] J.W. McIver, B. Schulte, F.-U. Stein, T. Matsuyama, G. Jotzu, G. Meier, and A. Cavalleri. Light-induced anomalous Hall effect in graphene. *Nature Physics*, 16(1):38–41, 2020.

[202] C. Shao, P. D. Sacramento, and R. Mondaini. Photoinduced anomalous Hall effect in the interacting Haldane model: Targeting topological states with pump pulses. *Phys. Rev. B*, 104:125129, Sep 2021.

[203] Francesco Peronaci, Marco Schiró, and Massimo Capone. Transient dynamics of d-wave superconductors after a sudden excitation. *Phys. Rev. Lett.*, 115(25):257001, 2015.

[204] Yao Wang, Brian Moritz, C.-C. Chen, C.J. Jia, Michel van Veenendaal, and Thomas P. Devereaux. Using nonequilibrium dynamics to probe competing orders in a Mott-Peierls system. *Phys. Rev. Lett.*, 116(8):086401, 2016.

[205] M. A. Sentef, A. Tokuno, A. Georges, and C. Kollath. Theory of laser-controlled competing superconducting and charge orders. *Phys. Rev. Lett.*, 118:087002, Feb 2017.

[206] Giacomo Mazza and Antoine Georges. Nonequilibrium superconductivity in driven alkali-doped fullerides. *Phys. Rev. B*, 96(6):064515, 2017.

[207] Yao Wang, Cheng-Chien Chen, Brian Moritz, and T.P. Devereaux. Light-enhanced spin fluctuations and d-wave superconductivity at a phase boundary. *Phys. Rev. Lett.*, 120(24):246402, 2018.

[208] M Buzzi, D Nicoletti, M Fechner, N Tancogne-Dejean, MA Sentef, A Georges, T Biesner, E Uykur, M Dressel, A Henderson, et al. Photomolecular high-temperature superconductivity. *Phys. Rev. X*, 10(3):031028, 2020.

[209] Ta Tang, Yao Wang, Brian Moritz, and Thomas P. Devereaux. Orbitally selective resonant photodoping to enhance superconductivity. *arXiv preprint arXiv:2106.04742*, 2021.

[210] D. Fausti, R.I. Tobey, N. Dean, S. Kaiser, A. Dienst, Matthias C. Hoffmann, S. Pyon, T. Takayama, H. Takagi, and A. Cavalleri. Light-induced superconductivity in a stripe-ordered cuprate. *Science*, 331(6014):189–191, 2011.

[211] S. Kaiser, C. R. Hunt, D. Nicoletti, W. Hu, I. Gierz, H. Y. Liu, M. Le Tacon, T. Loew, D. Haug, B. Keimer, and A. Cavalleri. Optically induced coherent transport far above T_c in underdoped $YBa_2C_3O_{6+\delta}$. *Phys. Rev. B*, 89:184516, May 2014.

[212] Daniele Nicoletti, Eliza Casandruc, Yannis Laplace, Vikaran Khanna, Cassandra R. Hunt, Stefan Kaiser, S.S. Dhesi, G.D. Gu, J.P. Hill, and Andrea Cavalleri. Optically induced superconductivity in striped $La_{2-x}Ba_xCuO_4$ by polarization-selective excitation in the near infrared. *Phys. Rev. B*, 90(10):100503, 2014.

[213] Kevin A. Cremin, Jingdi Zhang, Christopher C. Homes, Genda D. Gu, Zhiyuan Sun, Michael M. Fogler, Andrew J. Millis, Dimitri N. Basov, and Richard D. Averitt. Photoenhanced metastable c-axis electrodynamics in stripe-ordered cuprate $La_{1.885}Ba_{0.115}CuO_4$. *Proceedings of the National Academy of Sciences*, 116(40):19875–19879, 2019.

[214] Wei-Feng Tsai and Steven A. Kivelson. Superconductivity in inhomogeneous Hubbard models. *Phys. Rev. B*, 73(21):214510, 2006.

[215] Hong Yao, Wei-Feng Tsai, and Steven A. Kivelson. Myriad phases of the checkerboard Hubbard model. *Phys. Rev. B*, 76(16):161104, 2007.

[216] Wei-Feng Tsai, Hong Yao, Andreas Läuchli, and Steven A. Kivelson. Optimal inhomogeneity for superconductivity: Finite-size studies. *Phys. Rev. B*, 77(21):214502, 2008.

[217] D. Doluweera, A. Macridin, T. Maier, M. Jarrell, and Th. Pruschke. Suppression of d-wave superconductivity in the checkerboard Hubbard model. *Phys. Rev. B*, 78(2):020504, 2008.

[218] Hong Yao and Steven A. Kivelson. Fragile Mott insulators. *Phys. Rev. Lett.*, 105(16):166402, 2010.

[219] Shirit Baruch and Dror Orgad. Contractor-renormalization study of Hubbard plaquette clusters. *Phys. Rev. B*, 82(13):134537, 2010.

[220] P. M. Smith and M. P. Kennett. Disorder effects on superconducting tendencies in the checkerboard Hubbard model. *Phys. Rev. B*, 88:214518, Dec 2013.

[221] T. Ying, R. Mondaini, X.D. Sun, T. Paiva, R. Fye, and R. Scalettar. Determinant quantum Monte Carlo study of d-wave pairing in the plaquette Hubbard Hamiltonian. *Phys. Rev. B*, 90(7):075121, 2014.

[222] Gideon Wachtel, Shirit Baruch, and Dror Orgad. Optimal inhomogeneity for pairing in Hubbard systems with next-nearest-neighbor hopping. *Phys. Rev. B*, 96(6):064527, 2017.

[223] Giacomo Mazza, Adriano Amaricci, and Massimo Capone. Interface and bulk superconductivity in superconducting heterostructures with enhanced critical temperatures. *Phys. Rev. B*, 103(9):094514, 2021.

[224] M. Danilov, E. G. C. P. van Loon, S. Brener, S. Iskakov, M. I. Katsnelson, and A. I. Lichtenstein. Local plaquette physics as key ingredient of high-temperature superconductivity in cuprates. *arXiv preprint arXiv:2107.11344*, 2021.

[225] Steven A Kivelson, Ian P Bindloss, Eduardo Fradkin, Vadim Oganesyan, JM Tranquada, Aharon Kapitulnik, and Craig Howald. How to detect fluctuating stripes in the high-temperature superconductors. *Reviews of Modern Physics*, 75(4):1201, 2003.

[226] Erez Berg, Eduardo Fradkin, Steven A Kivelson, and John M Tranquada. Striped superconductors: how spin, charge and superconducting orders intertwine in the cuprates. *New Journal of Physics*, 11(11):115004, 2009.

[227] Daniel F Agterberg, JC Séamus Davis, Stephen D Edkins, Eduardo Fradkin, Dale J Van Harlingen, Steven A Kivelson, Patrick A Lee, Leo Radzihovsky, John M Tranquada, and Yuxuan Wang. The physics of pair-density waves: cuprate superconductors and beyond. *Annual Review of Condensed Matter Physics*, 11:231–270, 2020.

[228] John M Tranquada. Cuprate superconductors as viewed through a striped lens. *Advances in Physics*, 69(4):437–509, 2020.

[229] J. P. Dehollain, U. Mukhopadhyay, V. P. Michal, Y. Wang, B. Wunsch, C. Reichl, W. Wegscheider, M. S. Rudner, E. Demler, and L. M. K. Vandersypen. Nagaoka ferromagnetism observed in a quantum dot plaquette. *Nature*, 579(7800):528–533, Mar 2020.

[230] Edwin W. Huang, Christian B. Mendl, Shenxiu Liu, Steve Johnston, Hong-Chen Jiang, Brian Moritz, and Thomas P. Devereaux. Numerical evidence of fluctuating stripes in the normal state of high-T_c cuprate superconductors. *Science*, 358(6367):1161–1164, 2017.

[231] Boris Ponsioen, Sangwoo S. Chung, and Philippe Corboz. Period 4 stripe in the extended two-dimensional Hubbard model. *Phys. Rev. B*, 100:195141, Nov 2019.

[232] Luca D'Alessio and Marcos Rigol. Long-time behavior of isolated periodically driven interacting lattice systems. *Phys. Rev. X*, 4:041048, Dec 2014.

[233] S. Sorg, L. Vidmar, L. Pollet, and F. Heidrich-Meisner. Relaxation and thermalization in the one-dimensional Bose-Hubbard model: A case study for the interaction quantum quench from the atomic limit. *Phys. Rev. A*, 90:033606, Sep 2014.

[234] A. Bauer, F. Dorfner, and F. Heidrich-Meisner. Temporal decay of Néel order in the one-dimensional Fermi-Hubbard model. *Phys. Rev. A*, 91:053628, May 2015.

[235] Xie Chen, Zheng-Cheng Gu, and Xiao-Gang Wen. Local unitary transformation, long-range quantum entanglement, wave function renormalization, and topological order. *Phys. Rev. B*, 82:155138, Oct 2010.

[236] T. A. Maier, M. Jarrell, T. C. Schulthess, P. R. C. Kent, and J. B. White. Systematic study of d-wave superconductivity in the 2D repulsive Hubbard model. *Phys. Rev. Lett.*, 95:237001, Nov 2005.

[237] M. Först, R. I. Tobey, H. Bromberger, S. B. Wilkins, V. Khanna, A. D. Caviglia, Y.-D. Chuang, W. S. Lee, W. F. Schlotter, J. J. Turner, M. P. Minitti, O. Krupin, Z. J. Xu, J. S. Wen, G. D. Gu, S. S. Dhesi, A. Cavalleri, and J. P. Hill. Melting of charge stripes in vibrationally driven $La_{1.875}Ba_{0.125}CuO_4$: Assessing the respective roles of electronic and lattice order in frustrated superconductors. *Phys. Rev. Lett.*, 112:157002, Apr 2014.

[238] Mehran Kardar. *Statistical physics of fields*. Cambridge University Press, 2007.

[239] Anders W Sandvik. Computational studies of quantum spin systems. In *AIP Conference Proceedings*, volume 1297, pages 135–338. American Institute of Physics, 2010.

[240] O. Melchert. autoscale.py - a program for automatic finite-size scaling analyses: A user's guide. *arXiv:0910.5403*, 2009.

[241] Mark Jarrell and James E Gubernatis. Bayesian inference and the analytic continuation of imaginary-time quantum Monte Carlo data. *Physics Reports*, 269(3):133–195, 1996.

[242] Anders W Sandvik. Stochastic method for analytic continuation of quantum Monte Carlo data. *Phys. Rev. B*, 57(17):10287, 1998.

[243] KSD Beach, RJ Gooding, and F Marsiglio. Reliable padé analytical continuation method based on a high-accuracy symbolic computation algorithm. *Phys. Rev. B*, 61(8):5147, 2000.

[244] Nikolay V Prokof'ev and Boris V Svistunov. Spectral analysis by the method of consistent constraints. *JETP letters*, 97(11):649–653, 2013.

[245] C. E. Shannon. A mathematical theory of communication. *The Bell System Technical Journal*, 27(3):379–423, 1948.

[246] RK Bryan. Maximum entropy analysis of oversampled data problems. *European Biophysics Journal*, 18(3):165–174, 1990.

[247] Dominic Bergeron and A-MS Tremblay. Algorithms for optimized maximum entropy and diagnostic tools for analytic continuation. *Phys. Rev. E*, 94(2):023303, 2016.

[248] Josef Kaufmann and Karsten Held. ana_cont: Python package for analytic continuation. *arXiv preprint arXiv:2105.11211*, 2021.

[249] Ryan Levy, J.P.F. LeBlanc, and Emanuel Gull. Implementation of the maximum entropy method for analytic continuation. *Computer Physics Communications*, 215:149–155, 2017.